

1989

Laser spectroscopy of the mercury-zinc excimer.

Ezzat M. Hegazi
University of Windsor

Follow this and additional works at: <http://scholar.uwindsor.ca/etd>

Recommended Citation

Hegazi, Ezzat M., "Laser spectroscopy of the mercury-zinc excimer." (1989). *Electronic Theses and Dissertations*. Paper 2574.

This online database contains the full-text of PhD dissertations and Masters' theses of University of Windsor students from 1954 forward. These documents are made available for personal study and research purposes only, in accordance with the Canadian Copyright Act and the Creative Commons license—CC BY-NC-ND (Attribution, Non-Commercial, No Derivative Works). Under this license, works must always be attributed to the copyright holder (original author), cannot be used for any commercial purposes, and may not be altered. Any other use would require the permission of the copyright holder. Students may inquire about withdrawing their dissertation and/or thesis from this database. For additional inquiries, please contact the repository administrator via email (scholarship@uwindsor.ca) or by telephone at 519-253-3000ext. 3208.



National Library
of Canada

Bibliothèque nationale
du Canada

Canadian Theses Service

Service des thèses canadiennes

Ottawa, Canada
K1A 0N4

NOTICE

The quality of this microform is heavily dependent upon the quality of the original thesis submitted for microfilming. Every effort has been made to ensure the highest quality of reproduction possible.

If pages are missing, contact the university which granted the degree.

Some pages may have indistinct print especially if the original pages were typed with a poor typewriter ribbon or if the university sent us an inferior photocopy.

Reproduction in full or in part of this microform is governed by the Canadian Copyright Act, R.S.C. 1970, c. C-30, and subsequent amendments

AVIS

La qualité de cette microforme dépend grandement de la qualité de la thèse soumise au microfilmage. Nous avons tout fait pour assurer une qualité supérieure de reproduction.

S'il manque des pages, veuillez communiquer avec l'université qui a conféré le grade.

La qualité d'impression de certaines pages peut laisser à désirer, surtout si les pages originales ont été dactylographiées à l'aide d'un ruban usé ou si l'université nous a fait parvenir une photocopie de qualité inférieure.

La reproduction, même partielle, de cette microforme est soumise à la Loi canadienne sur le droit d'auteur, SRC 1970, c. C-30, et ses amendements subséquents.

LASER SPECTROSCOPY OF THE HgZn EXCIMER

BY

© EZZAT M. HEGAZI

A Dissertation .

Submitted to the Faculty of Graduate Studies through the
Department of Physics in Partial Fulfillment
of the Requirements for the Degree of
Doctor of Philosophy at
The University of Windsor

Windsor, Ontario, Canada

1989



National Library
of Canada

Bibliothèque nationale
du Canada

Canadian Theses Service Service des thèses canadiennes

Ottawa, Canada
K1A 0N4

The author has granted an irrevocable non-exclusive licence allowing the National Library of Canada to reproduce, loan, distribute or sell copies of his/her thesis by any means and in any form or format, making this thesis available to interested persons.

The author retains ownership of the copyright in his/her thesis. Neither the thesis nor substantial extracts from it may be printed or otherwise reproduced without his/her permission.

L'auteur a accordé une licence irrévocable et non exclusive permettant à la Bibliothèque nationale du Canada de reproduire, prêter, distribuer ou vendre des copies de sa thèse de quelque manière et sous quelque forme que ce soit pour mettre des exemplaires de cette thèse à la disposition des personnes intéressées.

L'auteur conserve la propriété du droit d'auteur qui protège sa thèse. Ni la thèse ni des extraits substantiels de celle-ci ne doivent être imprimés ou autrement reproduits sans son autorisation.

ISBN 0-315-50504-4

(c) Ezzat M. Hegazi 1989
All Rights Reserved

ABSTRACT

Extensive and previously unknown fluorescence and excitation spectra of the HgZn excimer have been observed and correlated with a potential energy (PE) diagram drawn and labelled according to Hund's case (c). The spectra were excited in a Hg-Zn mixture contained in a quartz vapour cell by successive pulses from two dye lasers using the pump-and-probe method, and were recorded using techniques of time-resolved fluorescence spectroscopy. The reservoir states, which became populated by the pump pulse, were found to be the A1, A0⁻ and A0⁺ states. The fluorescence band at 4750 Å, which has a 6µs lifetime and was first observed by Eden¹, was recognized as due to bound-continuum decays from the A1 and A0⁺ states to the X0⁺ ground state, and its time-evolution was recorded at various cell temperatures. Subsequent absorption of the probe pulse resulted in the excitation of several higher-lying states which were identified as the C0⁺, E1, F1 and E0⁻ states. Several excitation spectra were recorded and assigned to C0⁺ ← A0⁺, E1 ← A0⁻, E1 ← A0⁺, F1 ← A0⁺, E0⁻ ← A1 and E0⁻ ← A0⁻ transitions. UV fluorescence bands, which were observed

centered at 2500 Å, 2270 Å and 2230 Å, consisted of well-resolved Condon internal diffraction patterns, and were correlated with appropriate upper-state vibrational wave functions. They were attributed to bound-continuum transitions from the $C0^+$, $E1$ and $F1$ states to the $X0^+$ ground state, respectively. Bound-bound fluorescence bands were observed at 4288 Å, 4122 Å, 4236 Å and 4637 Å, and were identified as arising from $F1 \rightarrow A0^+$, $E0^- \rightarrow A1$, $E0^- \rightarrow A0^-$ and $E0^- \rightarrow B0^-$ transitions, respectively. A predissociation effect, which gave rise to Hg 4916 Å emission, was also observed and interpreted.

Analysis of the experimental data yielded vibrational constants, relative energies and relative internuclear separations of the PE minima for the various states. There is good agreement between the measured transition energies and the values estimated from the PE diagram.

Dedicated to my wife, Jameley

ACKNOWLEDGEMENTS

I wish to express my sincere thanks and appreciation to Dr. L. Krause, under whose supervision this research was conducted, for his essential assistance, encouragement and attention, and for the limitless effort he spent in seeing this thesis to conclusion. I also wish to thank, in a special way, Dr. J.B. Atkinson for his many helpful suggestions and constructive criticism during this research. Thanks are also given to Dr. W.E. Baylis and Dr. G. Chambaud for their important assistance in the theoretical aspects of this work.

I would like to express my true gratitude to Dr. J. Supronowicz not only for his indispensable help and advice during the development of this research, but also for his friendship which made learning from his expertise an enjoyable experience. Thanks are also due to my colleagues; Dr. W. Kedzierski and Dr. R. Berends for their help and technical advice, and to Mr. A. Buzzeo, Mr. B. Masse and Mr. W. Grewe for their invaluable technical expertise.

Although not directly involved in this research, many persons, whom I never had a chance to thank before, ought to

be acknowledged with gratitude. In particular are Dr. H. Talaat, Dr. P. Meijer and, of course, Dr. L. Resca at the Catholic University of America, Washington, D.C., who all showed me the way and helped me a lot during the initial stages of my graduate studies.

I wish to express deep gratitude and affection to my parents whose continued support and love provided me with the incentive and the opportunity to pursue higher education, and especial gratitude and affection to my wife Jameley who provided me with a loving and caring atmosphere, for her inspirational support, understanding and partnership. Finally, the list would not be complete without expressing my loving thanks to my daughter Nadia, for helping me laugh during difficult times and for making all this worthwhile.

The research described in this dissertation was carried out within the framework of Ontario Laser and Lightwave Research Centre and was supported by the Canadian Department of National Defence, through the unsolicited proposals program, and by a grant from the National Sciences and Engineering Research Council of Canada.

TABLE OF CONTENTS

ABSTRACT.....iv

DEDICATION.....vi

ACKNOWLEDGMENTS.....vii

LIST OF TABLES.....xi

LIST OF FIGURES.....xii

1. INTRODUCTION.....1

2. THEORETICAL.....5

 2.1 Potential Energy Curves.....5

 2.1.1 Hund's Case (a)

 2.1.2 Hund's Case (c)

 2.2 Excitation and Decay of the CO^+ , $E1$, $F1$
 and EO^- States.....9

 2.3 Vibrational Spectra of the HgZn Excimer.....16

 2.3.1 The Term Equation

 2.3.2 The Bound-Continuum Spectra

 2.3.3 The Bound-Bound Spectra

3. EXPERIMENTAL.....25

 3.1 Description of The Apparatus.....25

 3.1.1 General

 3.1.2 The Pump Laser

 3.1.3 The Probe Laser

 3.1.4 The Fluorescence Cell and Oven

 3.1.5 The Detection and Data Acquisition System

 3.2 Experimental Procedure.....38

 3.2.1 General

 3.2.2 Preparation of the HgZn Fluorescence Cell

 3.2.3 Registration of the Fluorescence spectrum
 Excited with a Single Laser

 3.2.4 The Pump-and-Probe Experiments

 3.2.4.1 Monochromator Scans of the Fluorescence

Spectra

3.2.4.2 Probe-Laser Scans of the Excitation Spectra

4. RESULTS AND DISCUSSION.....53

4.1 The 4750 Å Fluorescence Band.....53

4.2 Excitation and Decay of the $C0^+$ State.....58

4.2.1 The Fluorescence Spectrum in the 2380-2650 Å Region

4.2.2 The Excitation Spectrum in the 5200-6650 Å Region

4.3 Excitation and Decay of the E1 and F1 States...73

4.3.1 The Fluorescence Spectrum in the 2230-2320 Å Region

4.3.1.1 The $E1 \rightarrow X0^+$ Fluorescence Spectrum

4.3.1.2 The $F1 \rightarrow X0^+$ Fluorescence Spectrum

4.3.2 The Excitation Spectrum in the 4200-4500 Å Region

4.3.3 The Bound-Bound Fluorescence and Excitation Spectra Arising from $F1 - A0^+$ Transitions

4.3.4 Predissociation of the F1 State

4.4 Excitation and Decay of the $E0^-$ State.....97

4.4.1 The Fluorescence Spectrum in the 4000-4450 Å Region

4.4.2 The Fluorescence Spectrum in the 4600-4780 Å Region

4.4.3 The Excitation Spectrum in the 4180-4310 Å Region

5. SUMMARY AND CONCLUSIONS.....113

6. APPENDIX.....117

REFERENCES.....127

VITA AUCTORIS.....130

LIST OF TABLES

3.1 Laser dyes used in the experiments.....30

4.1 Vibrational components of the F1 \rightarrow A0⁺
fluorescence band.....87

4.2 Vibrational components of the E0⁻ \rightarrow A1
fluorescence band.....103

4.3 Vibrational components of the E0⁻ \rightarrow A0⁻
fluorescence band.....104

4.4 Vibrational components of the E0⁻ \rightarrow B0⁻
fluorescence band.....108

5.1 Molecular constants and energy separations of
the A1, A0⁻, A0⁺, B0⁻, C0⁺, E1, F1 and
E0⁻ states.....116

LIST OF FIGURES

2.1	PE diagram for HgZn, drawn and labelled according to Hund's case (a) coupling.....	6
2.2	PE diagram according to Hund's case (c), showing states with $\Omega = 0^+$	10
2.3	PE diagram according to Hund's case (c), showing states with $\Omega = 0^-$	11
2.4	PE diagram according to Hund's case (c), showing states with $\Omega = 1$	12
2.5	PE diagram according to Hund's case (c), showing states with $\Omega = 2$	13
2.6	The formation of a Condon internal diffraction pattern in a bound-continuum fluorescence spectrum.....	20
3.1	Schematic arrangement of the experiment.....	26
3.2	A block diagram of the vacuum system.....	33
3.3	A cross section of the oven used in the experiment.....	34
3.4	Schematic diagram of the distillation chain.....	41
3.5	Schematic diagram for the arrangement of mirrors and lenses used to achieve an optimum overlap between the pump and the probe beams.....	45
3.6	Schematic diagram of the apparatus used to calibrate the probe laser wavelength drive.....	51
4.1	The profile of the fluorescence band excited with 3075.9 Å laser radiation.....	54
4.2	Time-evolution of the 4750 Å fluorescence band and the atomic Zn fluorescence.....	55

4.3	Time-evolution of the 4750 Å fluorescence band at the side-arm temperatures 570 K and 470 K..	57
4.4	Partial PE diagram showing the X0 ⁺ , A1, A0 ⁻ , A0 ⁺ and C0 ⁺ states.....	59
4.5	LIF bands emitted from the selectively populated v' = 6, 7, 8, and 9 levels of the C0 ⁺ state.....	61
4.6	LIF bands emitted from v' = 0, 1, 2, 3, and 4 levels of the C0 ⁺ state.....	63
4.7	Traces of the fluorescence-monitored C0 ⁺ ← A0 ⁺ excitation band system, showing v' ← v'' assignments in the 5200-6600 Å region.....	65
4.8	Traces of the fluorescence-monitored C0 ⁺ ← A0 ⁺ excitation band system, showing some v' ← v'' assignments in the 5100-5350 Å region and the continuum.....	70
4.9	Partial PE diagram showing the X0 ⁺ , A1, A0 ⁻ , A0 ⁺ , E1 and F1 states.....	75
4.10	LIF bands emitted from v' = 1 and v' = 0 levels of the E1 state excited from the A0 ⁺ , v'' = 0 level.....	76
4.11	LIF bands emitted from v' = 1 and v' = 0 levels of the E1 state excited from the A0 ⁻ , v'' = 0 level.....	78
4.12	LIF bands emitted from v' = 1 and v' = 0 levels of the F1 state excited from the A0 ⁺ , v'' = 0 level.....	79
4.13	A trace of the fluorescence-monitored excitation spectrum at 2250 Å, showing the vibrational structures of the F1 ← A0 ⁺ , E1 ← A0 ⁻ and E1 ← A0 ⁺ band systems.....	81
4.14	A trace of the fluorescence-monitored excitation spectrum at 2250 Å, showing the E1 ← A0 ⁺ band system in the region 4420-4620 Å.....	84

4.15	A trace of the $F1 \rightarrow A0^+$ fluorescence band, showing $v' = 0 \rightarrow v''$ assignments.....	85
4.16	A trace of the $F1 \rightarrow A0^+$ fluorescence band, showing $v' = 1 \rightarrow v''$ assignments.....	88
4.17	The $F1 \leftarrow A0^+$ excitation spectrum, showing $v' \leftarrow v''$ assignments, monitored at 4916 Å.....	90
4.18	Hg 4916 Å fluorescence used to monitor the $F1 \leftarrow A0^+$ excitation spectrum.....	91
4.19	Partial PE diagram showing predissociation and pooling resulting in 4916 Å emission.....	94
4.20	Time-evolution of the 4750 Å fluorescence band excited with pump pulses only and of the Hg 4916 Å atomic fluorescence intensity plotted against pump-probe delay.....	95
4.21	Partial PE diagram showing the $X0^+$, $A1$, $A0^-$, $A0^+$, $B0^-$ and $E0^-$ states.....	98
4.22	A trace of two fluorescence bands arising from $E0^- \rightarrow A1$ and $E0^- \rightarrow A0^-$ transitions, showing $v' = 0 \rightarrow v''$ assignments.....	100
4.23	A trace of two fluorescence bands arising from $E0^- \rightarrow A1$ and $E0^- \rightarrow A0^-$ transitions, showing $v' = 1 \rightarrow v''$ assignments.....	102
4.24	A trace of the fluorescence band excited with 4188 Å probe radiation and originating from the $E0^-$, $v' = 0 \rightarrow B0^-$, v'' transitions, showing $v' \rightarrow v''$ assignments.....	105
4.25	A trace of the fluorescence band excited with 4200 Å probe radiation and originating from the $E0^-$, $v' = 1 \rightarrow B0^-$, v'' transitions, showing $v' \rightarrow v''$ assignments.....	107

4.26	A trace of the $E0^-, v' = 0 \leftarrow A1, v''$ and $E0^-, v' = 0 \leftarrow A0^-, v''$ excitation bands, monitored at 4675 Å.....	110
4.27	A trace of the $E0^-, v' = 1 \leftarrow A1, v''$ and $E0^-, v' = 0 \leftarrow A0^-, v''$ excitation bands, monitored at 4719 Å.....	112
A.1	Computer-simulated intensity distribution in the $F1 \rightarrow A0^+$ fluorescence spectrum.....	118
A.2	Computer-simulated intensity distribution in the $E0^- \rightarrow A1$ fluorescence spectrum.....	119
A.3	Computer-simulated intensity distribution in the $E0^- \rightarrow A0^-$ fluorescence spectrum.....	120
A.4	Computer-simulated intensity distribution in the $E0^- \rightarrow B0^-$ fluorescence spectrum.....	121
A.5	Computer-simulated intensity distribution in the $E1 \leftarrow A0^+$ excitation spectrum.....	123
A.6	Computer-simulated intensity distribution in the $C0^+ \leftarrow A0^+$ excitation spectrum.....	123
A.7	Computer-simulated intensity distribution in the $E0^-, v' = 0 \rightarrow B0^-, v''$ fluorescence spectrum, with $\Delta r_e = .08 \text{ \AA}, .12 \text{ \AA}$ and $.20 \text{ \AA}$	124
A.8	Computer-simulated intensity distribution in the $E0^-, v' = 1 \rightarrow B0^-, v''$ fluorescence spectrum, with $\Delta r_e = .08 \text{ \AA}, .12 \text{ \AA}$ and $.20 \text{ \AA}$	125

1 INTRODUCTION

There have been several recent reports on experimental and theoretical studies of group-2b metal excimers which exhibit emission in the blue-green spectral region and might become vehicles for molecular dissociation lasers with a large energy storage capability. Of particular interest are the spectroscopic investigations of $\text{Hg}_2^{2,3}$ and Hg_3^4 , the calculations of potential energy (PE) curves for Hg_2 and TlHg^5 , and of the energy states of Zn_2^6 and Zn_3^7 . Since Hg forms strong bonds with excited metal atoms because of its high polarizability and since its vapour pressure can reach high values at reasonable temperatures, excimers which include a mercury atom are among the first to be investigated. However, the many efforts to produce lasers based on transitions in the blue-green region in these systems have not met with success. Hill et al.⁸ attempted to measure the gain at all wavelengths which were probed in the 3900 - 5145 Å region of the Hg_2 spectrum, but found no positive result. This explained why Carbone and Litvak⁹ failed to produce laser emission based on transitions from the O_u^+ to the O_g^+ states. The contradiction between the results of Schlie et al.¹⁰, who achieved positive gain on both wings of the Hg_2 3350 Å continuum band using a He-Cd⁺ laser and an Ar⁺ laser, and the results of Komine and Byer¹¹, who observed a net

absorption cross section at 3250 Å and 4420 Å, finally led to the conclusion that gain from the Hg₂ excimer may be suppressed by absorption from excited states.

The kinetics of fluorescence and absorption of the HgCd molecule were investigated by McGeoch^{12,13} who used optical excitation at 2660 Å. Two species of this molecule, HgCd(a) and HgCd(b), were produced and distinguished on the basis of the ratio of cadmium-to-mercury number densities. In HgCd(a), the ratio was ≤ 0.2 , and the excitation at 2660 Å was into the Hg₂(1_u) state followed by radiation mostly of the 2.4 μ s 4700 Å HgCd(a) band. HgCd(b), on the other hand, was produced by making the ratio approximately unity. In this case, the excitation at 2660 Å was into the Cd₂(¹ Σ_u^+) state, and the emission was in the 150 ns HgCd(b) 4600 Å band. The results of the experiments performed on HgCd (b)¹² showed a rapid radiative decay and the simultaneous presence of Cd₂ and Cd₃ reservoirs, which left only a small fraction of the HgCd(b) excimer present. This, in turn, reduced its potential as a high-energy storage candidate. As for HgCd(a)¹³, although it was found that the single-electron collisional rate for its destruction was very low, it did not prove to be the basis for an efficient laser.

The HgTl excimer has been known to emit two intense bands at 4590 Å and 6560 Å and a less intense band at 5230 Å. Drummond and Schlie¹⁴ estimated that, if successful, a gain coefficient of about 1% per centimeter at either 4590 Å

or 6560 Å could be achieved with a particular ratio of the Hg/Tl densities at 720 °C. They also found that, by substituting TlI for the pure metal, the kinetics and spectra of the excimer were not changed, and by using this compound, the operating temperature could be reduced to around 350 °C. However, the authors finally concluded that TlI did not possess strongly bound low-lying electronic states from which transitions to the dissociative ground state were optically allowed.

In the HgZn excimer only one broad emission band was observed at 4750 Å, arising from a transition between an excited metastable state and the dissociative ground state¹, but this observation was not followed up by theoretical or further experimental work. In this dissertation, I report the results of an extensive spectroscopic investigation of HgZn, in which I observed numerous and previously unknown fluorescence and excitation bands and assigned them to transitions between specific molecular states located on a PE diagram which was produced simultaneously but independent of the experimental study^{15,16}. I used the Pump-and-probe method which proved to be very successful in the recent extensive experiments on Hg₂ and Hg₃ excimers carried out in this laboratory^{17-19,4}.

The HgZn molecule has a dissociative ground state and can only be formed in an excited state. Unlike homonuclear diatomic molecules such as Hg₂ and Cd₂, the electronic

states of HgZn do not split into gerade or ungerade states and the $g \leftrightarrow u$ selection rule cannot be used to assist with the identification of electronic states which participated in a particular transition. Nevertheless, the spectroscopic information derived from the excitation and fluorescence spectra led to satisfactory assignments which agreed well with the theoretically predicted transition energies. These data will be useful in arriving at conclusions as to whether gain at particular wavelengths is expected or whether it is likely to be suppressed by absorption.

The PE curves based on Hund's case(a) and on the more realistic Hund's case(c) are shown in Chapter 2. In Chapter 3, I describe in detail the apparatus used in the experiment, the pump-and-probe method and the methods of time-resolved fluorescence spectroscopy. The experimental results are presented and interpreted in Chapter 4 which also includes tables of the numerical data yielded by the experiment. Finally, the summary and conclusions are stated in Chapter 5.

2 THEORETICAL

2.1 Potential Energy Curves

2.1.1 Hund's Case (a)

The PE curves shown in Fig. 2.1 have been produced by Chambaud and Baylis^{15,16} using four-electron pseudopotentials for Hg and Zn. The atomic pseudopotentials and core-overlap terms were yielded by relativistic Hartree-Fock calculations and were combined in SCF-CI computations of electronic eigenstates of the four valence electrons as a function of internuclear separation. At the present stage, effects due to long-range polarization are not yet incorporated in the calculations. To a first approximation²⁰, the $X^1\Sigma$ ground state may be considered as the average of the Hg_2 and Zn_2 ground states, with the same asymptotic energy which is also taken as a reference zero value for the higher PE curves whose asymptotic values were assumed from experimental data. The Zn and Hg parameters were taken from ref. 21, those of Hg_2 were taken from refs. 5, 22 and 23, and those of Zn_2 from refs. 7, 24 and 25. For the sake of simplicity and clarity, the potential curves in Fig. 2.1, are drawn and labeled according to Hund's case(a) coupling, where spin-orbit effects are taken to be small. In view of the large

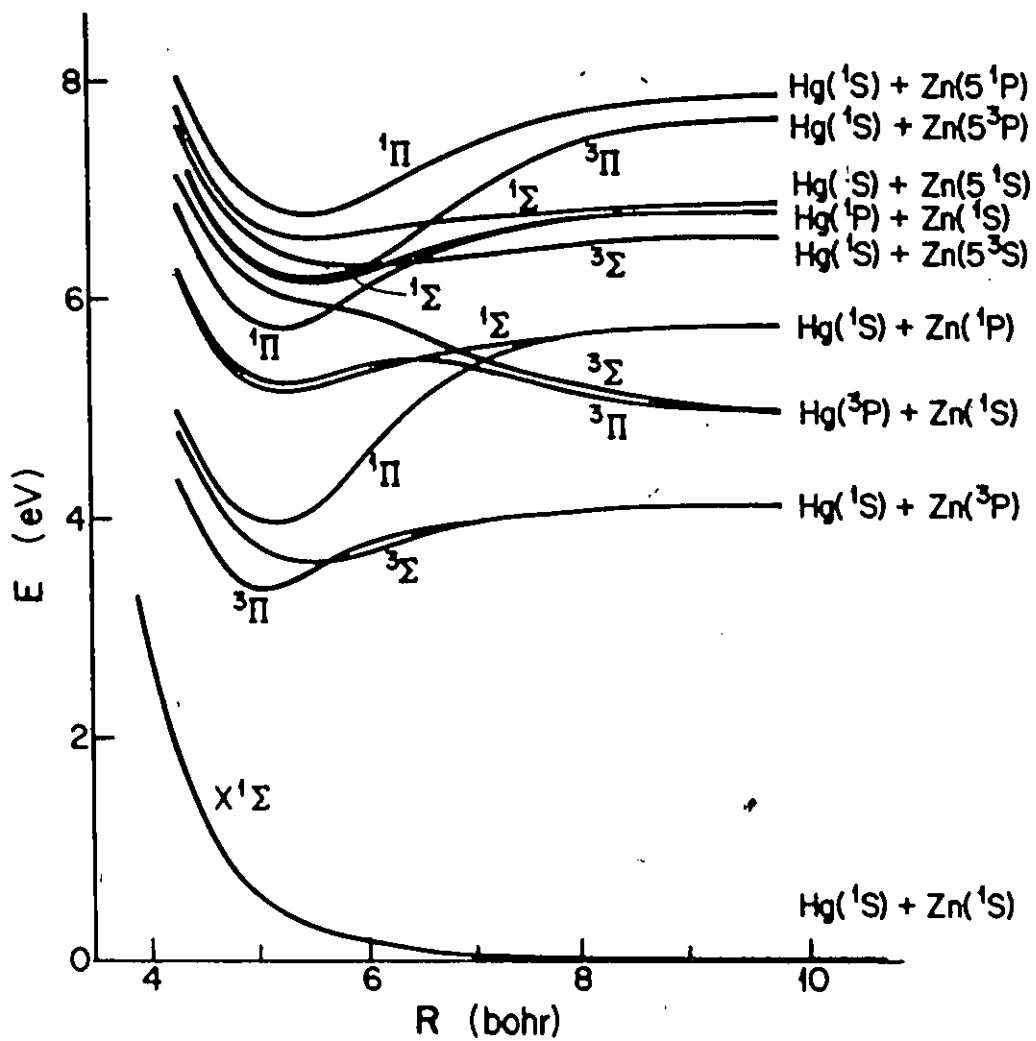


Figure 2.1 PE diagram for HgZn, drawn and labelled according to Hund's case (a) coupling.

fine-structure splitting in atomic mercury, this is a rather poor approximation, and it is more appropriate to use Hund's case(c) coupling, in which the curves are labeled by Ω , the quantum number corresponding to the projection of the electronic angular momentum j on the internuclear axis, and in which curves of the same Ω do not cross. This is done in section 2.2. In Hund's case(a), the low-lying excited states arise from two groups of states that are combined into a PE diagram which also includes the appropriate avoided crossings between the states of the first group and those of the second.

The first group of states is formed from a ground-state Hg or Zn and the other atom in a 3P or 1P excited state, corresponding to the configurations $nsnp$. Considerations of molecular-orbital energy levels indicate that the lowest excited states, correlated with the Zn^3P state, should have a (binding) character similar to the $^3\Sigma_u^+$ and $^3\Pi_g$ states of Zn_2 , except that in HgZn the bond is longer and the PE well depth smaller than in Zn_2 . Similar arguments apply to the $^1\Pi$ and $^1\Sigma$ states correlated with the Zn^1P state, and it is possible to deduce that the states correlated with the Hg($^3P, ^1P$) atomic states are repulsive, though less than the corresponding repulsive states in the case of Hg_2 .

The preliminary results of the calculations also provide information about the nature of the wave functions in the molecular region. Accordingly, the $^3\Pi$ and $^3\Sigma$ ($Hg^1S + Zn^3P$)

states are roughly half-ionic [$\text{Hg}^{-2}\text{P} + \text{Zn}^{+2}\text{S}$] and half-covalent [$\text{Hg}^1\text{S} + \text{Zn}^3\text{P}$]. Similarly, the $^1\Pi(\text{Hg}^1\text{S} + \text{Zn}^1\text{P})$ state is an approximately equal mix of ionic [$\text{Hg}^{-2}\text{P} + \text{Zn}^{+2}\text{S}$] and covalent [$\text{Hg}^1\text{S} + \text{Zn}^1\text{P}$] parts, and the more highly excited states also contain a significant ionic character. Thus the ionic states of the system [$\text{Hg}^- + \text{Zn}^+$] and, to a lesser extent [$\text{Hg}^+ + \text{Zn}^-$], do not simply cross the covalent states at various R-values, but instead interact strongly with all the molecular states, at least in the molecular region.

The second group of states is derived from ground-state Hg and excited Zn in the configuration $4s5s(^1,^3\text{S})$. Although no previous Zn_2 data are available, it is reasonably assumed that the $^3\Sigma(\text{Hg}^1\text{S} + \text{Zn}5^3\text{S})$ state is not strongly bound and that the $^1\Sigma(\text{Hg}^1\text{S} + \text{Zn}5^1\text{S})$ state is not very repulsive; avoided crossings can occur between these states and those of the first group.

2.1.2 Hund's Case (c)

The (c)-case curves are estimated first by splitting the case (a) curves into different j components with $|L - S| \leq j \leq L + S$, with splittings intermediate between those of Hg^3P and those of Zn^3P , and then by dividing these further into curves of differing Ω ($|L - \Sigma| \leq \Omega \leq L + \Sigma$) and replacing crossings of curves with like Ω by anticrossings whose

minimal separations are also of the order of the atomic fine-structure splittings. Thus, for example, a curve labeled $^3\Pi$ on the case (a) diagram splits into four curves in case (c) coupling: Two with $\Omega = 0$, one with $\Omega = 1$, and one with $\Omega = 2$.

Preliminary PE diagrams for $\Omega = 0^+$, 0^- , 1 and 2 are shown in Figs. 2.2, 2.3, 2.4 and 2.5, respectively^{15,16}, and will be used in Chapter 4 to interpret the observed fluorescence and excitation spectra.

2.2 Excitation and Decay of the CO^+ , E1, F1, and EO^- States

The transitions between the various spin-orbit states obey the selection rules appropriate to Hund's case (c) coupling for heteronuclear molecules:

$$1. \quad \Delta\Omega = 0, \pm 1 \quad (\Delta J \neq 0 \text{ for } \Omega = 0 \leftrightarrow \Omega = 0) \quad (2.1)$$

$$2. \quad \text{For transitions } \Omega = 0 \leftrightarrow \Omega = 0,$$

$$(+ \leftrightarrow +, - \leftrightarrow -, - \nleftrightarrow +)^{\circ} \quad (2.2)$$

The $CO^+(Hg^1S + Zn^1P)$, E1($Hg^1S + Zn^1P$), F1($Hg^1S + Zn5^3S$), and $EO^-(Hg^1S + Zn5^3S)$ states were populated using the pump and probe method. The pump pulse produced populations of the A1, $A0^-$ and $A0^+$ ($Hg^1S + Zn^3P$) states which became reservoir states, since $A0^-$ is a metastable state and $A0^+$ and A1 are very likely in thermal equilibrium with it. The excitation of the reservoir states may be represented as

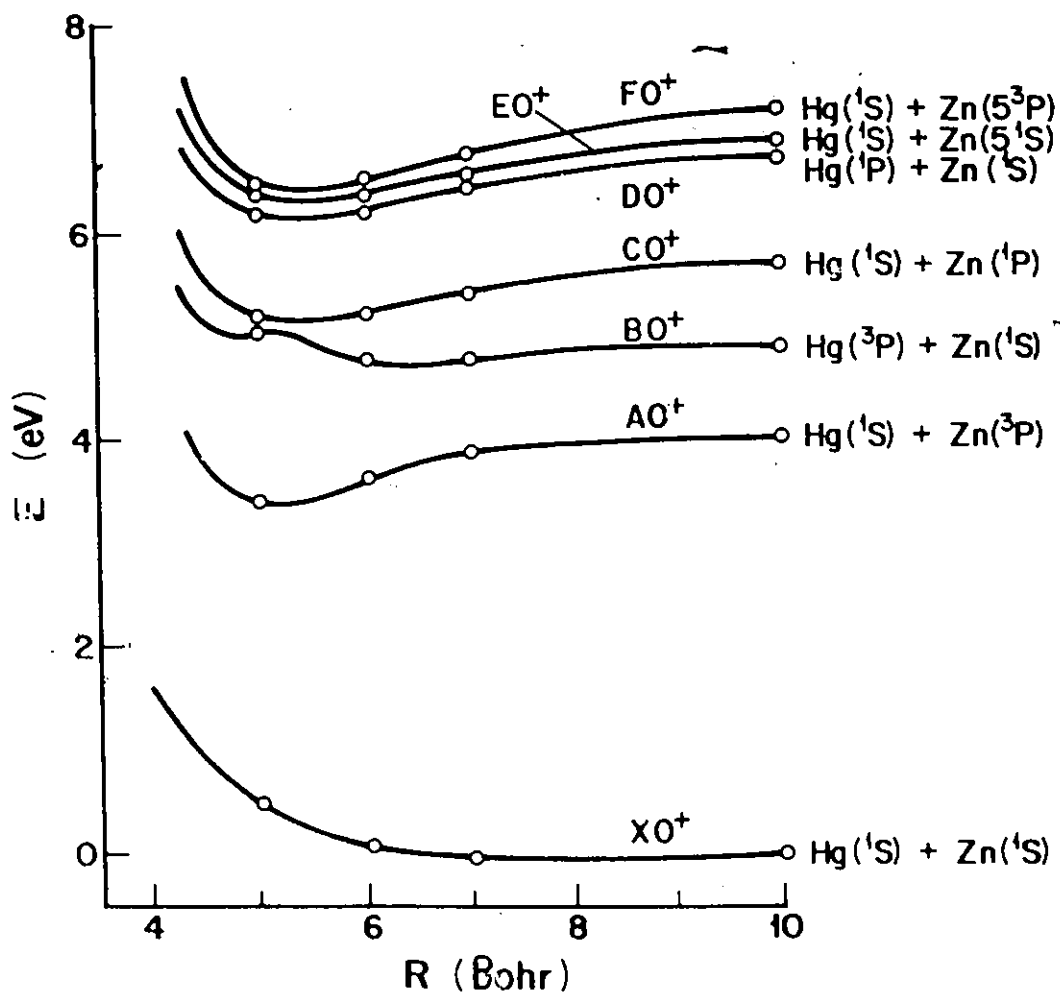


Figure 2.2 PE diagram according to Hund's case (c), showing states with $\Omega = 0^+$.

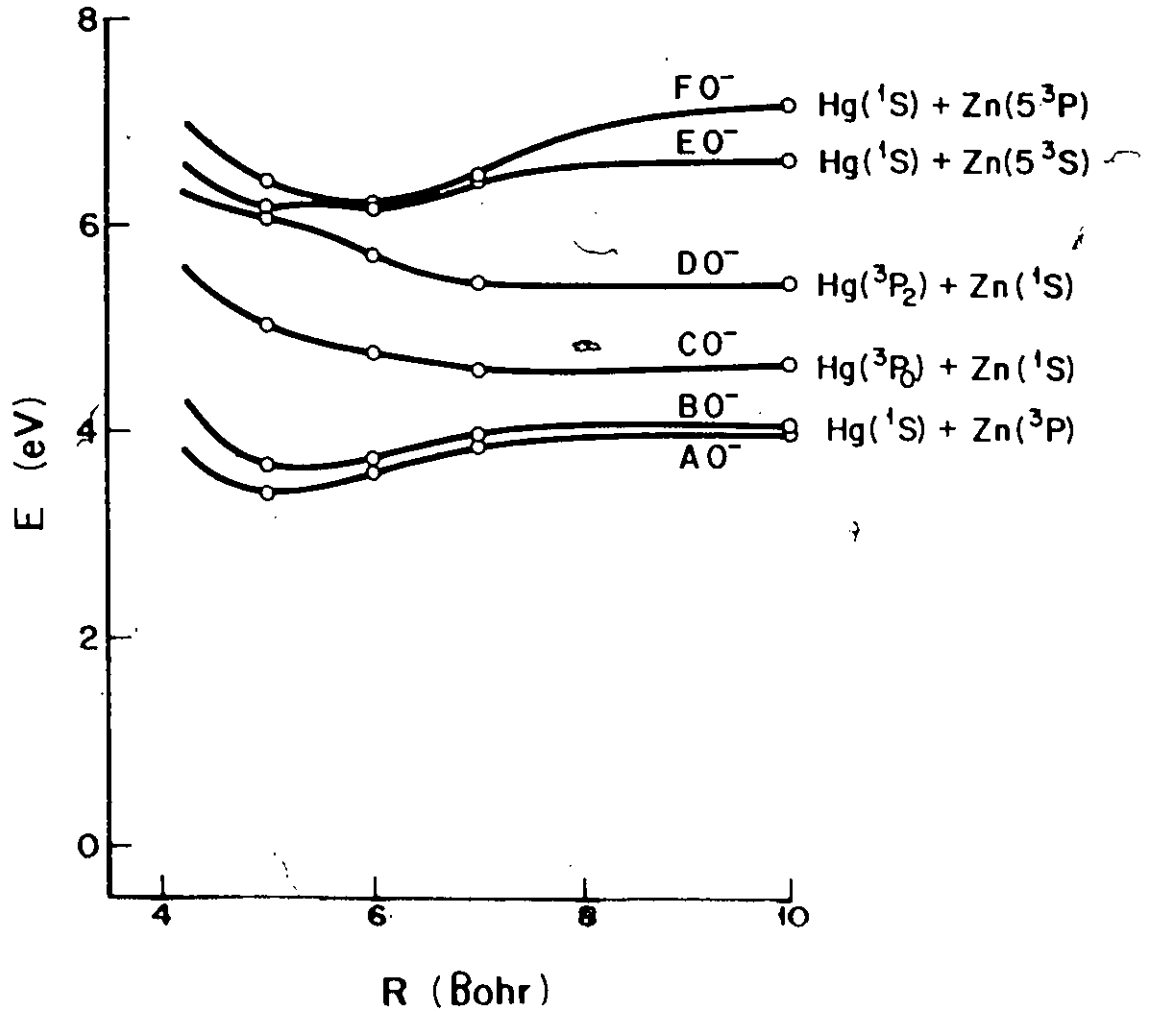


Figure 2.3 PE diagram according to Hund's case (c), showing states with $\Omega = 0^-$.

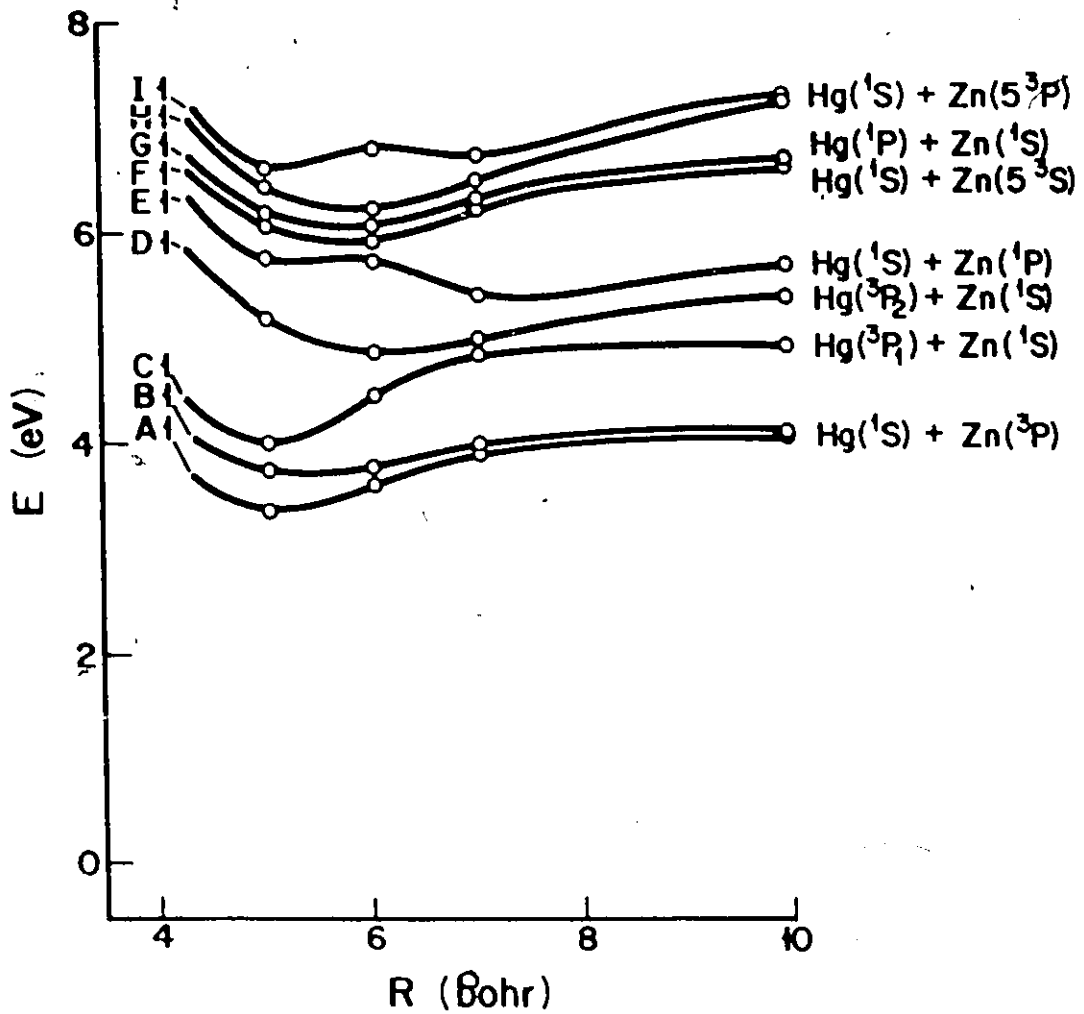


Figure 2.4 PE diagram according to Hund's case (c), showing states with $\Omega = 1$.

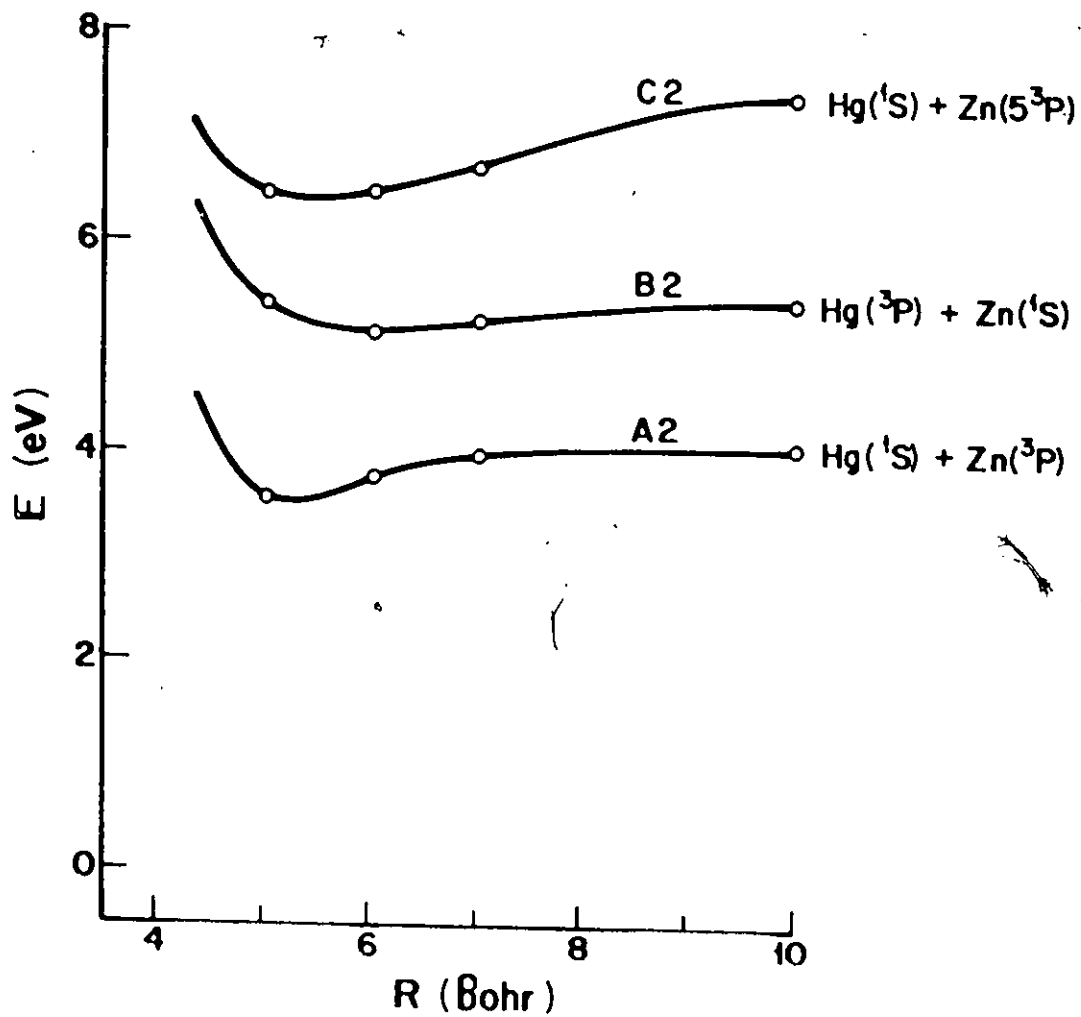
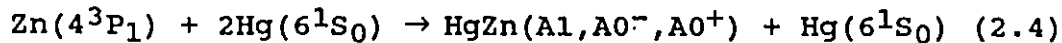
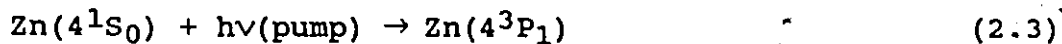
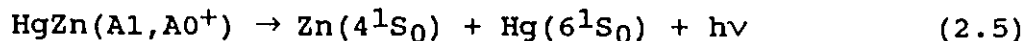


Figure 2.5 PE diagram according to Hund's case (c), showing states with $\Omega = 2$.

follows:

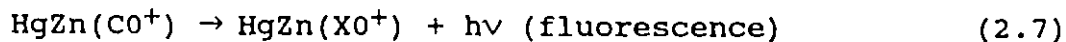
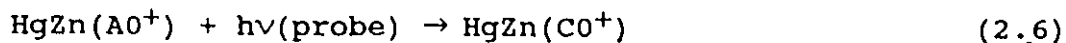


The blue fluorescence band at 4750 Å is due to the bound-continuum transitions from the A0^+ and A1 states to the X0^+ ground state, which can be represented by:



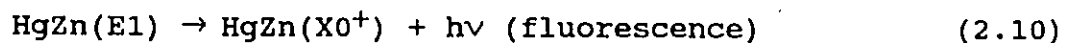
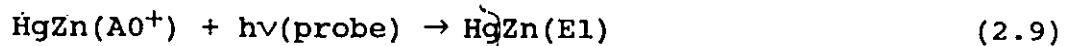
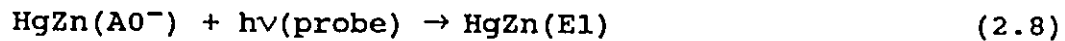
The subsequent probe pulse consisted of laser radiation which was tuned within several spectral regions. Its absorption in the 5200 - 6650 Å region populated many vibrational levels of the C0^+ state, in the 4200 - 4500 Å region it populated low-lying vibrational levels of the E1 and F1 states and in the 4180 - 4310 Å region it populated low-lying vibrational levels of the E0^- state.

The C0^+ state was excited by transitions from the A0^+ state, and was found to decay to the X0^+ repulsive ground state, giving rise to a fluorescence spectrum in the 2380 - 2660 Å region. Its excitation and decay processes may be represented as follows:

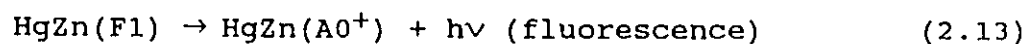
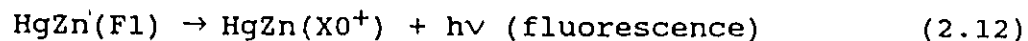
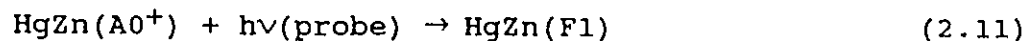


The E1 state was excited by transitions from both A0^- and A0^+ states and decayed to the ground state giving rise

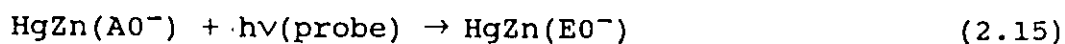
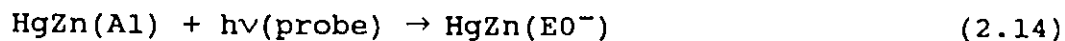
to fluorescence spectra in the 2230 - 2320 Å region. Its excitation and decay processes may be represented as follows:

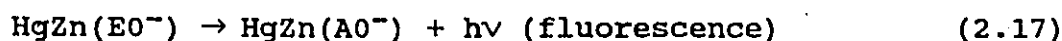
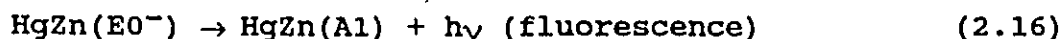


The F1 state was excited only from the A0⁺ state but was found to decay to the ground state by bound-continuum transitions emitting fluorescence in the 2230 - 2320 Å region, and to the A0⁺ state by resonance bound-bound transitions, emitting fluorescence in the 4200 - 4500 Å region. The processes of excitation and decay of the F1 state may be represented by the equations:



Finally, the E0⁻ state was excited from both the A1 and A0⁻ reservoir states, and was found to decay back to these two states, as well as to the B0⁻ state by bound-bound transitions in the 4000 - 4450 Å and 4600 - 4780 Å regions, respectively. The excitation and decay processes may be represented as follows:





2.3 Vibrational Spectra of the HgZn Excimer

2.3.1 The Term Equation

The HgZn molecular fluorescence consists of band spectra resulting from transitions between vibrational levels of electronic states. The total electronic, vibrational and rotational energy of the molecule may be expressed as follows:

$$T = T_e + G(v) + F_v(J) \quad (2.19)$$

where T_e , $G(v)$ and $F(J)$ are the standard terms representing the electronic, vibrational and rotational energies, respectively. In a transition between two electronic states, the frequencies of the emitted spectral components are determined by the difference of the two term values in the upper and lower electronic states²⁶.

$$\begin{aligned} \nu &= T' - T'' \\ &= (T_e' - T_e'') + (G'(v') - G''(v'')) + (F_v(J') - F_v(J'')) \end{aligned} \quad (2.20)$$

or

$$\nu = \nu_e + \nu_v + \nu_r \quad (2.21)$$

where the single-primed superscripts relate to the upper state and the double-primed superscripts to the lower state.

In the case of the HgZn molecule, ν_r is very much smaller than ν_v and may be neglected, and equation (2.21) may be written as follows²⁶

$$\begin{aligned} v = v_e + [(v' + 1/2)\omega_e' - (v'' + 1/2)\omega_e''] \\ - [(v' + 1/2)^2\omega_e'x_e' - (v'' + 1/2)^2\omega_e''x_e''] \\ + \text{higher-order anharmonic terms.} \end{aligned} \quad (2.22)$$

where $v = 0, 1, 2, \dots$ is the vibrational quantum number, ω_e is the frequency (in cm^{-1}) of (simple harmonic) oscillations of infinitesimal amplitude about the equilibrium bond length, and $\omega_e x_e$ is the first-order anharmonicity.

Because of the anharmonicity, there are two important differences from the harmonic oscillator. The vibrational transitions are no longer restricted to $\Delta v = \pm 1$ but transitions corresponding to $\Delta v = 0, \pm 2, \pm 3, \pm 4, \dots$ are also allowed. In addition, the separations between the vibrational levels are no longer constant but decrease as v increases by amounts dependent on the magnitude of $\omega_e x_e$.

Equation (2.22) may be used to calculate, from the observed spectrum, the harmonic frequency ω_e and the anharmonicity $\omega_e x_e$ as well as the zero-point energy and the energy separation between the $v = 0$ levels of the two electronic states participating in the transition.

The rotational energy term value can be expressed by a formula similar to that of the vibrational term value²⁶.

$$F_v(J) = B_v J(J + 1) - D_v J^2(J + 1)^2 + \dots \quad (2.23)$$

where

$$B_v = B_e - \alpha_e(v + 1/2) \quad (2.24)$$

$$B_e = h/(8 \pi^2 c \mu r_e^2) \quad (2.25)$$

$$D_v = 4B_v^3/\omega_e^2 \quad (2.26)$$

B_e is the rotational constant for a rigid rotator.

α_e is the correction factor for the rotational constant due to the vibrational distortion.

D_v is the centrifugal stretching constant.

The frequencies of the spectral lines in a specific band can then be determined by the equation ;

$$\nu = \nu_0 + B_v' J'(J' + 1) - B_v'' J''(J'' + 1) \quad (2.27)$$

where

$$\nu_0 = \nu_e + \nu_v, \quad (2.28)$$

and the terms containing the D_v terms are neglected.

Transitions between rotational levels are governed by the selection rule :

$$\Delta J = 0, \pm 1 \quad (J' = 0 \nleftrightarrow J'' = 0) \quad (2.29)$$

and therefore equation (2.26) may be split into three equations corresponding to the P, Q, and R branches.

$$P(J) = \nu_0 - (B_v' + B_v'')J + (B_v' - B_v'')J^2 \quad (2.30)$$

$$Q(J) = \nu_0 + (B_v' - B_v'')J + (B_v' - B_v'')J^2 \quad (2.31)$$

$$R(J) = \nu_0 + 2B_v' + (3B_v' - B_v'')J + (B_v' - B_v'')J^2 \quad (2.32)$$

2.3.2 The Bound-Continuum Spectra

The relative intensities of the vibrational components in a fluorescence band spectrum are governed mainly by the

Franck-Condon (FC) factors which are determined by the square of the integral²⁶:

$$\int \psi'(r)\psi''(r)dr \quad (2.33)$$

where $\psi'(r)$ and $\psi''(r)$ are the wave functions of the upper and lower vibrational levels, respectively. For bound-continuum decays, $\psi' = \psi'(r,E)$ represents a wave function of a bound vibrational energy level, and $\psi'' = \psi''(r,E)$ represents a wave function of the continuum of the wave functions of the unbound lower state since the argument E , which is the kinetic energy, is continuous²⁷. Accordingly, there will be a continuum of wavefunctions belonging to the lower repulsive state, and the shape of each wave function will consist of a broad maximum at the turning point on the PE curve and a rapid oscillation towards larger r . Consequently, for every $\psi'(r)$, there will be a continuum of values of the integral (2.33), which will qualitatively depict the probability density distribution²⁸ of the particular upper vibrational level, as shown in Fig. 2.6. The integral has significant non-zero values when two conditions are satisfied:

1. The local de Broglie wavelengths corresponding to the 'upper' and 'lower' wave functions are equal,

$$\lambda' = \lambda'' = h/(2\mu E)^{1/2} \quad (2.34)$$

(where μ is the reduced mass of the molecule). This is equivalent to the classical Franck-Condon principle which states that the positions and momenta of the nuclei do not

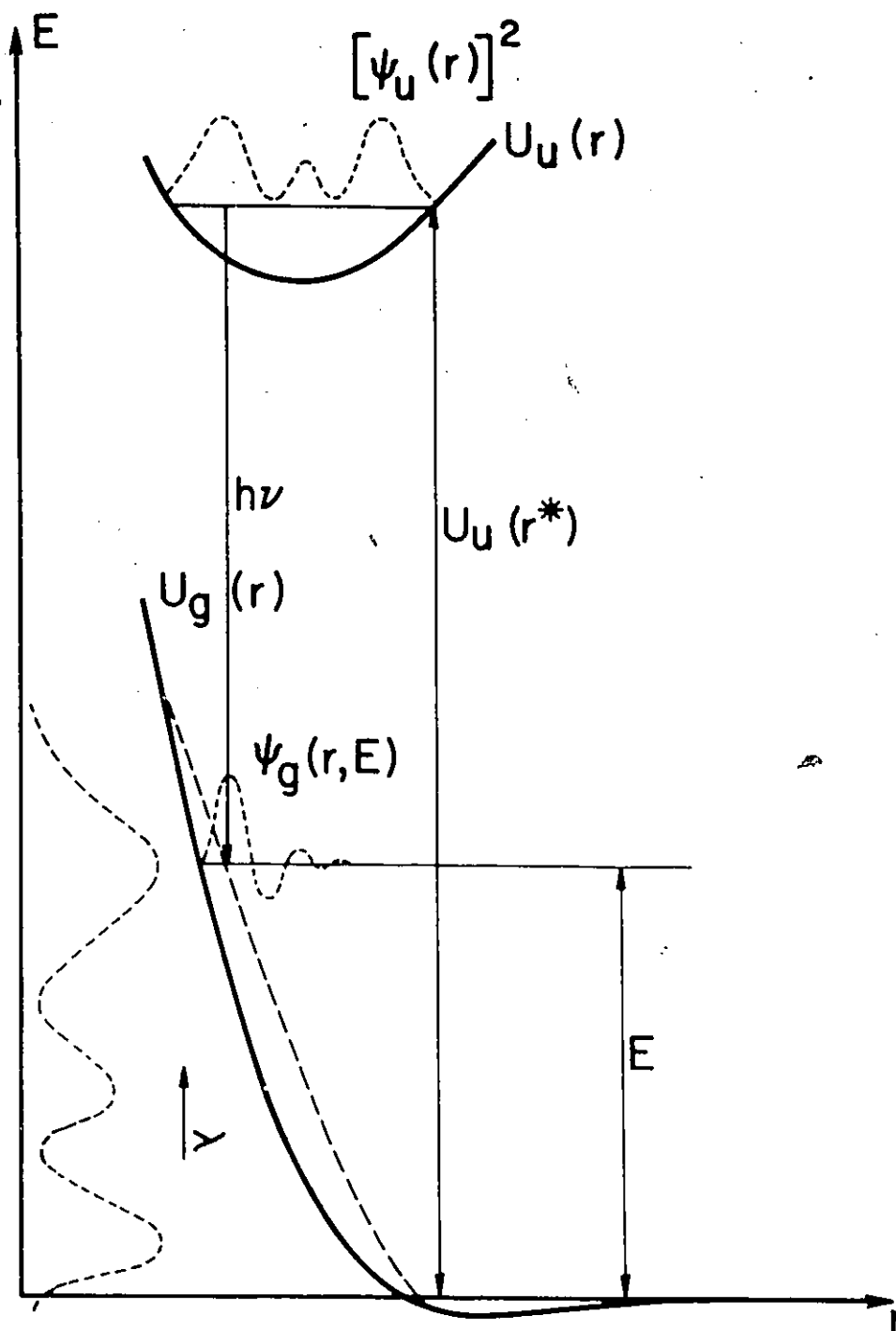


Figure 2.6 The formation of a Condon internal diffraction pattern (projected on the E axis) in a bound-continuum fluorescence spectrum. The subscripts u and g refer to upper and lower states, respectively. The dashed ground-state PE curve allows for conservation of kinetic energy.

change in a transition, and thus the kinetic energy is conserved i.e.

$$E - U''(r) = U'(r^*) - U'(r) \quad (2.35)$$

where $U''(r)$ and $U'(r)$ are the potential energies of the lower and upper states, respectively, and r^* corresponds to the turning points of the particular vibrational wave function.

2. The phases of the two wave functions match or are shifted by $\pm\pi$ with respect to each other. The integral (2.33) has minima when the phases of both wave functions are shifted by $\pm\pi/2$. The resulting intensity distribution consists of two broad maxima which correspond to the classical turning points of the nuclear vibration, and a number of subsidiary maxima. The total number of maxima in the pattern may be used to identify the vibrational quantum numbers of the bound state since it is equal to $v + \frac{1}{2}$.

2.3.3 The Bound-Bound Spectra

The relative intensities of the vibrational components in a bound-bound fluorescence band spectrum are also governed mainly by the FC factors determined by the integrals (2.33) but, in this case, both $\psi'(r)$ and $\psi''(r)$ are wave functions of bound vibrational levels. Therefore, some vibrational components may be more intense than others, depending on the degree of overlap between the two wave

functions²⁶. Usually the distribution of intensities among the different transitions originating from a $v' = 0$ level to various v'' levels, exhibits a bell-like distribution, which may or may not be symmetric, with the maximum at the component which corresponds to the largest value of the integral. The distribution of intensities among transitions originating from a $v' = 1$ level to various v'' levels, on the other hand, goes through a minimum, which corresponds to the minimal value of the integral. A simple modeling calculation² of the vibrational intensity distribution in the fluorescence spectra may be used to make estimates of $\Delta r_e = r_e' - r_e''$ (the difference between the internuclear separations at the potential minima of the two states).

In a bound-bound excitation spectrum, which represents upward transitions from a particular reservoir state to a particular excited state, the relative intensities of the vibrational components are also affected by the Boltzmann vibrational distribution which modifies the relative intensities arising from the FC factors. Under conditions of thermal equilibrium, the population of a vibrational level with quantum number v can be expressed as²⁶

$$N_v = (N/Q_v) \exp (-G_0(v)hc/kT) \quad (2.37)$$

where

$$Q_v = 1 + \exp (-G_0(1)hc/kT) + \exp (-G_0(2)hc/kT) + \dots \quad (2.38)$$

is the partition function and N is the total number of molecules. Accordingly, the Boltzmann factor plays an important role in diminishing the intensities of components arising from (upward) transitions originating from higher v'' levels.

Because of the large reduced mass μ , the vibrational spectral lines were broadened by the unresolved, densely-spaced, rotational components. This broadening made it impossible to measure the frequencies of the vibrational components with sufficient precision to determine higher-order vibrational anharmonicity (beyond $\omega_e x_e$) or the rotational constants.

Nevertheless, taking advantage of the rotational selection rules, it was in some cases possible to deduce, from the shapes of the vibrational components in an excitation band, the relative ordering of the rotational constants B' and B'' . This, in turn, provided an indication of the relative r_e values associated with the states involved in the transition, since $B \propto 1/r^2$. When the vibrational components exhibit steep leading edges on the short-wavelength sides and are degraded towards longer wavelengths, this indicates that rotational transitions associated with large J 's lie at energies lower than those associated with small J 's (which, in this case, are close to the band head) and the quadratic term in J'' (see equations (2.30-32)) is negative, i.e. $B' < B''$ and $r_e' > r_e''$. On the other hand, if the steep leading

edges appear on the long-wavelength sides and the degradation is towards shorter wavelengths, then $B' > B''$ and $r_e' < r_e''$.

3 EXPERIMENTAL

3.1 Description of the Apparatus

3.1.1 General

The arrangement of the apparatus is shown schematically in figure 3.1. The Hg-Zn vapour mixture, contained in a sealed-off quartz fluorescence cell, was irradiated with collinear pulsed 'pump' and 'probe' laser beams directed antiparallel to each other and timed to produce a 450-ns pump-probe delay. The resulting fluorescence, emitted at right angles to the laser beams, was dispersed by a monochromator and detected by a photomultiplier. The output signals from the photomultiplier were sampled by a 1024-channel transient digitizer and stored in a microcomputer which carried out signal-averaging. Both the monochromator and the probe laser could be scanned, by computer-controlled stepper motors, to produce the various fluorescence and excitation spectra.

3.1.2 The Pump Laser

The pump-laser beam was produced by pumping an in-house built two-stage dye laser with the second harmonic (5320 Å)

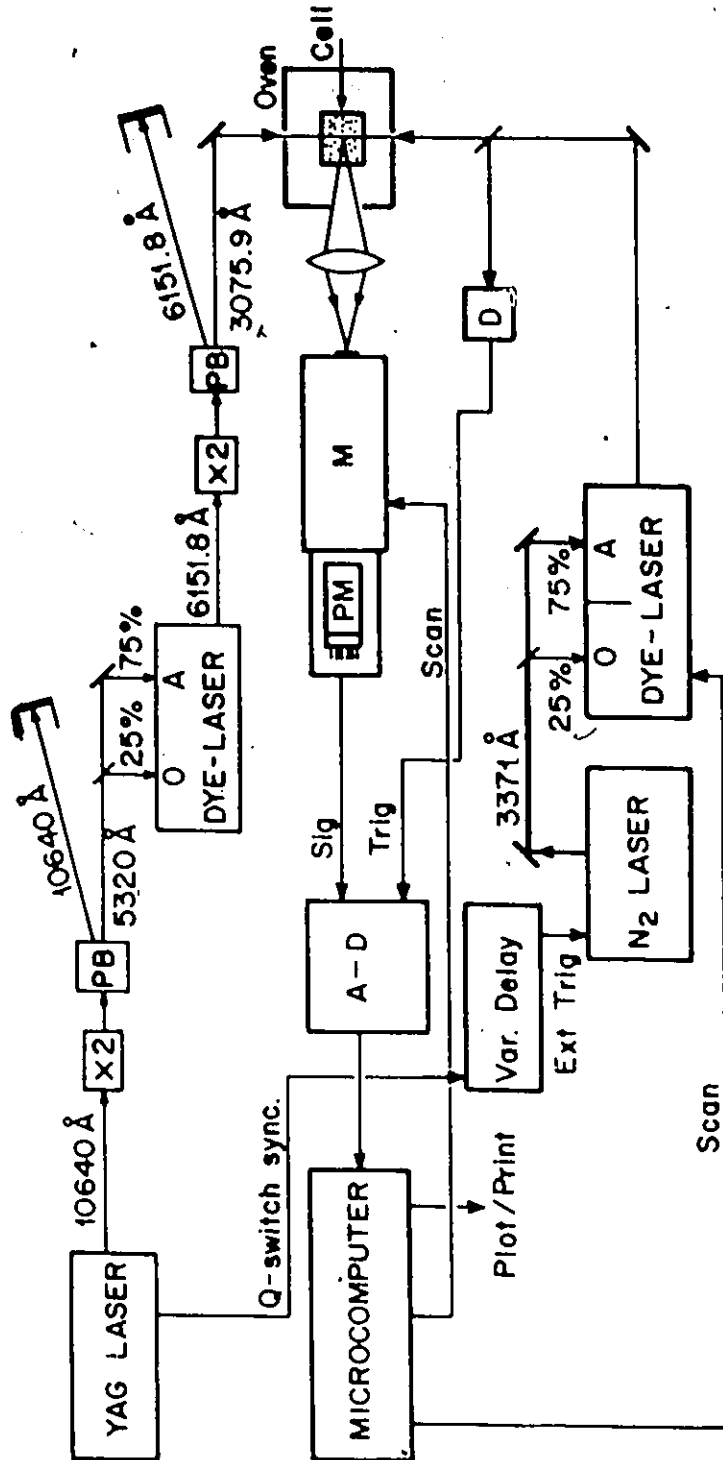


Figure 3.1 Schematic arrangement of the experiment. PB, Pellin-Broca prisms; D, photodiode; M, monochromator; A-D, transient digitizer.

of a Quanta-Ray DCR-1A Nd:YAG (Neodymium: Yttrium Aluminum Garnet) laser. The fundamental laser output at 10640 Å was produced in an unstable (convex-concave) optical resonator and was amplified when necessary by a power amplifier stage. The laser was always operated in the Q-switched mode, by means of an electro-optical Q-switch (Pockels cell), in order to produce short pulses of high-peak power needed for the efficient generation of the second harmonic.

The second harmonic at 5320 Å was produced using an angle-tuned KD*P (Potassium Dideuterium Phosphate) frequency-doubling crystal. The fundamental and the second harmonic laser outputs, which were generated collinearly, were angularly separated using a Suprasil quartz Pellin-Broca prism, oriented to reduce losses due to Fresnel reflection. The unused part of the IR beam was dissipated in a beam-dump and the 5320 Å laser output was directed, by beam splitters and two antireflection-coated cylindrical quartz lenses, to side-pump a two-stage dye laser operated with Rhodamine 640 in methanol (5×10^{-4} M). The first stage (oscillator), consisted of a diffraction grating/mirror cavity, which included a quad-prism beam expander²⁹ and a magnetically stirred dye cell, and received 25% of the total 5320 Å beam intensity. The diffraction grating, which could be rotated manually by means of a micrometer, was kept tuned at an angle which produced laser radiation at 6151.8 Å. The second stage received 75% of the total 5320 Å beam intensity

and acted as an amplifier. It consisted of a second magnetically stirred dye cell, into which the output laser beam from the oscillator was focused by means of a $f = 10$ cm antireflection-coated achromatic lens. The amplified laser output was subsequently frequency-doubled with a KDP" C" (Potassium Dihydrogen Phosphate) crystal to produce the 3075.9 Å laser radiation for the excitation of Zn atoms to the 4^3P_1 state. This 3075.9 Å laser beam (1 mm in diameter) was directed by aluminum mirrors and quartz lenses to pass through the fluorescence cell inside the oven.

When the 5320 Å second-harmonic laser radiation was generated at an energy of 12 mJ per pulse, the resulting 6151.8 Å dye-laser output was found to have an energy of 0.7 mJ per pulse, and the final output at 3075.9 Å had an energy of 0.05 mJ per pulse.

3.1.3 The Probe Laser

The probe laser consisted of a two-stage dye laser excited with an in-house built N_2 -laser. The N_2 -laser had a transverse discharge resonator cavity 1 m long with a flat dielectrically coated total reflector at one end and a flat uncoated Suprasil output window at the other. Pure N_2 gas was admitted to the cavity at a pressure of about 75 Torr. The output laser beam consisted of 3371 Å radiation, had a rectangular cross-section (3.2 cm x 0.6 cm) and a pulse

width of about 10 ns. The N_2 -laser was triggered externally by the Q-switch pulse of the YAG laser after being delayed by 450 ns. Thus the repetition rate of the N_2 -laser was equal to that of the YAG laser (usually set at 10 Hz.)

The N_2 -laser output was used to pump a two-stage dye laser similar to that described above, in which the diffraction grating was tuned by a sine-drive²⁹ activated by a computer-controlled stepper motor. The steps corresponded to constant wavelength increments of 1/24, 1/20 or 1/16 Å, depending on the order in which the grating was operated. The linearity of the scanning steps with respect to the wavelength increment, over a particular spectral range, was checked by means of an optogalvanic cell which consisted of a miniature Neon discharge lamp. An aperture 1 mm in diameter was located between the oscillator and the amplifier stages, and another aperture, 3 mm in diameter was located in the path of the output dye laser to block out the undesired superradiance which otherwise would scatter off the cell walls and produce spurious stray-light signals.

The various laser dyes (supplied by Exciton Chemical Company) dissolved in the appropriate solvents, which were used to produce laser radiation in the 5000-6500 Å and 4000-4700 Å regions, are listed in Table 3.1. Under typical conditions of the pump-and-probe experiments, the energy per

TABLE 3.1 Laser dyes used in the experiments

Laser Dye	Solvent	Concentration (M)	Wavelength Range (Å)
Rhodamine 640	Ethanol	5×10^{-3}	6250-6650
Rhodamine 610	Ethanol	3.8×10^{-3}	5950-6300
Rhodamine 6G	Ethanol	5.3×10^{-3}	5750-6000
Coumarin 540	Ethanol	1×10^{-2}	5200-5800
Coumarin 500	Ethanol	1×10^{-2}	5100-5350
Coumarin 460	Ethanol	4.5×10^{-3}	4420-4700
Coumarin 440	Ethanol	5×10^{-3}	4280-4550
Stilbene 420	Methanol	1.8×10^{-3}	4120-4320
DPS	P-dioxane	$< 1.2 \times 10^{-3}$	4050-4180

pulse of the 4320 Å dye laser output (Coumarine 440 in ethanol) was measured to be 0.02 mJ. When measuring the linearity of the probe laser intensity against the intensity of the LIF signal, a series of identical neutral-density filters was inserted in the path of the dye-laser output. The dye-laser output wavelengths were measured with a precision of ± 0.4 Å in the red region and of ± 1 Å in the blue region, using an in-house built Fizeau wavelength meter³⁰.

3.1.4 The Fluorescence Cell and Oven

The fluorescence cell had a cylindrical shape and was constructed of non-fluorescing Suprasil quartz. It was 7 cm long and 1.8 cm in diameter, and had a 13 cm-long side arm. It was fitted with two end windows (2 mm thick) perpendicular to the cell axis.

When preparing the Hg-Zn mixture, the cell was connected to a Pyrex vacuum-distillation system by means of a graded seal. A vacuum of 10^{-8} torr was produced by an Edwards E02 oil diffusion pump filled with Santovac 5 fluid and backed by a Speedivac ES35 rotary pump. The pressure was measured by a CVC GIC-028-2 ionization gauge connected to a Bendix GIC-300 control unit. The diffusion pump was connected to the vacuum system by a cylindrical glass stopcock lubricated with Apiezon-L grease. The diffusion pump had a liquid

nitrogen cold trap to prevent backstreaming of the fluid into the fluorescence cell. A block diagram of the vacuum system is shown in Fig. 3.2.

A U-tube liquid-nitrogen cold trap was connected in-line close to the fluorescence cell for use during the distillation of Hg. This served two purposes: it trapped traces of O_2, CO_2, H_2O, \dots inside the vacuum system allowing it to reach an optimum vacuum, and it condensed any Hg vapour that might have escaped during distillation and prevented contamination of the vacuum system by mercury.

Figure 3.3 shows a schematic diagram of the oven. It consisted of two compartments, one of which housed the main body of the fluorescence cell and the other contained the side arm. The main compartment was constructed of 3 mm thick stainless steel sheets. Its top cover, which could be detached when necessary, had two holes through which passed the wires of two thermocouples. The side-arm compartment was cylindrical, 10 cm in diameter, and was made of brass. The whole oven was placed inside a jacket made of 1 mm-thick stainless steel plates and was attached to a 20 x 10 cm stainless steel base 6.3 mm thick. The jacket was filled with commercial ceramic 'blankets' capable of withstanding temperatures up to 1500 $^{\circ}C$. This provided a convenient heat insulation as well as a stable temperature over a period of several weeks. The main oven compartment and the jacket both had three circular apertures through which light passed

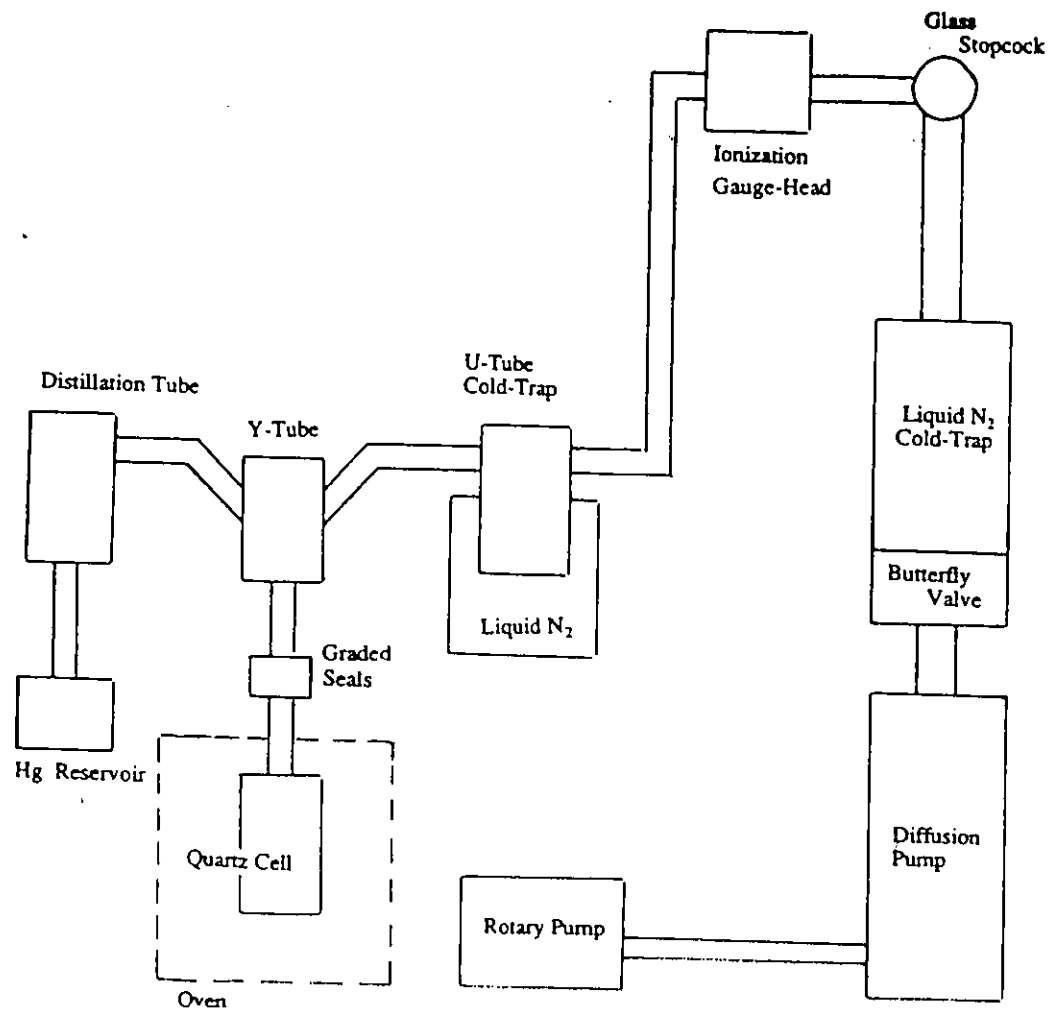


Figure 3.2 A block diagram of the vacuum system.

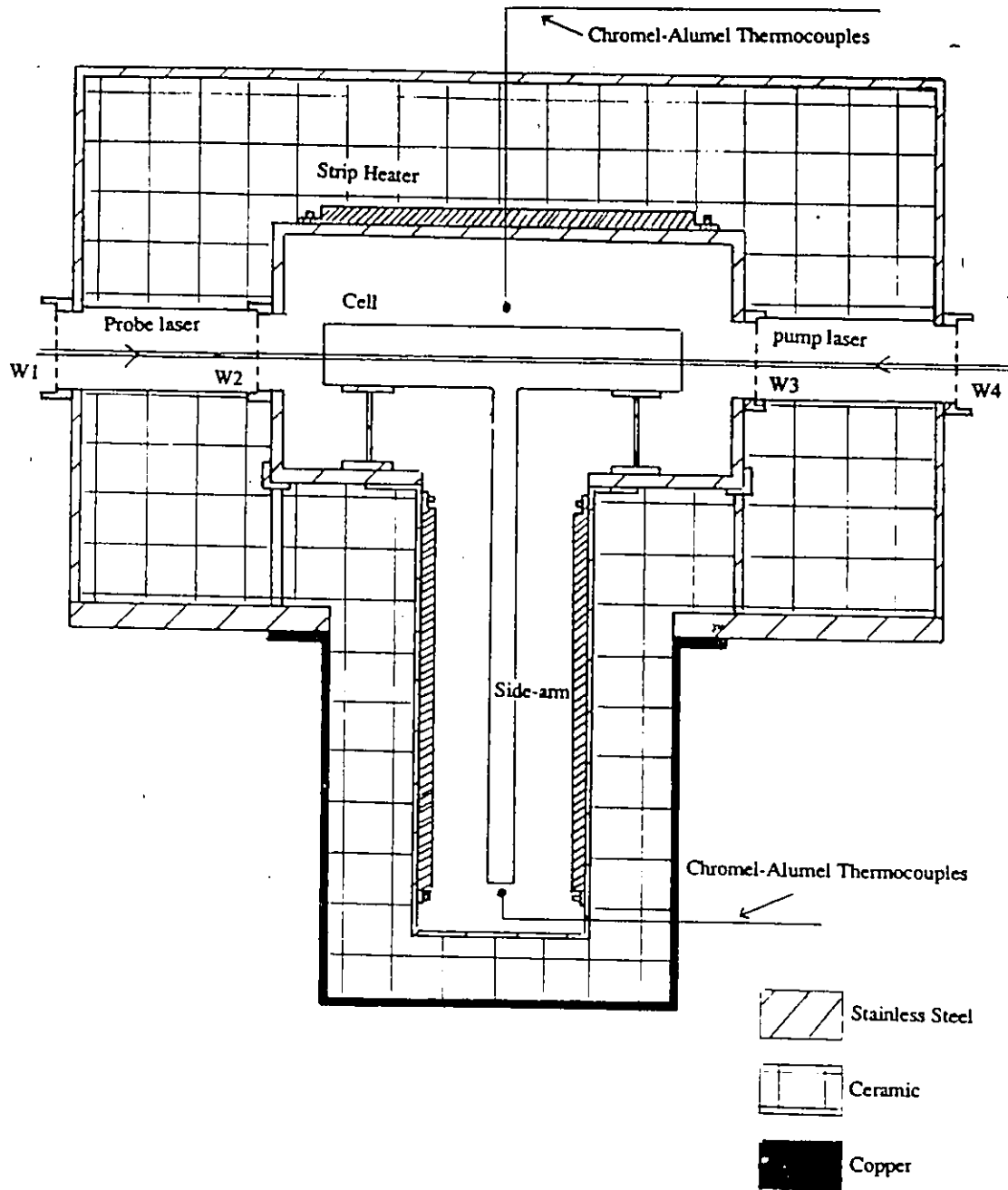


Figure 3.3 A cross section of the oven used in the experiment. The whole assembly is covered by an aluminum box. W1, W2, W3 and W4 are quartz windows.

into and out of the cell. The apertures were closed off with Suprasil windows to reduce heat loss by convection. The whole oven assembly, including the jacket, was mounted inside a large box made of 5 mm thick aluminum sheets which provided additional insulation.

Each of the two oven compartments was separately heated by three ac General Electric strip heaters connected in parallel, which had an effective resistance of 27Ω . The heaters had a maximal operating temperature of 650°C . They were mounted on the outer walls of both compartments, to make them easily accessible for minor repairs without opening the whole oven. They had the additional advantage over helical heating elements made of high-resistance wire, that asbestos or ceramic padding inside the oven was not necessary. Variac autotransformers connected to 120 V wall outlets were used to power the strip heaters separately. The various electrical connections between the strip heaters inside the oven and between the heaters and the Variac transformers were made of ceramic-beaded stainless steel wires which resisted corrosion at high temperatures.

Two chromel-alumel thermocouples were used to monitor the temperature of the main oven (near but not touching the body of the cell) and of the bottom of the side arm, and were connected to two digital voltmeters. Leeds and Northrup thermocouple conversion tables were used to convert the voltage readings into temperatures.

3.1.5 The Detection and Data Acquisition System

The fluorescence, emitted at right angles to the laser beams, was focused by an $f = 20$ cm spherical quartz lens onto the entrance slit of a monochromator. Two different monochromators were used during the experiments, depending on the wavelength of the emitted fluorescence. The (I.S.A., H-20) Jobin-Yvon 20-cm monochromator, equipped with a 1200 l/mm concave holographic grating, had a maximal resolution of about 4 Å at 2000 Å and an effective speed of $f/4.2$. A calibration of the spectral response of this monochromator revealed the existence of a grating "ghost" in the 4900-5100 Å region. The calibration was performed with a GE 200 W QI130 quartz halogen lamp, which was calibrated by NRC laboratories for spectral irradiance from 3000 Å to 8000 Å, in 50 Å steps. The monochromator was fitted with an EMI 9816QB photomultiplier which had a nominal rise time of 2.2 ns and a relatively high quantum efficiency ($\approx 30\%$) in the ultra-violet spectral region which encompassed the observed bound-continuum fluorescence. The photomultiplier had an extended S-20 photocathode and a 14-dynode electron multiplier, and was powered by an Ortec 456 power supply. Since it was found that a potential difference of 1.7-1.8 kV was sufficient to obtain a satisfactory signal, no preamplification was used. The photomultiplier was cooled by an EMI thermoelectric cooling unit to reduce the dark noise.

An I.S.A. HR-320 monochromator was used when registering the bound-bound fluorescence in the blue spectral region which also contained the long-lived broad fluorescence band due to the pump pulse. The monochromator was equipped with a 1800 l/mm grating and had a maximal-resolution of 0.5 Å at 3131 Å. Its entrance and exit slits were continuously adjustable and its effective speed was f/4. The monochromator was equipped with a thermoelectrically cooled RCA C31034 photomultiplier; its voltage-divider was connected to an Ortec 456 power supply, it had a GaAs photocathode, eleven high-stability CuBe dynodes and a quantum efficiency of about 14% at 5500 Å. The potential difference across the photomultiplier was maintained at a value 1.7-1.8 kV, and to achieve a satisfactory signal level its output was amplified 200 times using an Ortec 9302 amplifier-discriminator.

Both monochromators were scanned by computer-controlled stepper motors in constant wavelength increments, the smallest of which was 0.5 Å.

The photomultiplier signal was registered by a Biomation model 6500 waveform analyzer which was used as a transient digitizer. It had 1024 channels in which the data were stored in the form of 6-bit binary words. Its highest time-resolution was 2 ns/channel and the lowest was 1 s/channel. The waveform analyzer was triggered externally by the probe laser pulses, by directing a small fraction of the probe

laser beam into a fast EG&G photodiode whose output triggered the waveform analyzer. The digitized output from the waveform analyzer was then sent to a Commodore PET[™] model 2001 microcomputer which carried out the signal averaging of the incoming data using a machine-language program³¹. The necessary input parameters (the number of channels per scan, of laser pulses per channel, of pulses per increment, the wavelength setting, and the wavelength limits of the scan) were entered into the program. While the program was running, it displayed on the monitor a periodically updated histogram of the computer-memory contents along with the corresponding normalized number of counts. The histogram and number of counts were then plotted and printed on an EPSON model MX-80 dot-matrix printer for further analysis.

3.2 Experimental Procedure

3.2.1 General

The Hg-Zn vapour mixture in the fluorescence cell was maintained at 840 K, with the side-arm at 780 K. It was irradiated with pump pulses of wavelength, 3075.9 Å, tuned to the Zn $4^3P_1 \leftarrow 4^1S_0$ atomic transition. This caused the formation of HgZn in an excited (metastable) state, which had a relatively low rate of quenching by Hg ($5.5 \times 10^{-15} \text{ cm}^3/\text{s}$)¹, and a long effective lifetime (6.1 μs); this

allowed enough time for probing higher excited states. Probing was affected by the variable-wavelength probe pulses which were delayed relative to the pump pulses, until the density of the metastable HgZn molecules reached a maximum. The fluorescence signals resulting from the decay of the various excited states were observed at right-angles to the direction of excitation and were analyzed using techniques of time-resolved fluorescence spectroscopy.

3.2.2 Preparation of the HgZn Fluorescence Cell

The composition of Hg-Zn mixture used in the experiments was so arranged that the mole fraction of mercury exceeded 0.95. The quantity of mercury was also appropriately adjusted, that at temperatures above 600 K it was all in the vapour phase at a density of 1.9×10^{19} atoms/cm³. Thus the pressure of mercury vapour at temperatures above 660 K increased linearly with temperature and did not exceed moderate values.

The quartz cell was first washed with a dilute solution of HF, rinsed repeatedly with distilled water and dried, and then 0.022 g pure zinc granules (99.99% purity) was placed inside it. It was then attached by means of graded seals to the lower end of a Y-tube in the glass section of the vacuum

system shown in Fig. 3.4. 0.162 g of doubly-distilled mercury was placed in a sealed-off ampoule inside a distillation tube which was connected to one (upper) branch of the Y-tube. The other branch of the Y-tube was connected through the cold-trap to the vacuum system. When a vacuum of 1×10^{-8} Torr was reached, the quartz cell was outgassed by baking it for two days at 600°C in an electrically heated oven. The three constriction areas were also well degassed by heating them with a torch to temperatures near the softening point of pyrex or quartz. This process was repeated several times to reduce the outgassing of potential contaminants after sealing-off.

When the distillation process began, the valve connecting the diffusion pump to the glass section of the vacuum system was closed, and the cold-trap was immersed in a bath of liquid nitrogen to condense the remaining gases and to stop the escaping mercury vapour from contaminating the system. The ampoule containing the mercury was opened with a magnetic breaker and the mercury was slowly distilled into the cell with the aid of a heating tape. The Y-tube was then sealed off at the constrictions, and the quartz cell was sealed off at the constriction in the side arm.

Since the HgZn amalgam, formed at such high temperatures, was found to deviate from ideal activity by less than 2%¹ the vapour pressures of mercury and zinc above the amalgam

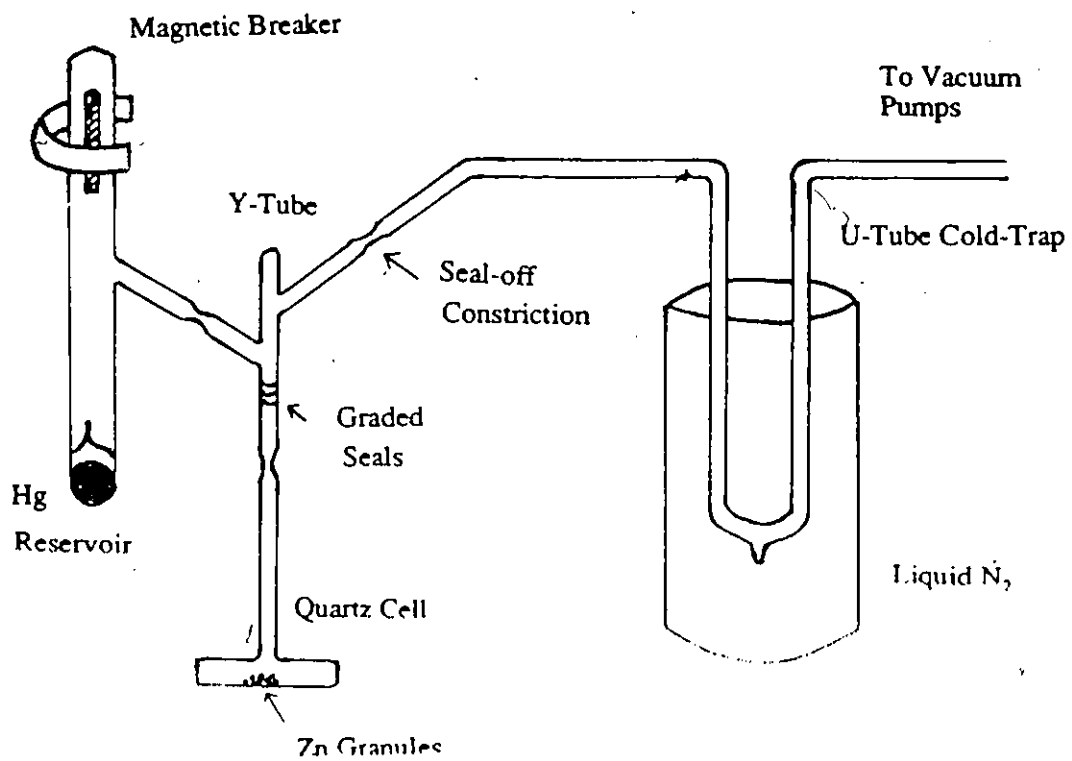


Figure 3.4 Schematic diagram of the distillation chain.

were calculated by using the standard temperature-vapour pressure tables³² for pure mercury and zinc which incurred errors of less than 5%.

The amount of mercury transferred to the quartz cell was estimated to be 0.12 g. This was done by carefully weighing the amount of mercury which escaped during the distillation and was deposited as a thin film on the inside walls of the cold-trap. At the side-arm temperature of 780 K and main cell temperature of 840 K, the density of Hg was estimated to be 1.9×10^{19} atoms/cm³ and that of Zn 1.8×10^{16} atoms/cm⁻³. Unlike alkali-based systems, the HgZn amalgam does not attack glass, quartz, insulators or optical materials which makes it much easier to handle.

In all the experiments conducted in this work, I used a single fluorescence cell, with a fixed composition of the Hg-Zn mixture. The temperature of its side-arm, which controlled the densities of Hg and Zn and thus of the HgZn molecule, was kept fixed during all the experiments except when the relative formation rate of the excimer was studied.

3.2.3 Registration of the Fluorescence Spectrum Excited with a Single Laser

The profile of the blue fluorescence band, excited with the pump laser alone, was recorded by scanning the monochromator in the range 3800-5400 Å and using a 'boxcar' time-

averaging method. Ten fluorescence pulses following ten pump-laser pulses were digitized, time-integrated, and accumulated in the computer memory channel corresponding to the wavelength setting of the monochromator. The computer then advanced the monochromator wavelength setting by 10 Å and the procedure was repeated throughout the wavelength range. After completion of the scan, the monochromator was reset to its initial position and the whole scan was repeated until a satisfactory signal-to-noise ratio was achieved. All 1024 channels (each corresponding to 2 ns) of the transient digitizer were used and the resulting spectrum was represented as a plot of the relative fluorescence intensity against scanned wavelength. The process was repeated under the same experimental conditions, using the standard quartz halogen lamp, and the profile of the fluorescence band was corrected for the spectral response of the monochromator and photomultiplier.

The time-evolution of the fluorescence band was registered by setting the monochromator at 4750 Å and recording, with the transient digitizer, the intensity of the fluorescence signal in relation to time following the pump-laser pulse. This procedure was repeated and the spectra were summed in the computer until a satisfactory signal-to-noise ratio was obtained. The decay of the fluorescence was recorded in an extended time span, using

1024 channels (each corresponding to 10 ns). The rise time, on the other hand, was studied by using 1024 channels (each corresponding to 2ns) in the transient digitizer.

3.2.4 The Pump-and-Probe Experiments

The pump and probe laser beams were directed collinearly and antiparallel to each other inside the HgZn fluorescence cell, and the fluorescence was observed at right-angles to the laser beams. The overlap of the laser beams and the position of the lens which focused the resulting fluorescence onto the entrance slit of the monochromator, were found to be critical in achieving a satisfactory fluorescence intensity. The following procedure, shown in Fig 3.5, was used to ensure optimal alignment. The probe-laser beam was directed through the cell by means of mirror 3 and lens 3, and was aimed at a spot at the centre of mirror 2. The pump-laser beam was made incident on the same spot by adjusting mirror 1 and lenses 1 & 2. Mirror 2 was then used to steer the pump-laser beam through the fluorescence cell and make it overlap the probe-laser beam. The alignment of the two laser beams was considered satisfactory when both beams coincided at the centres of the three mirrors. The blue fluorescence emission, excited with the pump-laser, was focused with lens 4 on the entrance slit of

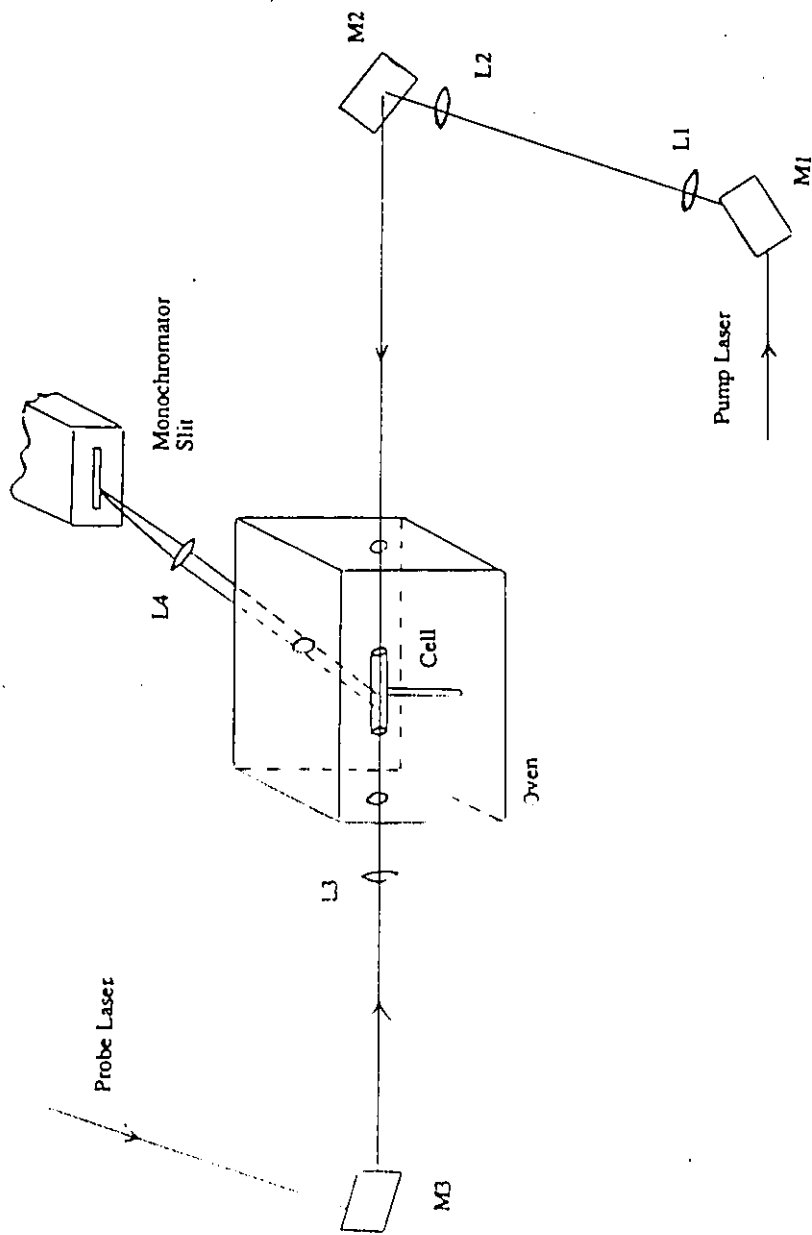


Figure 3.5 Schematic diagram for the arrangement of mirrors and lenses used to achieve an optimum overlap between the pump and the probe beams. L1, L2, L3 and L4 are quartz lenses. M1, M2 and M3 are aluminum mirrors.

the monochromator. The final alignment was achieved by minute adjustments of mirror 2 and lens 4 while monitoring the digitized signal displayed on an oscilloscope.

The pump-and-probe experiments consisted of two separate but complementary parts :

3.2.4.1 Monochromator Scans of the Fluorescence Spectra

The probe laser was tuned to excite transitions between particular vibrational levels of a low-lying excimer state and a higher state. Numerous fluorescence bands arising from bound-continuum and bound-bound decays were recorded by scanning the monochromator in increments of 1, 2 or 3 Å, using narrow slits ($\leq 1/8$ mm), and the boxcar time-averaging method. The probe-laser pulses, which also triggered the transient digitizer, were delayed by 450 ns relative to the pump pulses. The delay corresponded to the maximal population of the reservoir states. This was verified experimentally by scanning the time delay between the pump and probe pulses while monitoring the intensity of the fluorescence induced by the probe pulses in relation to the delay.

When monitoring the spectrum arising from bound-bound transitions, the vibrational component which was of the same wavelength as the probe laser radiation was not recorded.

When deemed appropriate, this component was recorded by tuning the excitation (probe) wavelength to a different vibrational transition between the same electronic states and recording the resulting fluorescence spectrum.

The time-evolution of the fluorescence was also monitored to obtain estimates of the lifetimes of the upper states. When the UV bound-continuum fluorescence was recorded, the initial 20 channels (2 ns each) of the transient digitizer were used. When the visible fluorescence in the blue spectral region was recorded, only 13 of the channels were used together with the HR-320 monochromator to reject as much as possible of the intense and persistent background fluorescence excited by the pump pulses.

3.2.4.2 Probe-Laser Scans of the Excitation Spectra

To record an excitation spectrum, the monochromator was set on a wavelength corresponding to a vibrational component of a fluorescence band arising from a level v' , while the probe laser was scanned over the spectral region containing components corresponding to the excitation of level v' from various v'' levels of a lower-lying electronic state. A box-car time-averaging method was again used for data acquisition.

LEAF 48 OMITTED IN PAGE NUMBERING

A power curve was recorded for each laser dye to permit the normalization of intensities of the components in the excitation spectrum. This was done by setting the monochromator at the zero-order position, and scanning the dye laser under the same experimental conditions as before except that the pump laser was turned off.

Since the degree of resolution in the excitation spectra did not depend on the resolution of the monochromator, 1 mm slits were used while recording the spectra by monitoring the UV fluorescence. This increased the intensity of the fluorescence reaching the photomultiplier and resulted in a higher signal-to-noise ratio. As noted previously, when the fluorescence was monitored in the blue region of the spectrum, the excitation spectra were recorded by using narrower slits ($< 1/8$ mm) in order to reduce to a minimum the stray light due to the intense 'background' fluorescence (4750 Å). The probe-laser scanning increment was 1 or 2 Å and the number of channels used in the transient digitizer ranged from 11 to 20 (2 ns each), depending on the effective lifetimes of the emitting states, the spectral region of the fluorescence and the resolution of the monochromator.

The linearity of the scanning steps of the stepper-motor-activated sine-drive with the wavelength increments was found to be very precise across the 5850 - 6500 Å region which was covered by two laser dyes: Rhodamine 610 and Rhodamine 640 (20.00 steps/Å and 16.00 steps/Å, respectively).

This was checked by comparing the counter readings of the wavelength drive with the optogalvanic spectrum of Ne produced in a miniature glow lamp. Figure 3.6 shows a schematic diagram describing the method used for the calibration. The dye-laser output was split into two parts, of which one was focused into an optogalvanic Ne cell, and the other was made incident on a photodiode which triggered the oscilloscope. When the dye laser was scanned, voltage changes at the discharge electrodes, due to the variation in the net degree of ionization of neon, were detected on the oscilloscope whenever the dye laser output corresponded to the components of the optogalvanic Ne spectrum³³. A calibration curve representing a plot of stepper-motor readings against actual wavelengths was then obtained and the linearity was verified. For the other laser dyes, which cover spectral regions in which there is no optogalvanic Ne spectrum, the calibration curves were produced by comparing the wavelengths of the dye laser output at different counter readings with the Fizeau wavemeter³⁰. The results showed that for the Rhodamine 6G, Coumarin 540 and Coumarin 500 dyes, the linearity was exact (20.00 steps/ Å) as long as the range was restricted to the generation band of each individual dye. For the Coumarin 460, Coumarin 440, Stilbene 420 and DPS dyes, which were used with the diffraction

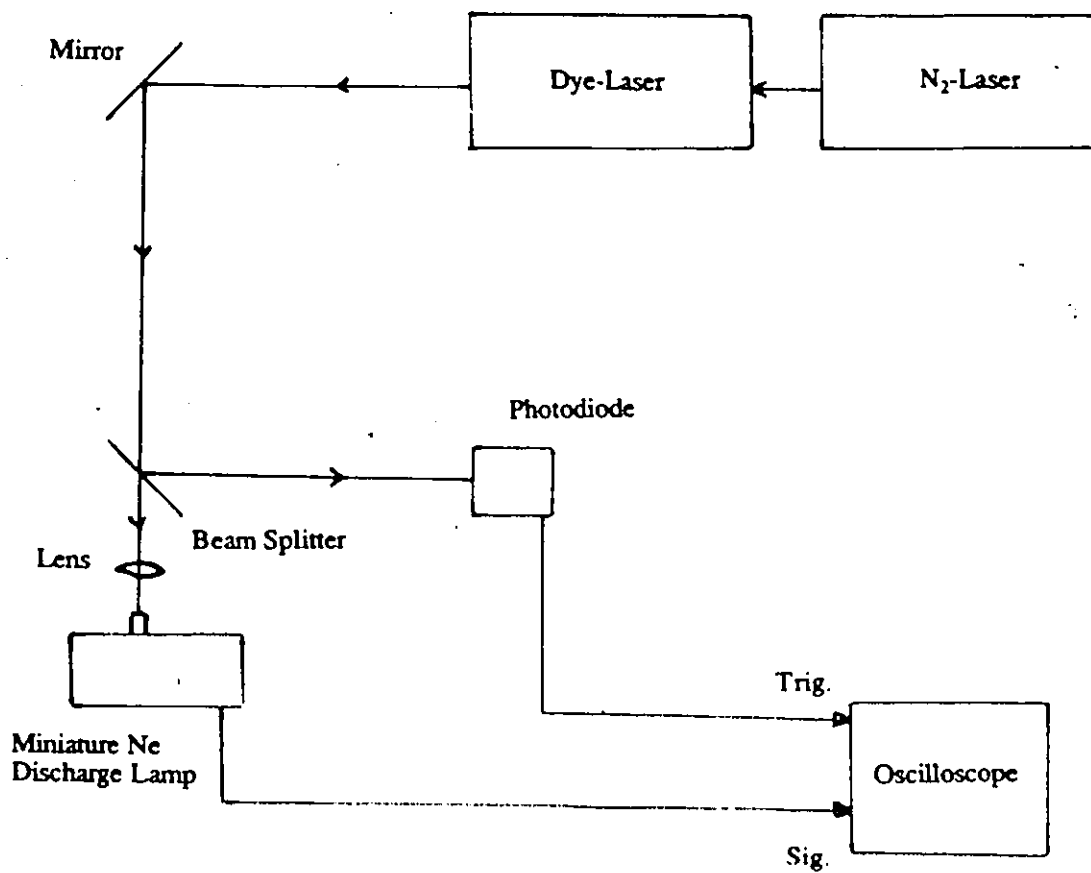


Figure 3.6 Schematic diagram of the apparatus used to calibrate the probe laser wavelength drive.

grating in a higher order, the wavelength increments corresponded to non-integral numbers of steps (23.98 steps/Å) over a range of 100 Å.

4 RESULTS AND DISCUSSION

4.1 The 4750 Å Fluorescence Band

Figure 4.1 shows the spectral profile of the 4750 Å fluorescence band excited with the pump laser³⁴. This band was first recorded, using photographic techniques, by Eden¹ who determined the centre of the band at 4600 Å. My measurement, which is in accord with another recent observation³⁵, places the centre of the band near 4750 Å and shows it to possess a degree of asymmetry with respect to the central peak. At 5400 Å the fluorescence intensity decreased to 1/3 of the peak intensity and at longer wavelengths the band exhibited a weak but extended tail, not shown in Fig. 4.1; towards shorter wavelengths, the band intensity declined steeply. I believe that this band arises from the decay, to the XO^+ ground state, of the $A0^+$ and $A1$ states which are in thermal equilibrium with the metastable $A0^-$ state.

The time evolution of the band is shown in Fig 4.2 which also shows the Zn atomic fluorescence emitted in the $4^3P_1 \rightarrow 4^1S_0$ decay. The intensity-variation of the fluorescence band was typical for a three-body collision process, it increased rapidly following the pump pulse and then decayed exponentially with a decay time of about 6 μ s, in agreement

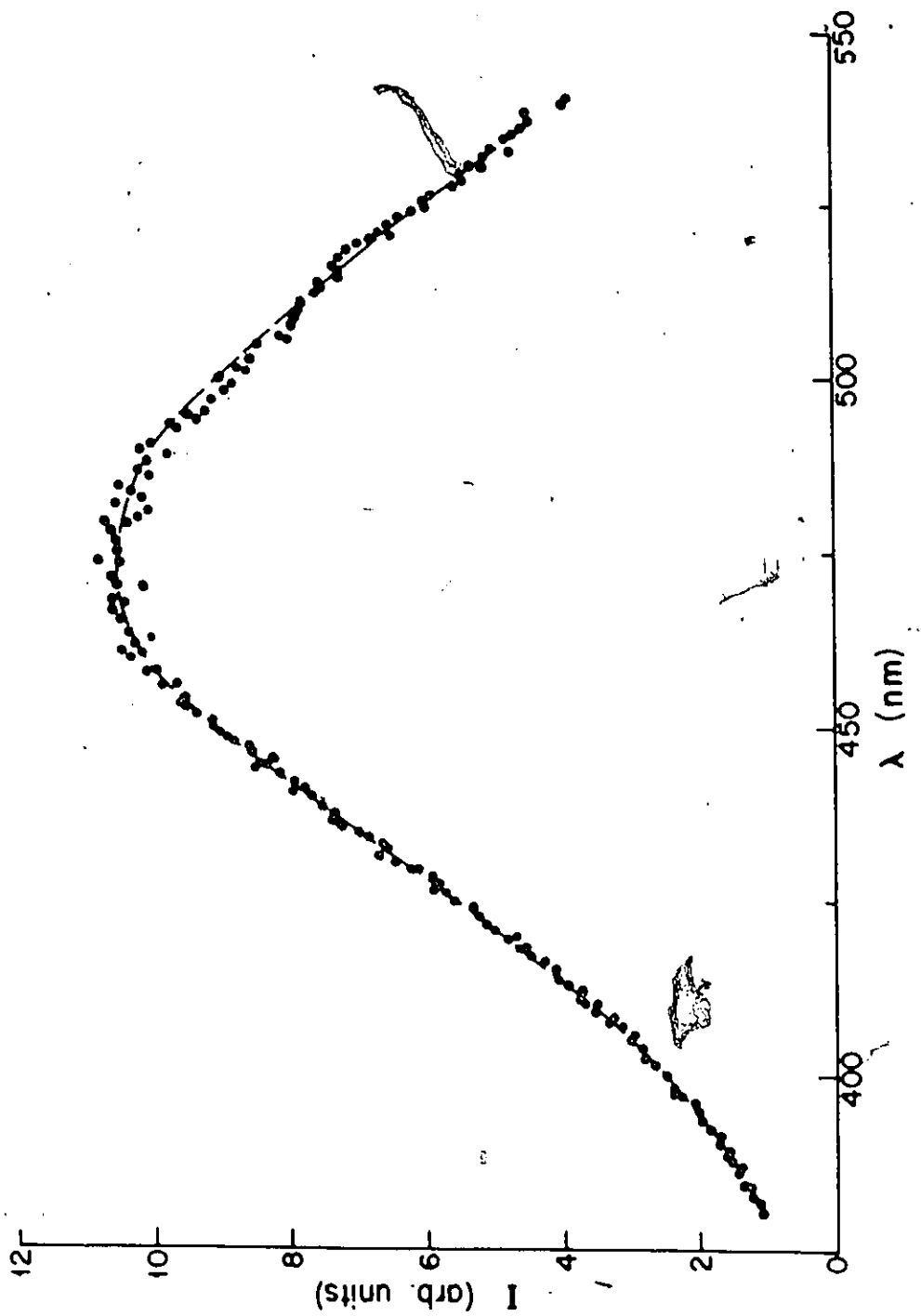


Figure 4.1 The profile of the fluorescence band excited with 3075.9 Å laser radiation.

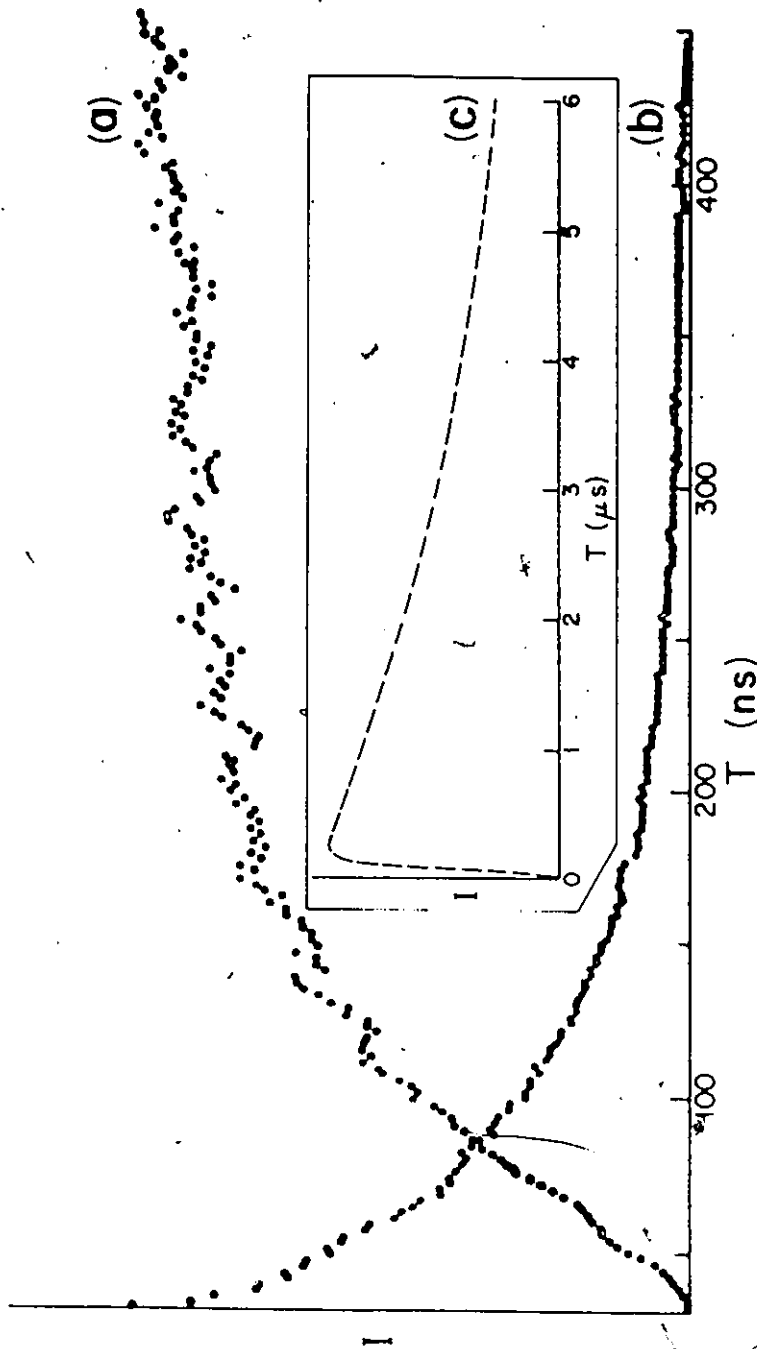


Figure 4.2 Time-evolution of the 4750 Å fluorescence band (a), coincident with the decay of the atomic Zn fluorescence (b). The inset (c) shows excitation and decay of the HgZn band over an extended time span.

with the observation of Eden¹ who, however, did not comment on the fast rise-time. Since the amount of Hg inside the cell was so arranged that, above 660 K, all of it was in the vapour phase, the Hg density increased with temperature until 660 K and then remained constant. The rise-time of the band was found to follow the same relation; it increased with the side-arm temperature up to 660 K and then remained constant. This suggested that, since no more Hg atoms were produced above 660 K while the density of the Zn atoms still increased with temperature, the HgZn molecule was formed by a three-body collision process which involved one Zn and two Hg atoms. The dependence of the rate of formation on the side-arm temperature below 660 K is illustrated in Fig. 4.3, which shows a comparison between the rise times at 470 K and at 570 K. At 470 K the densities of Hg and Zn in the cell were estimated to be 2×10^{17} and 4×10^{10} atoms/cm³, respectively, while at 570 K they were 3×10^{18} and 1.4×10^{13} atoms/cm³, respectively. It can be seen in Fig. 4.3 that at 570 K the rate of formation of HgZn was higher than at 470 K.

The decay time of the Zn fluorescence was found to be of the same order as the rise time of the HgZn fluorescence at various temperatures of the side-arm, which also confirms that the formation of the excimer required a three-body-collision involving one Zn and two Hg atoms.

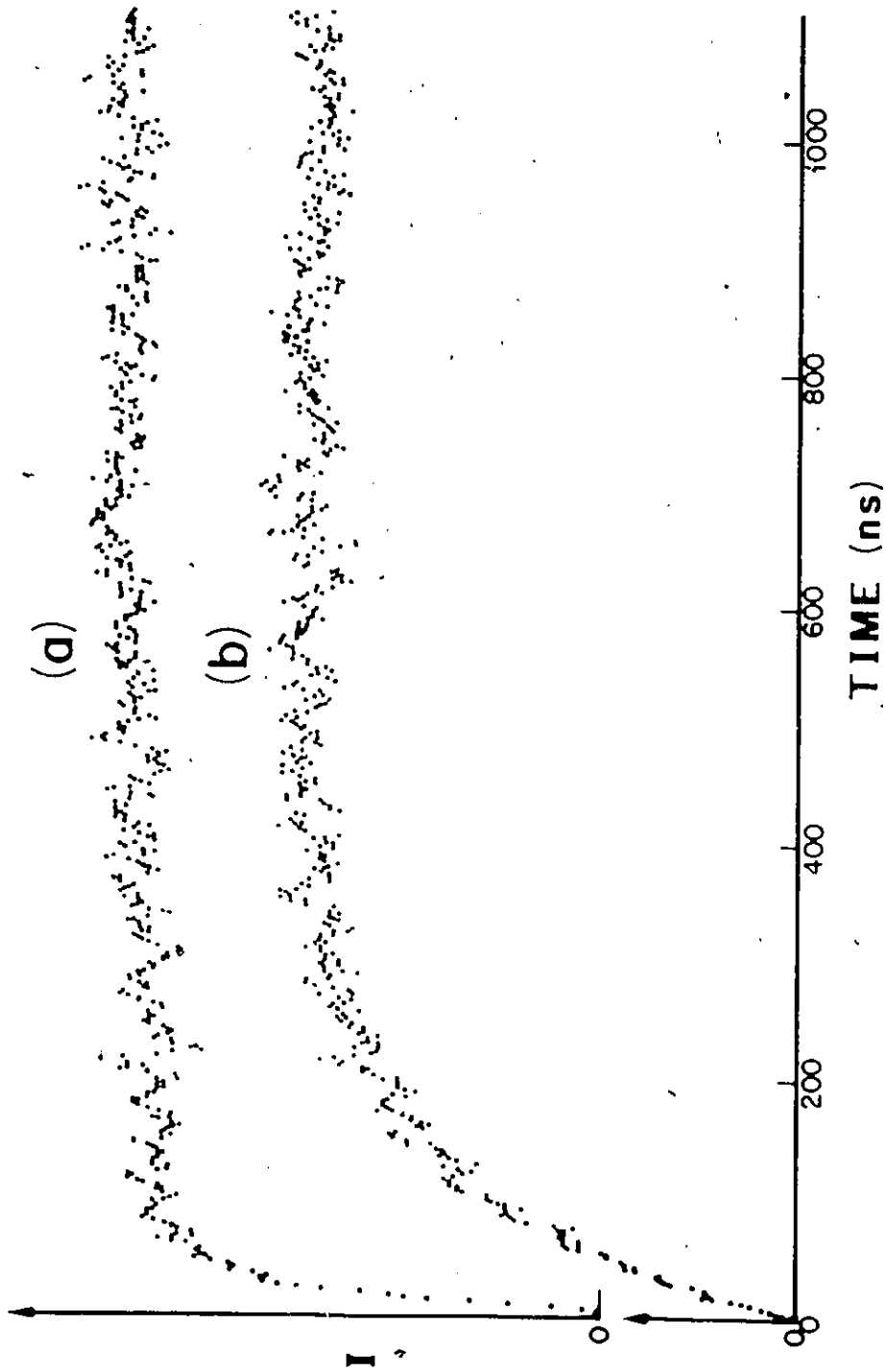
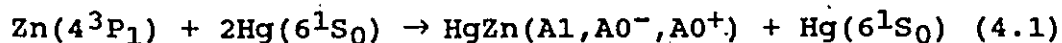


Figure 4.3 Time-evolution of the 4750 Å fluorescence band at the side-arm temperatures 570 K (a) and 470 K (b). The temperature of the main oven was held at 770 K.



This mechanism was put forward by Eden¹ who, however, did not specify the excited states of HgZn.

4.2 Excitation and Decay of the C0⁺ State

When the HgZn excimer was irradiated with a probe pulse in the 5200 - 6650 Å region, UV fluorescence bands were detected in the 2380 - 2650 Å region^{20,36}. The fluorescence bands had the form of CID patterns characteristic of bound-continuum transitions, but were obliterated at wavelengths near and above 2537 Å because of absorption of radiation in the region of the broadened Hg 2537 Å ($6^3\text{P}_1 \leftarrow 4^1\text{S}_0$) line. The excitation spectrum in the 5200 - 6650 Å region, recorded by monitoring the fluorescence at the various CID peaks, exhibited an extensive structure typical of bound-bound transitions.

I believe that this fluorescence was due to a decay of the C0⁺ state, excited by transitions from the A0⁺ reservoir state, to the X0⁺ ground state. A partial PE diagram for the X0⁺, A0⁺ and C0⁺ states is shown in Fig. 4.4²⁵. It, like the assignment of the spectrum, supersedes the previous interpretation based on Hund's case (a) PE curves²⁰

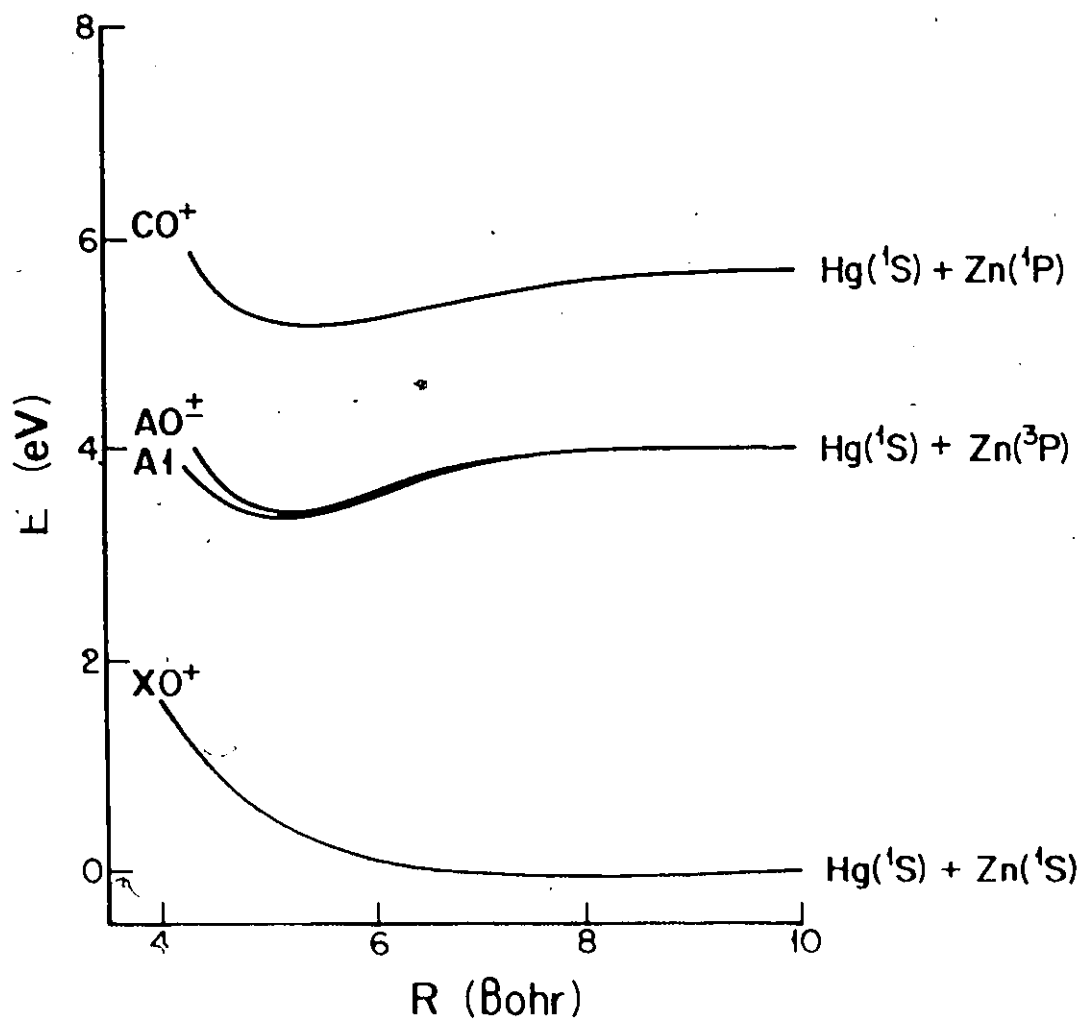


Figure 4.4 A partial PE diagram showing the XO^+ , A1 , AO^- , AO^+ and CO^+ states.

4.2.1 The Fluorescence Spectrum in the 2380 - 2650 Å Region

Figure 4.5 shows traces of fluorescence bands emitted in the decay of the $v' = 6, 7, 8$ and 9 vibrational levels of the $C0^+$ state to the repulsive $X0^+$ ground state. As stated above, the bands have the form of CID patterns characteristic of bound-continuum transitions, with two prominent peaks on the wings of each band, corresponding to the classical turning points of the particular v' wave functions. The $v' = 6$ band shown in Fig. 4.5 (a) was excited using the probe laser wavelength $\lambda = 5660$ Å which corresponds to the $C0^+, v' = 6 \leftarrow A0^+, v'' = 0$ absorption. The excitation of the $v' > 6$ levels from $v'' = 0$ was accomplished with shorter probe wavelengths, corresponding to an excitation energy increment of about 117.5 cm^{-1} per vibrational quantum number v' , equivalent to the vibrational frequency ω_e of the $C0^+$ state. Although the band profiles are distorted by the (broadened) atomic Hg absorption at 2537 Å, it is nevertheless possible to make unambiguous assignments of v' levels from which they arise, making also use of the excitation spectra which are discussed below. A few additional small peaks may be seen on the short- λ wings of the bands (a) and (d), suggesting that two or more vibrational levels were excited simultaneously by the probe-laser radiation. The 2537 Å absorption made it impossible to detect any similar effect on the long- λ wings of the bands.

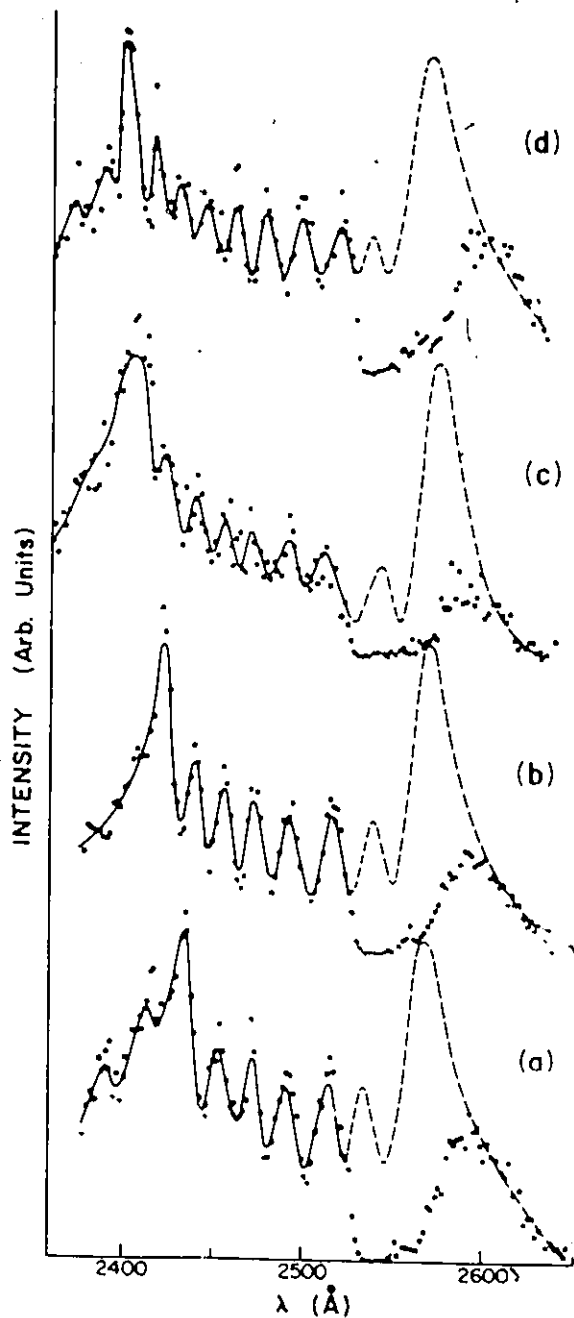


Figure 4.5 LIF bands emitted from selectively populated v' levels of the CO^+ state. (a) $v' = 6$, (b) $v' = 7$, (c) $v' = 8$, (d) $v' = 9$. The wavelengths of the probe radiation were (a) 5660 Å, (b) 5623 Å, (c) 5586 Å, (d) 5550 Å. The traces suggest the spectral profiles, the dashed lines indicate the probable positions of the components absorbed by Hg.

The relative intensities of the fluorescence bands excited in a $v' \leftarrow v'' = 0$ progression depend mainly on the FC factors. I found the intensity of the $v' = 7$ band to be the highest, decreasing towards both higher and lower v' values. This effect I attribute to the fact that the bond-lengths r_e differ in the upper and lower electronic states and, consequently, $v' \leftarrow v''$ transitions such as $0 \leftarrow 0$ and $1 \leftarrow 0$ are much weaker (in absorption) than other transitions taking place at approximately the same wavelengths, and are effectively masked. It is, however, possible to populate low v' states by excitation from $v'' > 0$ states, using the appropriate wavelengths of probe radiation and taking advantage of favorable FC factors; the intensity profile of the excitation spectrum usually provides a clear indication of the relative strengths of the $v' \leftarrow v''$ transitions. Figure 4.6 shows profiles of uv fluorescence bands excited by probe wavelengths in the range 5780 - 6080 Å. The bands are due to the $C0^+ \rightarrow X0^+$ decays of $v' = 0, 1, 2, 3, 4$ levels which were excited from various v'' ($A0^+$) states. As in Fig. 4.5, profiles of the CID bands are distorted by the strong atomic absorption near 2537 Å. Nevertheless, the v' and v'' assignments are quite unambiguous and fully consistent with the many recorded CID bands and with the excitation spectrum, as will be seen in the subsequent section.

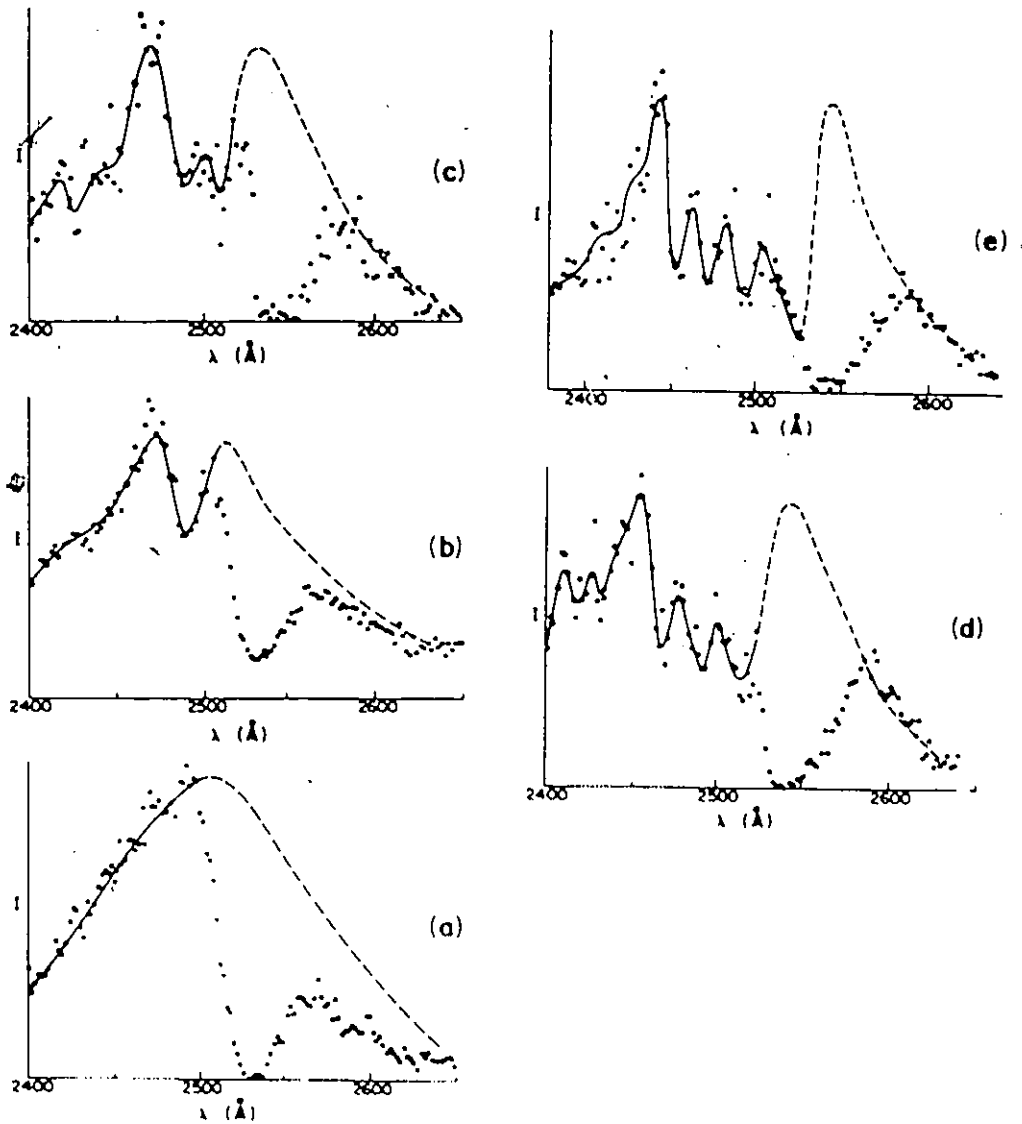


Figure 4.6 LIF bands emitted from v' levels of the CO^+ state. (a) $v' = 0$, (b) $v' = 1$, (c) $v' = 2$, (d) $v' = 3$, (e) $v' = 4$. The wavelengths of the exciting probe radiation and the corresponding $v' \leftarrow v''$ transitions are (a) 6078 \AA , $0 \leftarrow 3$; (b) 6035 \AA , $1 \leftarrow 3$; (c) 5922 \AA , $2 \leftarrow 2$; (d) 5818 \AA , $3 \leftarrow 1$; (e) 5781 \AA , $4 \leftarrow 1$. The dashed lines indicate the positions of the component absorbed by Hg.

4.2.2 The Excitation Spectrum in the Region 5200 - 6650 Å

Scanning the probe laser over the wavelength range 5200 - 6650 Å, while recording the fluorescence with the monochromator at fixed wavelength settings, produced an extensive and highly structured excitation spectrum which is shown in Fig. 4.7 (a, b, c and d) and which represents the vibrational structure of the $\text{CO}^+ \leftarrow \text{AO}^+$ excitation band system. I found the decay time of the upper state (CO^+) to be of the order of 1 ns as its decay appeared to follow the time-evolution of the probe laser pulse. It is not certain whether the decay time, which is of the same order as that of the 4^1P Zn state, represents the radiative lifetime of the CO^+ state or whether it represents the effective lifetime which would include non-radiative decay (quenching). Although the decay time was found invariant over a range of temperatures and vapor densities, the time-resolution of the apparatus was not sufficient to rule out the presence of quenching. Each part of Fig. 4.7 shows a segment of the excitation spectrum recorded with a particular probe-laser dye and with the monochromator setting at a wavelength corresponding to a peak in the fluorescence spectrum described in Section 4.2.1. The extensive structure is, in each case, superimposed on a continuous background which contains up to 60% of the total intensity. Although in some segments the

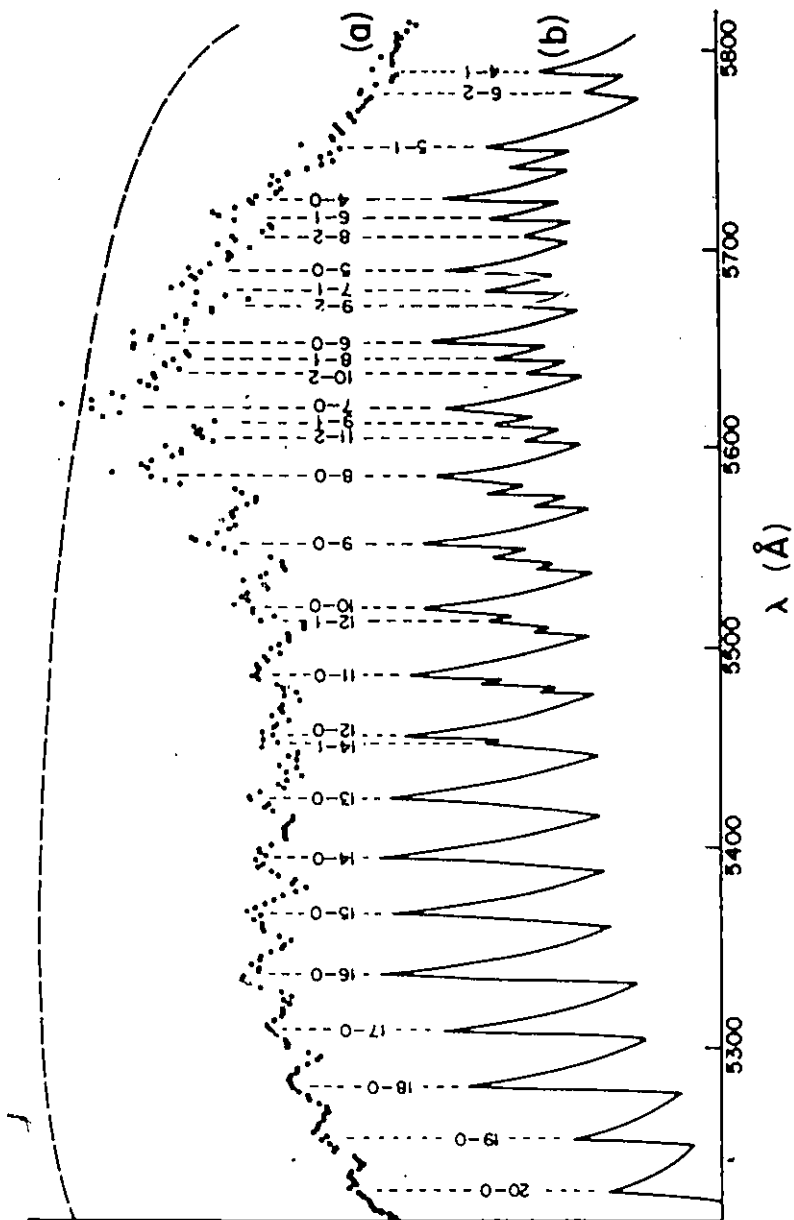


Figure 4.7 (a) Traces of the fluorescence-monitored $\text{CO}^+ \leftarrow \text{A}0^+$ excitation band system, showing $v' \leftarrow v''$ assignments in the 5200-5750 Å region. The dots represent the experimental trace and the solid line is the computer-modeled spectrum; the dashed curves indicate relative dye-laser power.

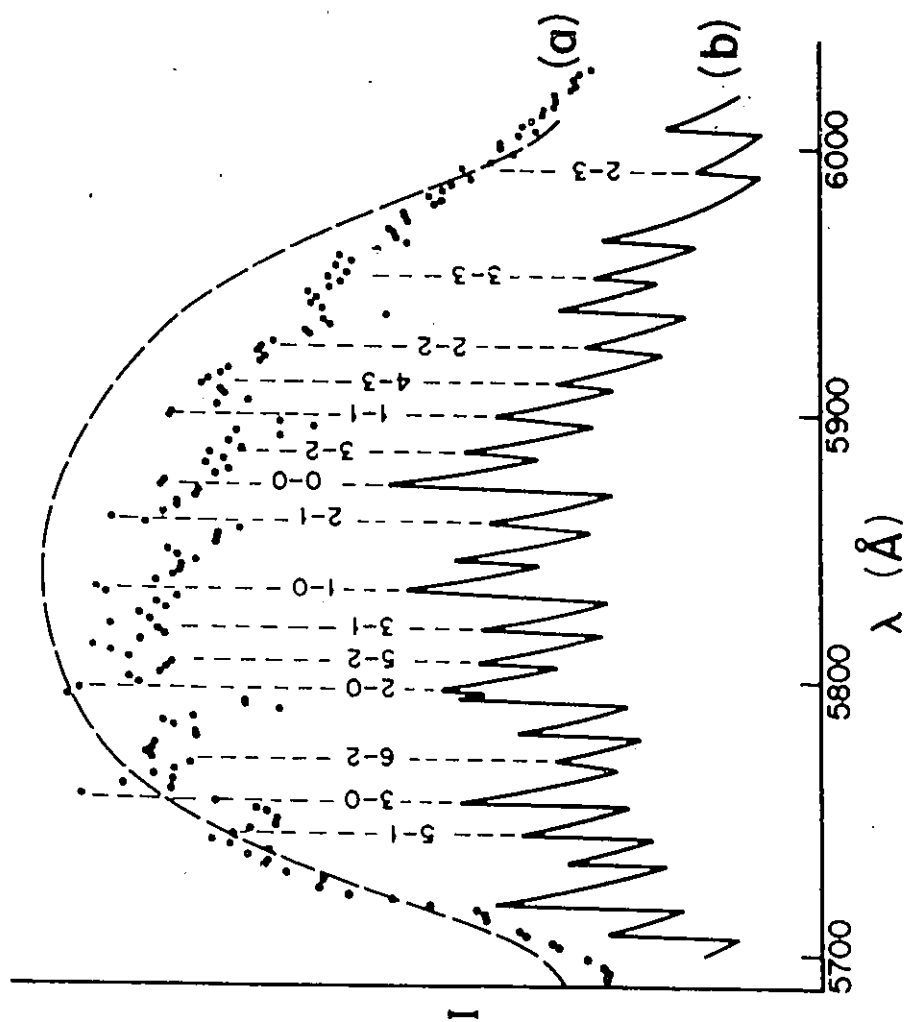


Figure 4.7 (b) Traces of the fluorescence-monitored $\text{CO}^+ \leftarrow \text{AO}^+$ excitation band system, showing $v' \leftarrow v''$ assignments in the 5700-6000 \AA region.

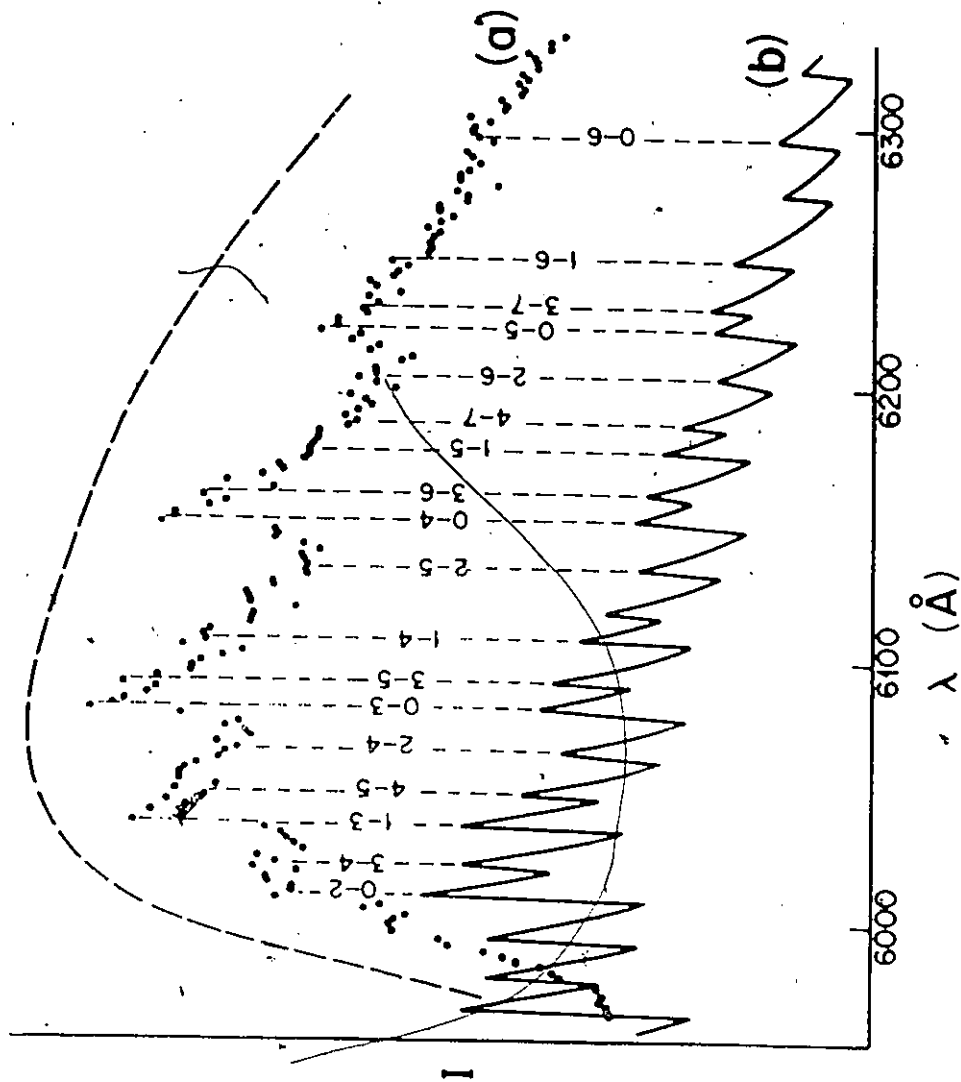


Figure 4.7 (c) Traces of the fluorescence-monitored $\text{CO}^+ \leftarrow \text{A0}^+$ excitation band system, showing $v' \leftarrow v''$ assignments in the 6000-6300 Å region.

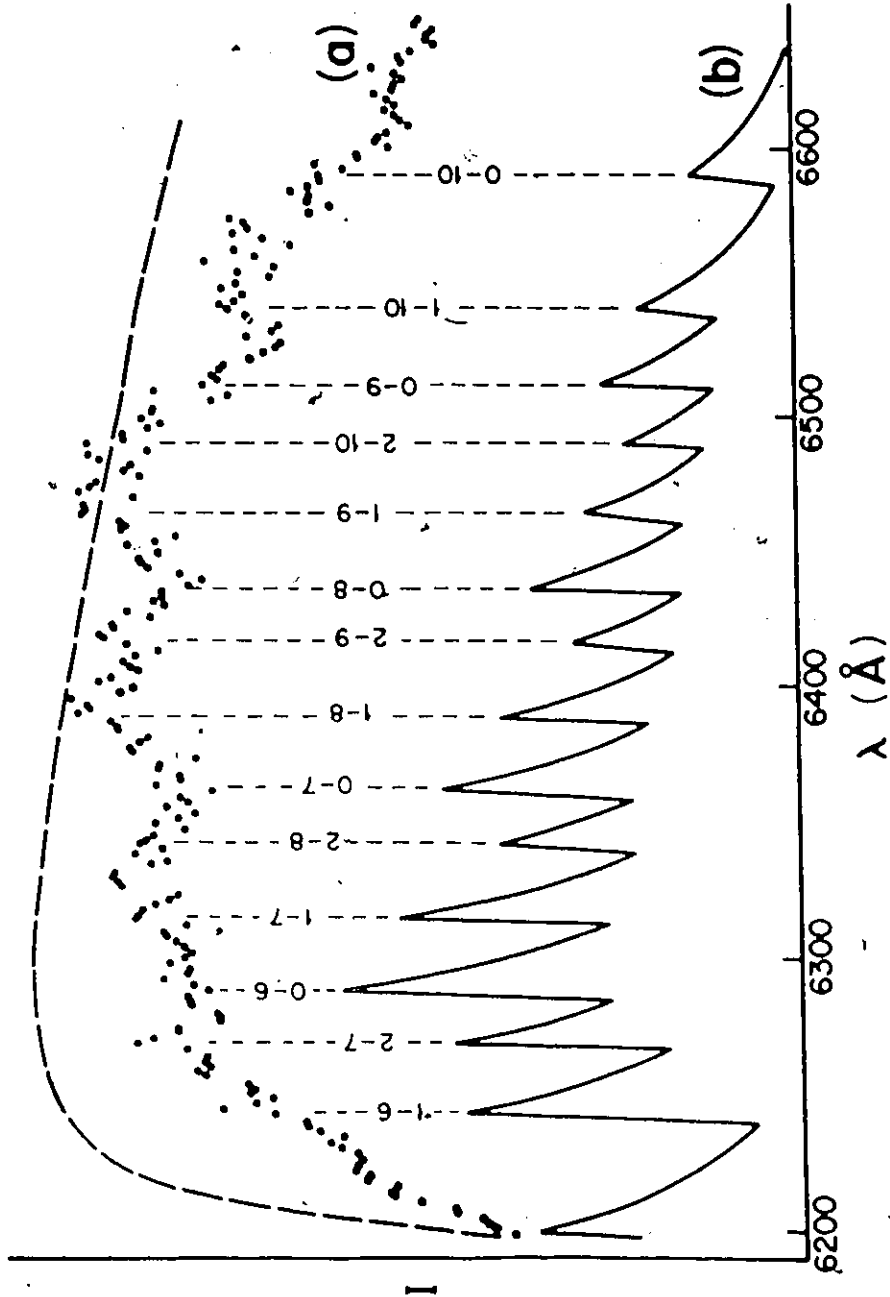


Figure 4.7 (d) Tracés of the fluorescence monitored $\text{CO}^+ \leftarrow \text{A0}^+$ excitation band system, showing $v' \leftarrow v''$ assignments in the 6250-6600 Å region.

background accounts for even a higher proportion of the intensity, I found the structure to be fully reproducible during the many scans of the spectrum.

Figure 4.7 (a) shows the excitation spectrum in the 5200 - 5750 Å region, recorded with the monochromator set at 2420 Å. The structure represents a v' progression with $v'' = 0$, and the assignment of the individual vibrational components has been verified by direct comparison with the CID fluorescence spectra. The most intense component arises from the $v' = 7 \leftarrow v'' = 0$ transition produced by a probe wavelength of 5623 Å. That some of the peaks in this spectrum do not show sharp leading edges suggests that they may be due to several transitions with nearly equal energies (e.g., $0 \leftarrow 0$, $1 \leftarrow 1$, $2 \leftarrow 2$, etc.), which could be induced by a single probe wavelength and could take place with different transition moments, depending on the FC factors. The highest Δv transition, which was identified in the $v' \leftarrow v'' = 0$ progression, corresponds to $v' = 23 \leftarrow v'' = 0$, located near 5160 Å. Shorter probe wavelengths gave rise to an unstructured continuum as shown in Fig. 4.8.

Figure 4.7 (b) shows the excitation spectrum in the range 5700 - 6000 Å recorded with the monochromator at 2435 Å. The spectrum, although quite intense, possesses a rather irregular structure suggesting that the FC factors favor no particular v' or v'' progression, even though it seems that they influence the profile of the spectrum to a greater

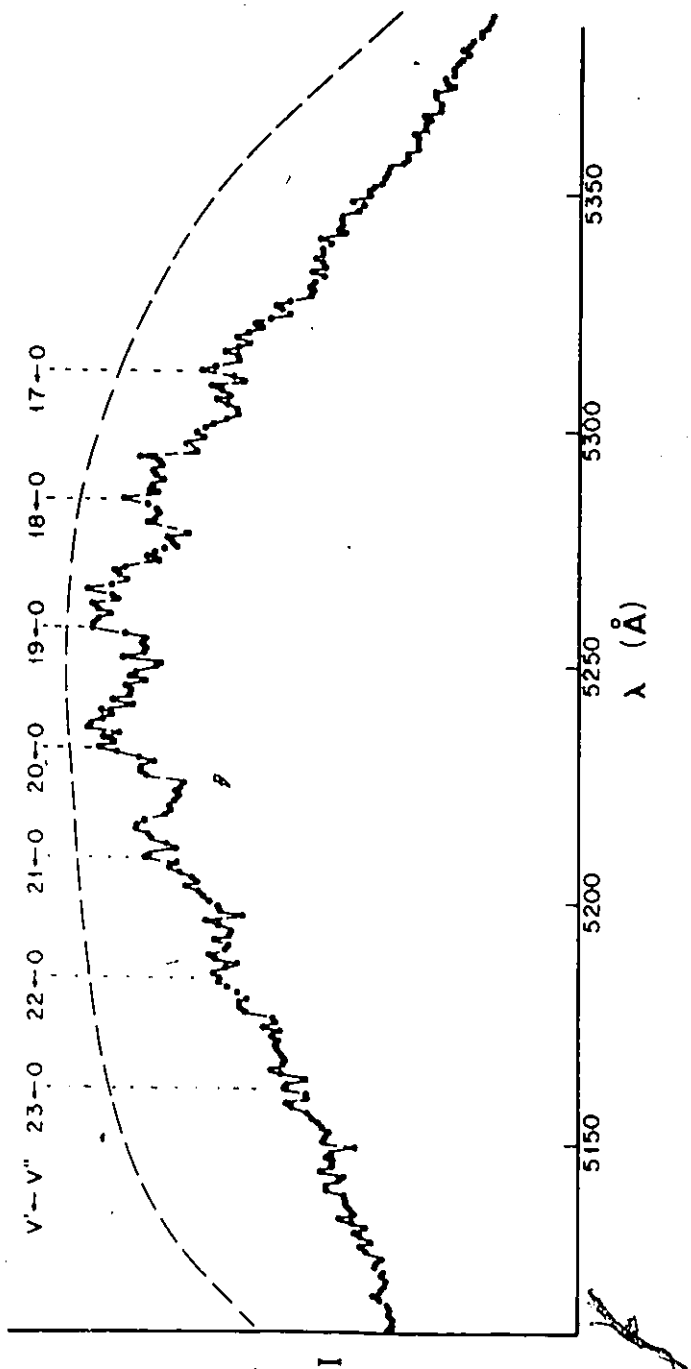


Figure 4.8 Traces of the fluorescence-monitored $\text{CO}^+ \leftarrow \text{A}0^+$ excitation band system, showing some $v' \leftarrow v''$ assignments in the 5100-5350 Å region. The structure merges into a continuum below 5200 Å.

extent than the Boltzmann vibrational distribution. This situation resembles that encountered in the intermediate region of the $GO_u^+ \leftarrow AO_g^+$ excitation spectrum of Hg_{18} . The $v' = 0 \leftarrow v'' = 0$ transition would be expected to lie at $5872 \pm 4 \text{ \AA}$ and appears to be of considerably lower intensity than other close-lying transitions. The most intense fluorescence was produced by probe-laser scans in the 5500 - 5850 \AA range, which induced transitions from various low-lying v'' states to higher v' states. This observation, together with the fact that the vibrational components are degraded towards long wavelengths, suggests that the PE minimum of the CO^+ state is located at a larger internuclear separation than the minimum of the AO^+ state, as was already indicated by the preliminary calculations.

As the probe laser was scanned towards longer wavelengths, the excitation spectrum again assumed a more regular structure which extended from 6000 \AA to 6300 \AA and may be seen in Fig. 4.7 (c). Here the spectrum was monitored at 2450 \AA and the structure represents a v'' progression of transitions terminating at the $v' = 0$ state, as was confirmed by the examination of the CID fluorescence bands excited with the various probe wavelengths (see Fig. 4.7 (a)). Figure 4.7 (d) shows the next segment of the excitation spectrum (6250 - 6600 \AA) monitored at 2500 \AA where the various peaks are due to transitions from weakly populated high v'' states to low v' states. The decreasing intensity

at longer wavelengths³ in this part of the spectrum is mainly attributed to the Boltzmann vibrational distribution. The sequence of peaks resembles that observed in the 6200 - 6500 Å region of the $GO_u^+ \leftarrow AO_g^+$ excitation spectrum of Hg_2^{19} , except that in the present case the vibrational components do not exhibit sharp leading edges, which limits the accuracy of the vibrational analysis. As the vapor mixture was probed with wavelengths longer than 6700 Å, the fluorescence signal faded rapidly.

The vibrational analysis of the spectrum shown in Fig. 4.7 was carried out by substituting the measured wavelengths of the various identified peaks in the standard term equation (2.22). Preliminary values of ω_e' and ω_e'' were first determined by a least-squares analysis of the v' and v'' progressions. More accurate values of ω_e and $\omega_e x_e$ were yielded from the direct comparison of the observed spectrum with a computer-simulated spectrum. The modeling procedure took into account the Boltzmann population distribution of the vibrational states but not the unknown FC factors. The vibrational constants $\omega_e'' = 194 \pm 4 \text{ cm}^{-1}$, $\omega_e'' x_e'' = 0.7 \pm 0.2 \text{ cm}^{-1}$, $\omega_e' = 117 \pm 4 \text{ cm}^{-1}$ and $\omega_e' x_e' = 0.5 \pm 0.2 \text{ cm}^{-1}$ were adjusted to produce the best fit between the observed and modelled spectra shown in Fig. 4.7. The difference between the internuclear separations at the potential minima (Δr_e)

of the $C0^+$ and $A0^+$ states were estimated to be 0.25 ± 0.01 Å, using a computer-simulated modelling which computes the integral (2.33), (see Appendix).

4.3 Excitation and Decay of the E1 and F1 States

When the HgZn excimers were probed with radiation of various wavelengths in the range 4200 - 4500 Å, an intense UV fluorescence spectrum was detected in the 2230 - 2320 Å region¹⁶. The spectrum consisted of overlapping CID patterns belonging to bound-continuum transitions from two excited electronic states to the ground state. They decayed simultaneously in the same spectral region following excitation with a single probe wavelength and there was some difficulty with the identification and analysis of the spectra. An additional complication arose from the presence of a third partially resolved bound-continuum fluorescence spectrum extending over the range 2300 - 2660 Å, whose overall profile was typical of a decay of a high vibrational level.

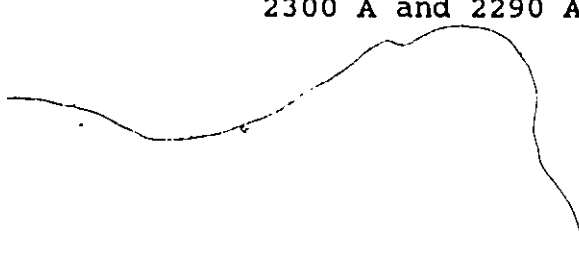
The corresponding excitation spectrum, when monitored in the UV, was found to consist of three band systems which overlapped and produced a complex structure. One of these band systems was also observed by monitoring the fluorescence at one of its vibrational components or at the Hg 4916 Å emission line. The other two band systems represented transitions from two lower states to one upper state, but no

bound-bound transitions involving the upper state were detected. On the basis of the comparison between the fluorescence and excitation spectra, and the PE diagram, I assigned the upper and lower states of the first band system as the $F1(Hg^1S + Zn5^3S)$ and $A0^+$ states, respectively, and the upper and the two lower states of the other two band systems as the $E1(Hg^1S + Zn^1P)$, $A0^-$ and $A0^+$ states. A partial PE diagram for the $X0^+$, $A1$, $A0^-$, $A0^+$, $E1$ and $F1$ states is sketched in Fig. 4.9.

4.3.1 The Fluorescence Spectrum in the 2230 - 2320 Å Region

4.3.1.1 The $E1 \rightarrow X0^+$ Fluorescence Spectrum

Traces of the fluorescence bands emitted in the bound-free $E1 \rightarrow X0^+$ decay of the $v' = 1$ and $v' = 0$ levels are shown in Fig. 4.10. Both levels were excited from the $v'' = 0$ level of the $A0^+$ state, using probe wavelengths of 4394 Å and 4421 Å, respectively. The CID patterns corresponding to these bands are partly overlaid by an additional CID pattern which has a smaller spacing between maxima, exhibits a prominent peak near 2340 Å, and extends to 2660 Å. This CID "background" has not yet been analyzed and its origin is to be further investigated. The prominent peaks near 2340 Å, 2300 Å and 2290 Å were found to be a constituent part of



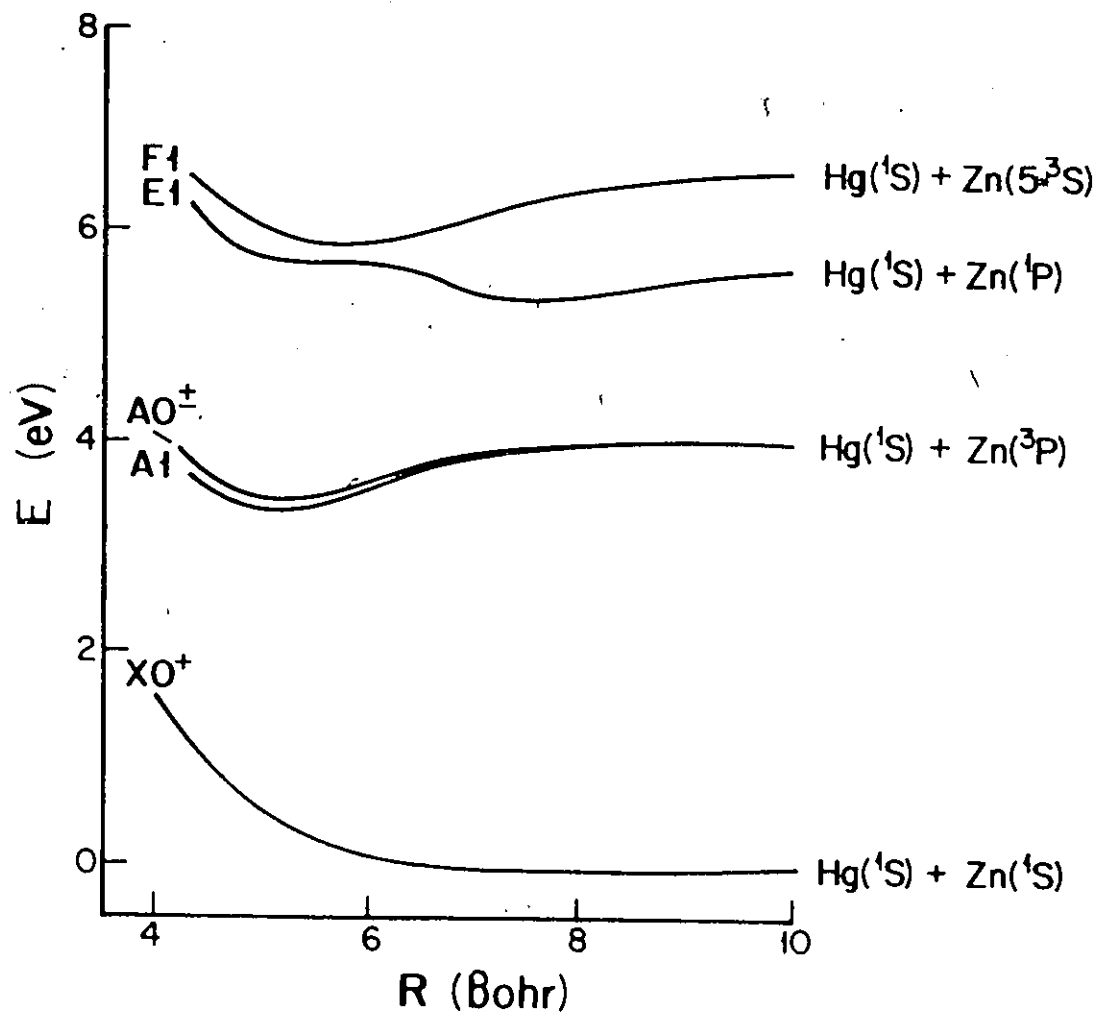


Figure 4.9 A partial PE diagram showing the XO^+ , $A1$, $A0^-$, $A0^+$, $E1$ and $F1$ states.

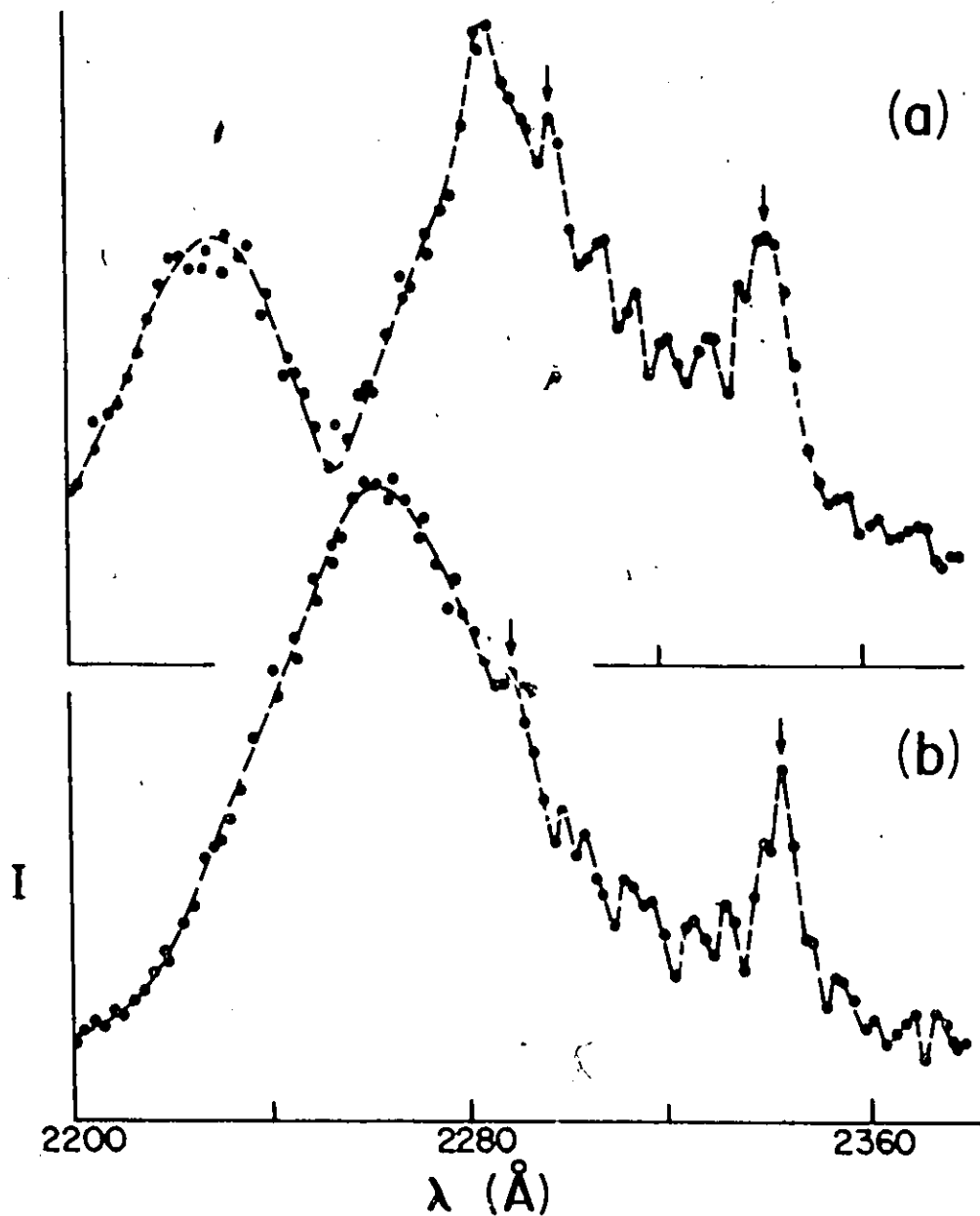


Figure 4.10 LIF bands emitted from (a) $v' = 1$ and (b) $v' = 0$ levels of the $E1$ state excited from the $A0^+$, $v'' = 0$ level with 4394 Å and 4421 Å probe radiation, respectively. The vertical arrows indicate peaks due to the 'background' fluorescence spectrum.

this spectrum.

Using probe wavelengths longer than 4421 Å, resulted in the excitation of the E1, $v' = 0$ level from $A0^+$, $v'' = 1, 2, 3$ and 4 levels, which were found to have an energy spacing of $194 \pm 5 \text{ cm}^{-1}$, in good agreement with the value obtained in section 4.2.2. Using probe wavelengths shorter than 4421 Å resulted in the excitation of the E1, $v' = 1, 2$ and 3 levels from the $A0^+$, $v'' = 0$ level. For these levels the energy spacing was approximately 135 cm^{-1} which corresponds to the vibrational frequency ω_e of the E1 state.

Figure 4.11 shows traces of the fluorescence bands emitted in the $E1 \rightarrow X0^+$ decays of the $v' = 1$ and $v' = 0$ states which, in this case, were excited from the $A0^+$, $v'' = 0$ level by 4347 Å and 4372 Å probe radiation, respectively. The spectra include the unidentified "background" peaks at 2340 Å and 2290 Å. The vibrational spacing in the $A0^+$ state was found to be $190 \pm 5 \text{ cm}^{-1}$.

4.3.1.2 The F1 \rightarrow X0⁺ Fluorescence Spectrum

Figure 4.12 shows traces of the fluorescence bands emitted in the $F1 \rightarrow X0^+$ decay of the $v' = 1$ and $v' = 0$ levels. Both v' levels were excited from the $A0^+$, $v'' = 0$ level using 4258 Å and 4288 Å probe radiation, respectively. The bands also include the background CID spectrum with the

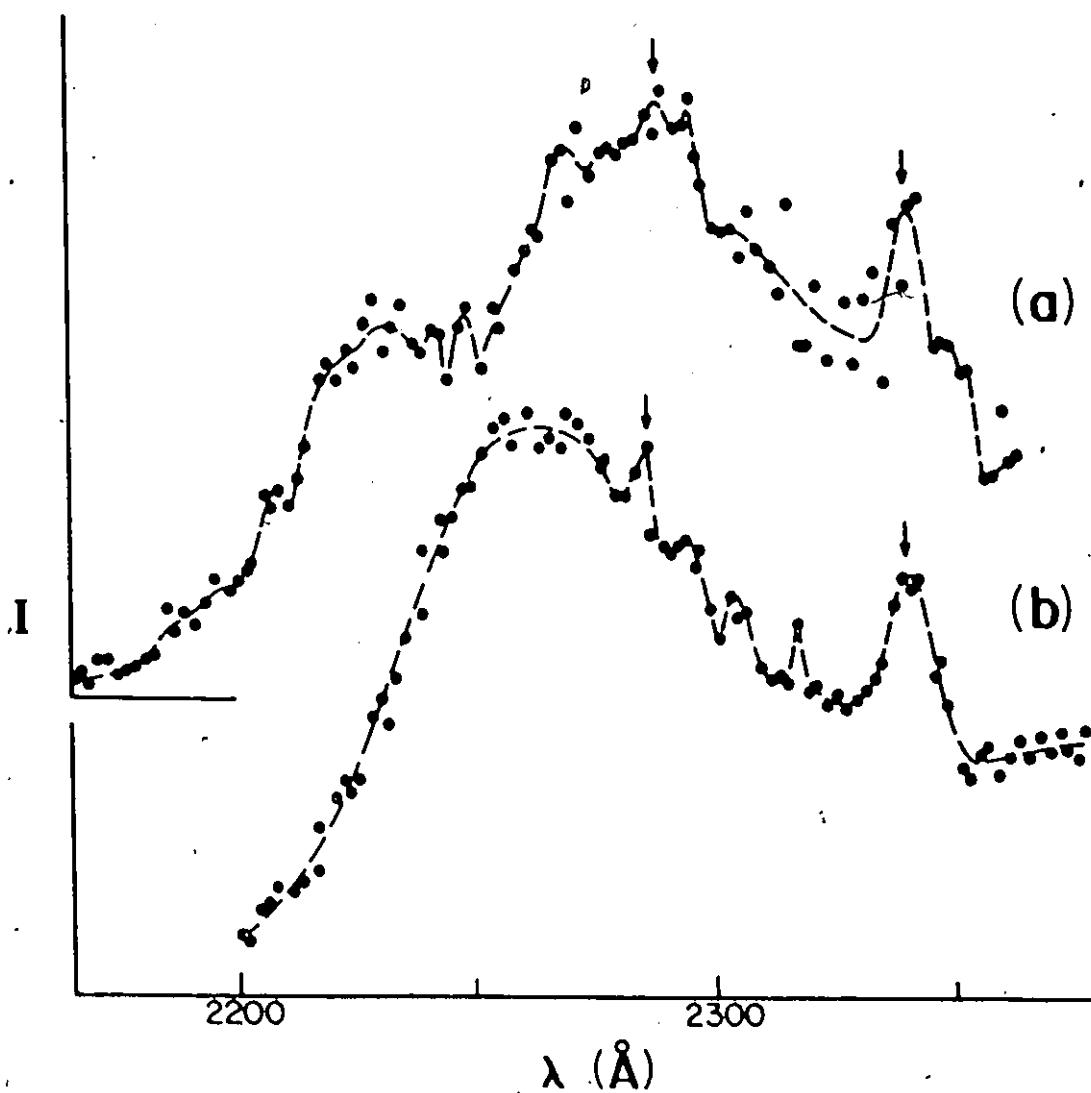


Figure 4.11 LIF bands emitted from (a) $v' = 1$ and (b) $v' = 0$ levels of the E_1 state excited from the $A_0^-, v'' = 0$ level with 4347 \AA and 4372 \AA probe radiation, respectively. The vertical arrows indicate peaks due to the 'background' fluorescence spectrum.

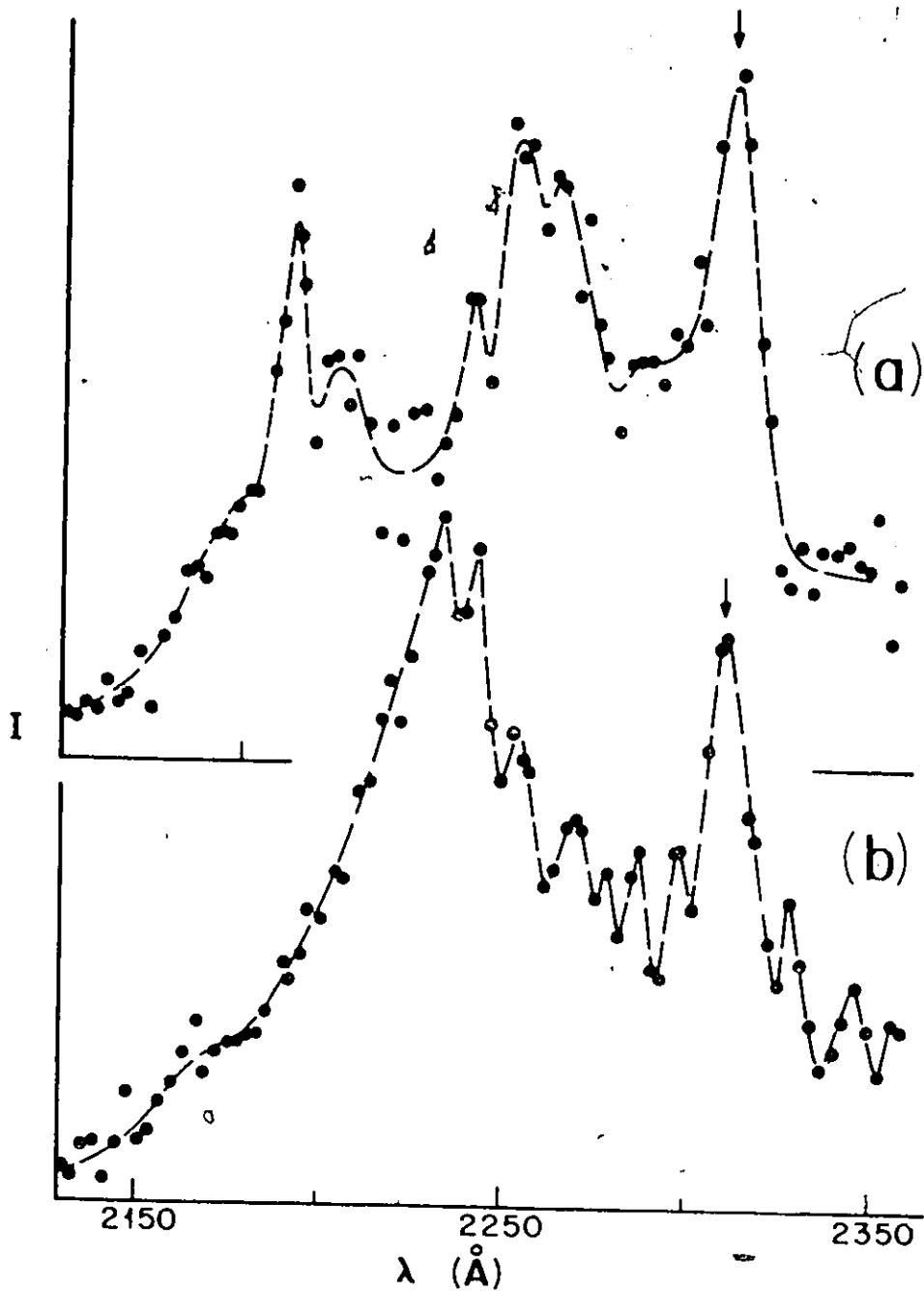


Figure 4.12 LIF bands emitted from (a) $v' = 1$ and (b) $v' = 0$ levels of the F1 state excited from the $A0^+$, $v'' = 0$ level with 4258 \AA and 4288 \AA probe radiation, respectively. The vertical arrows indicate peaks due to the 'background' fluorescence spectrum.

peak near 2340 Å quite prominent. It may be seen that the $v' = 0$ component of the F1 state is centred near 2230 Å, and of the E1 state near 2260 Å.

The effective lifetimes of the E1 and F1 states are estimated to be of the order of 1 ns as their decays appeared to follow the time evolution of the probe-laser pulse.

4.3.2 The Excitation Spectrum in the 4200 - 4500 Å Region

Figure 4.13 shows the extensive and highly structured excitation spectrum recorded by scanning the probe laser over the range 4200 - 4550 Å while monitoring the fluorescence at 2250 Å. It represents the vibrational structures of the $F1 \leftarrow A0^+$, $E1 \leftarrow A0^-$, and $E1 \leftarrow A0^+$ excitation bands which are identified in the trace. The $E1 \leftarrow A0^-$ and $E1 \leftarrow A0^+$, $v' = 0 \leftarrow v'' = 0$ transitions give rise to components at 4372 Å and 4421 Å, respectively, and thus yield the energy separation of $253 \pm 12 \text{ cm}^{-1}$ between the $A0^-$ and $A0^+$ reservoir states. The peak corresponding to the $F1 \leftarrow A0^+$, $(v' = 0 \leftarrow v'' = 0)$ transition is found at 4288 Å.

That all three bands include components arising from transitions between low v' and v'' levels leads to the conclusion that, in each case, the internuclear separations r_e in the upper and lower electronic states are nearly equal.

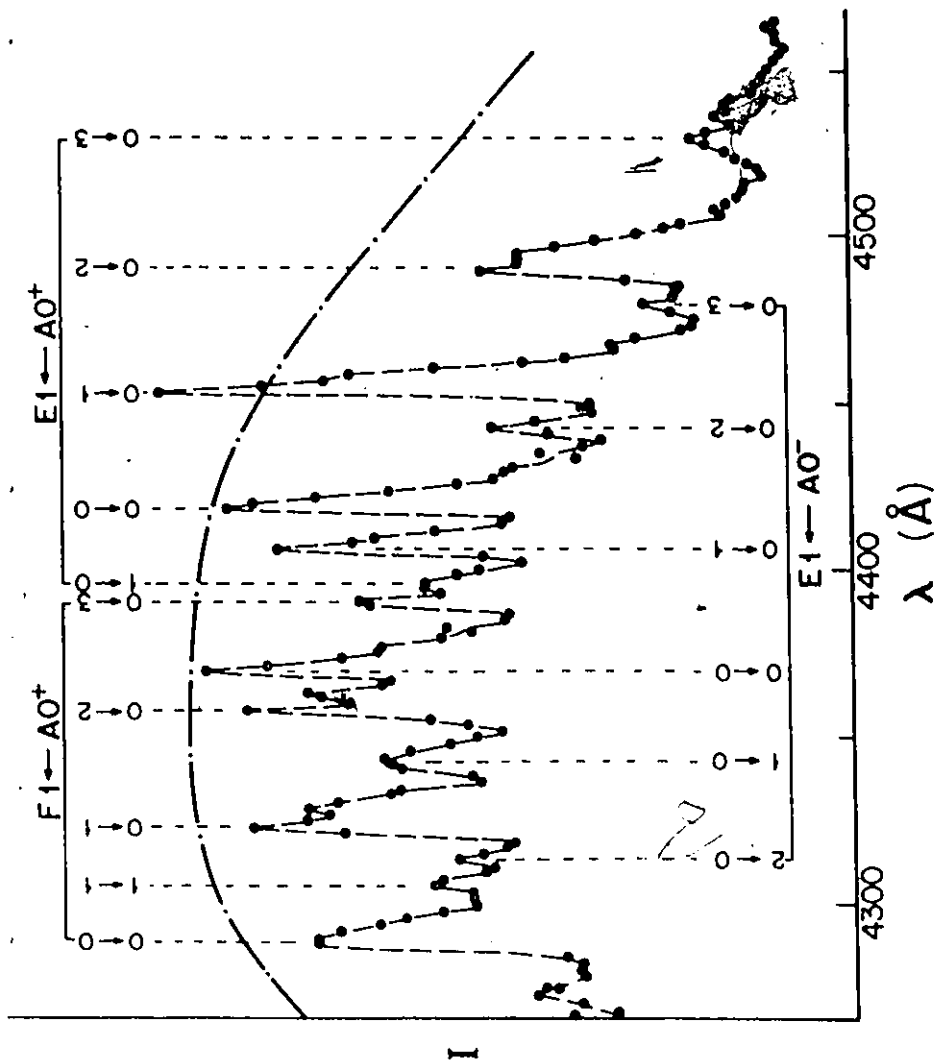


Figure 4.13 A trace of the fluorescence-monitored excitation spectrum at 2250 Å, showing the vibrational structures of the $F1 \leftarrow A0^+$, $E1 \leftarrow A0^-$ and $E1 \leftarrow A0^+$ band systems. The $v' \leftarrow v''$ assignments are shown on the trace. The dashed line represents the dye-laser power curve.

The most intense components, at 4450 Å and 4490 Å, arise from the $E1 \leftarrow A0^+$, $v' = 0 \leftarrow v'' = 1$ and $v' = 0 \leftarrow v'' = 2$, transitions, respectively.

The excitation spectrum recorded by monitoring the fluorescence at 2340 Å, 2460 Å, 2600 Å, or 2650 Å, peaks in the background bound-continuum fluorescence spectrum, had a structure quite different from that shown in Fig. 4.13, confirming our conclusions concerning the origin of the fluorescence peak at 2340 Å appearing in Figs. 4.10, 4.11, and 4.12. The peak near 2340 Å might be a result of bound-continuum transitions, to the $X0^+$ ground state, from some vibrational levels of the second PE well in the $E1$ state which might have been excited indirectly. The broad 'background' fluorescence spectrum, on the other hand, might be due to bound-continuum transitions, to the $X0^+$ ground state, from high-lying vibrational levels of the $C0^+$ state which might have also been excited indirectly through the complex PE curve-crossings.

The shapes of the vibrational components of the excitation band can provide an indication of the relative r_e values associated with the states involved in the transition. When the r_e values are similar, so are the rotational constants and, because of the rotational selection rules ($\Delta J = 0, \pm 1$), the rotational profile of a particular vibrational component is expected to be relatively narrow; the larger the difference between the r_e values, the greater the width

of the rotational profile. As was described in section 2.3, when the vibrational components exhibit steep leading edges on the short-wavelength sides, $r_e' > r_e''$. If the steep edges appear on the long-wavelength sides, then $r_e' < r_e''$. The components of the v'' progressions associated with the E1 and F1 states seen in Figs. 4.13 and 4.14, are relatively narrow, exhibit steep leading edges and are degraded towards longer wavelengths. These features, which I ascribe to the effects of rotational structure, reinforce the conclusion that the r_e values of the $A0^-$ and $A0^+$ states on the one hand, and F1 and E1 states on the other, are nearly equal to one another, with r_e' somewhat larger than r_e'' . The separation of the F1 and E1 levels, determined from the excitation spectrum, agrees within experimental error with the spacing estimated from the bound-continuum spectra in Figs. 4.10 and 4.12.

4.3.3 The Bound-Bound Fluorescence and Excitation Spectra Arising from $F1 \leftrightarrow A0^+$ Transitions

Figure 4.15 shows a trace of the $F1 \rightarrow A0^+$ (bound-bound) fluorescence band excited with the probe-laser wavelength 4323 Å which induced the $v' = 0 \leftarrow v'' = 1$ transition. The structure of the spectrum represents a v'' progression with a spacing of $190 \pm 3 \text{ cm}^{-1}$, corresponding to ω_e for the $A0^+$

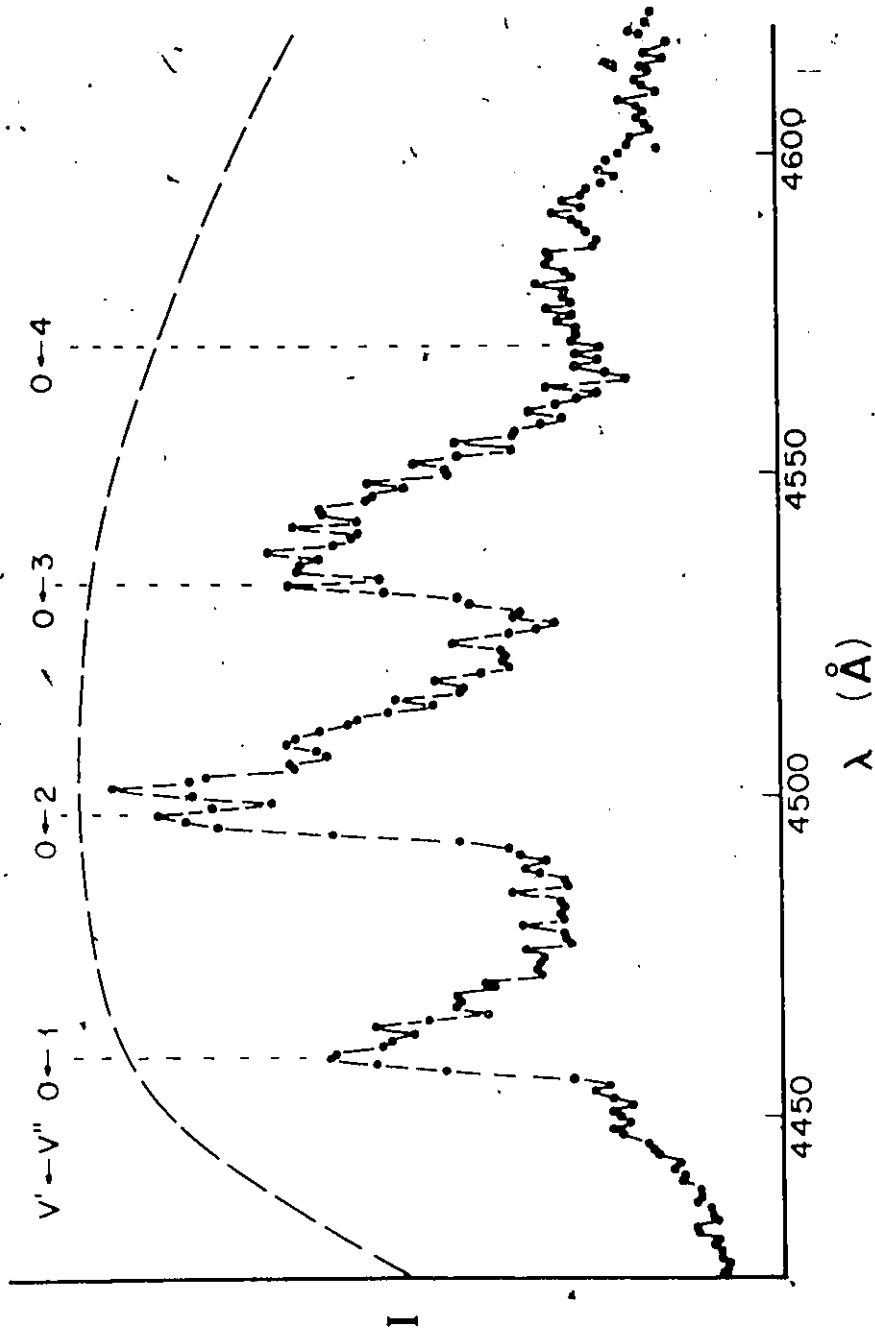


Figure 4.14 A trace of the fluorescence-monitored excitation spectrum at 2250 Å, showing the $E1 \leftarrow A0^+$ band system in the region 4420-4620 Å. The dashed line represents the dye-laser power curve.

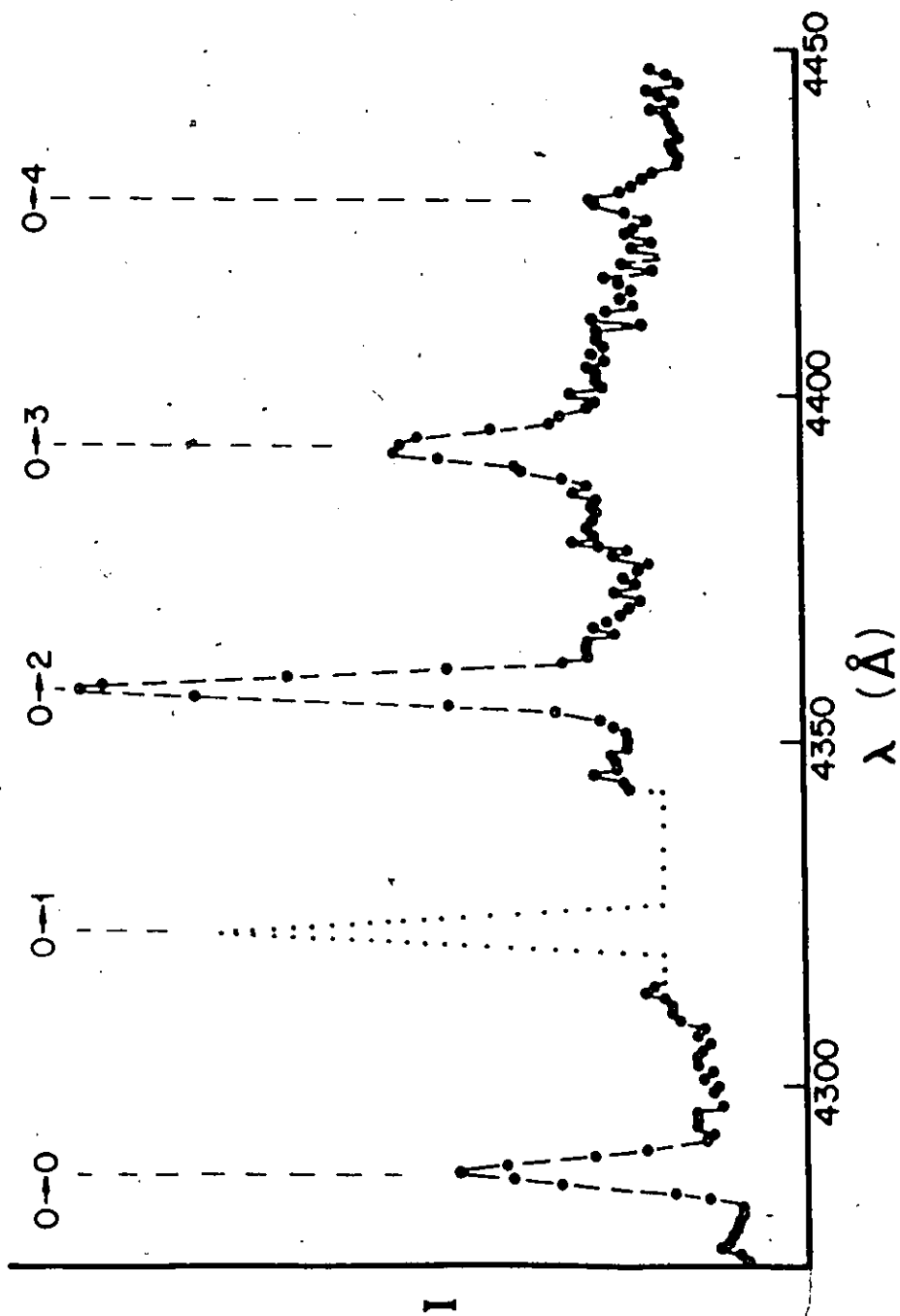


Figure 4.15 A trace of the F1 \rightarrow A0⁺ fluorescence band, showing $v' = 0 \rightarrow v''$ assignments.

state. The $v' = 0 \leftarrow v'' = 0$ component is at 4288 Å and thus the energy difference between the $v = 0$ levels of the F1 and $A0^+$ states is $23314 \pm 12 \text{ cm}^{-1}$. The vibrational components are identified on the trace and are listed in Table 4.1; their relative intensities are typical of a $v' = 0$ emission. Figure 4.16 shows the corresponding fluorescence band arising from $v' = 1 \rightarrow v''$ decays. The $v' = 1$ level was populated by $v' = 1 \leftarrow v'' = 0$ absorption, using the probe wavelength 4258 Å. The spectrum shows an intensity distribution typical for a $v' = 1$ emission.

I also observed the F1 \leftarrow $A0^+$ excitation spectra containing $v' = 0 \leftarrow v''$ and $v' = 1 \leftarrow v''$ progressions, which had structures similar to the fluorescence spectra in Figs. 4.15 and 4.16. Δr_e between the E1 and $A0^+$, E1 and $A0^+$, and F1 and $A0^+$ states were estimated to be $0.13 \pm 0.01 \text{ Å}$, using the computer-simulated modelling in the Appendix.

4.3.4 Predissociation of the F1 State

When the probe-laser radiation was tuned at a wavelength corresponding to any peak on the F1 \leftarrow $A0^+$ excitation spectrum shown in Fig. 4.13, intense emission was also detected at 4916 Å, which corresponded to the Hg $8^1S_0 \rightarrow 6^1P_1$ transition³⁷. To investigate this phenomenon further, the probe laser was scanned in the region 4200 - 4450 Å while

Table 4.1 Vibrational components of the $F1 \rightarrow A0^+$ fluorescence band; the measured $\lambda(\text{\AA})$ are given in air; $\nu(\text{cm}^{-1})$ are stated in vacuo.

$v' \rightarrow v''$	$\lambda(\text{\AA})$	$\nu(\text{cm}^{-1})$	$\Delta\nu(\text{cm}^{-1})$
0 - 0	4288±1	23314.4±5	188.8
0 - 1	4323±1	23125.6±5	185.7
0 - 2	4358±1	22939.9±5	188.0
0 - 3	4394±2	22751.9±10	179.8
0 - 4	4429±3	22572.1±15	
1 - 0	4258±1	23478.6±5	186.0
1 - 1	4292±1	23292.6±5	188.4
1 - 2	4327±3	23104.2±15	180.1
1 - 3	4361±1	22924.1±5	182.5
1 - 4	4396±1	22741.6±5	184.8
1 - 5	4432±2	22556.8±10	176.7
1 - 6	4467±3	22380.1±15	

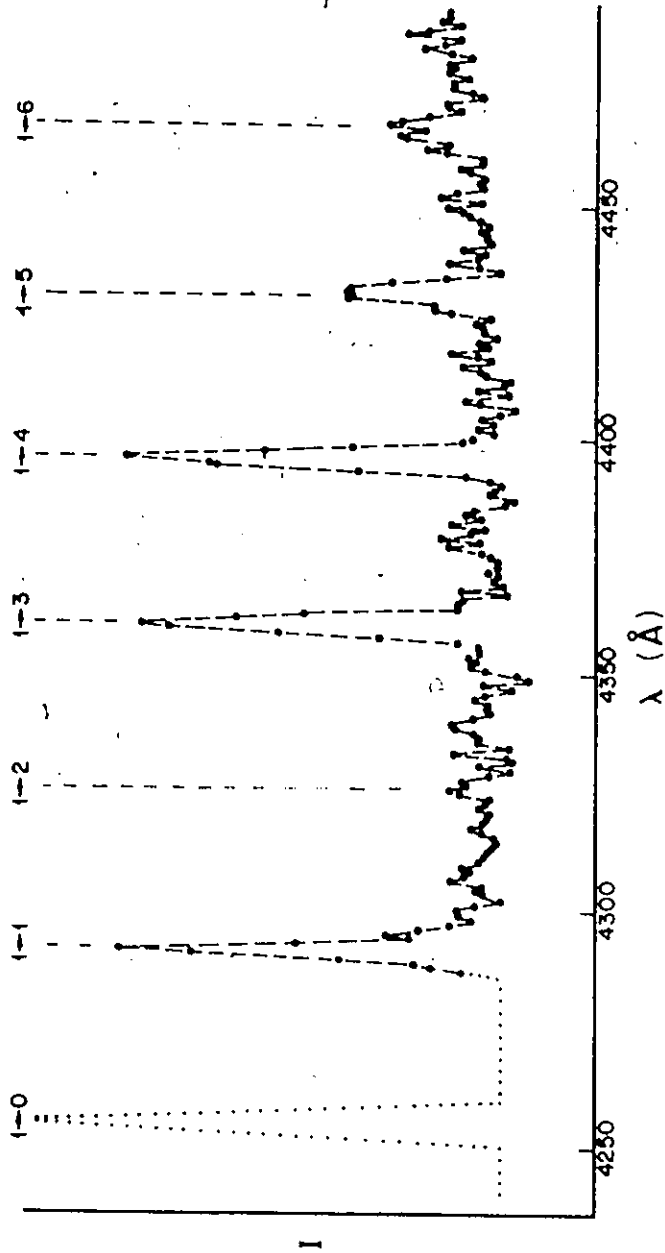


Figure 4.16 A trace of the $F1 \rightarrow A0^+$ fluorescence band, showing $v' = 1 \rightarrow v''$ assignments.

monitoring the emitted fluorescence at 4916 Å. It was found that this produced an excitation spectrum nearly identical with the $F1 \leftarrow A0^+$ excitation spectrum shown in Fig. 4.13 and observed when the fluorescence signal was monitored in the UV (on the bound-free $F1 \rightarrow X0^+$ transitions), or in the blue region (on the bound-bound $F1 \rightarrow A0^+$ transitions shown in Fig. 4.15). There were slight differences between the spectra because, in the bound-bound transitions, the excitation spectrum showed a pure v'' progression resulting from the decay of a selectively excited upper vibrational level whereas, in the spectrum monitored at 4916 Å, the excitation spectrum included other progressions, as may be seen in Fig. 4.17.

Figure 4.18 shows a trace of the Hg 4916 Å emission line produced by using probe-laser wavelength at 4288 Å, which corresponded to the $F1, v' = 0 \leftarrow A0^+, v'' = 0$ transition, and scanning the monochromator in the 4850 - 5000 Å region. The background signal represented the extended tail of the persistent blue fluorescence band at 4750 Å, which was excited by the pump pulses. The same atomic emission line was observed when the probe-laser wavelength was set to correspond to any peak on the $F1 \leftarrow A0^+$ excitation spectrum. When the monochromator was scanned in the spectral region from 2300 Å to 7000 Å, no other atomic emissions were detected.

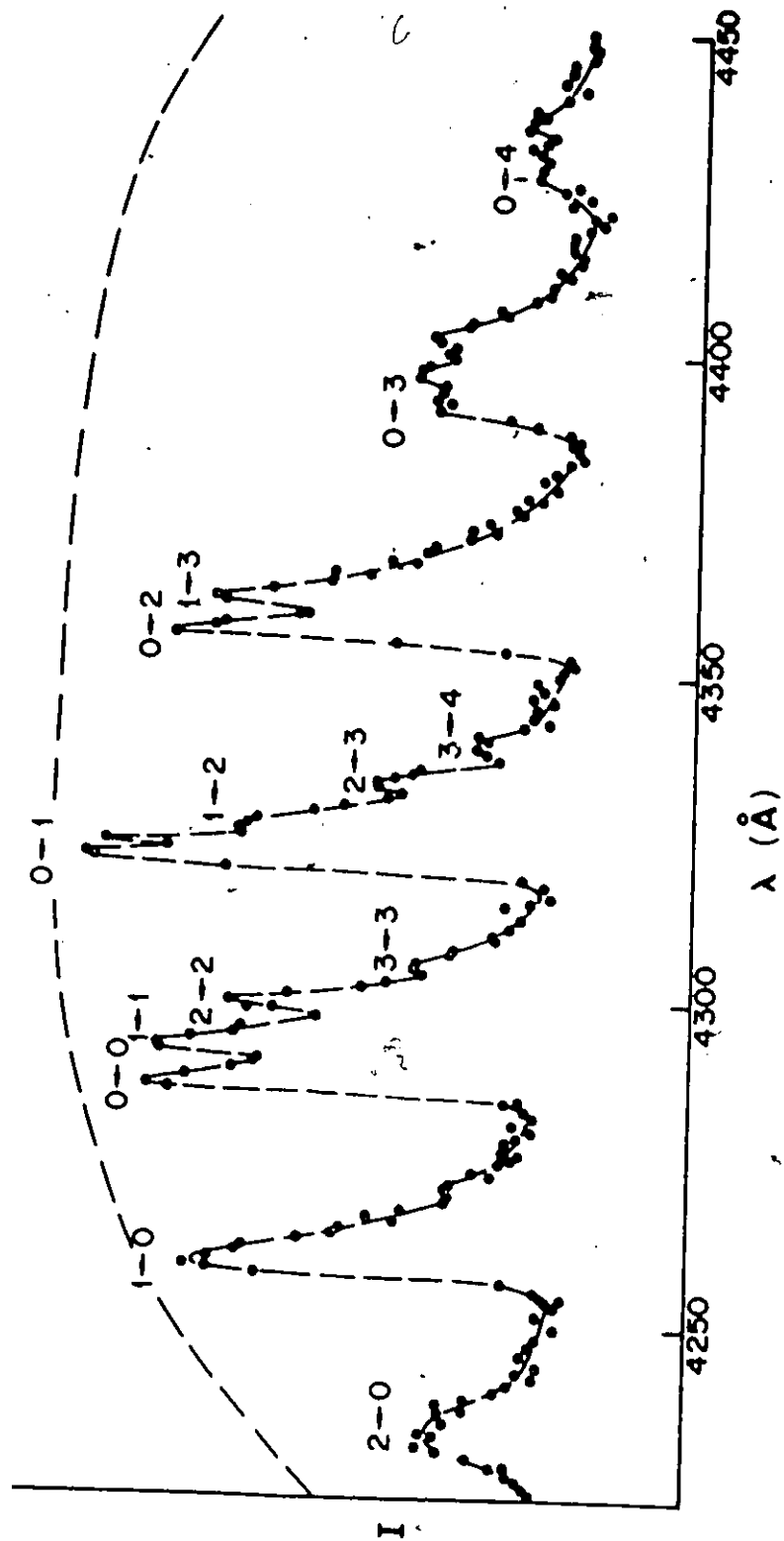


Figure 4.17 The $F1 \leftarrow A0^+$ excitation spectrum, showing $v' \leftarrow v''$ assignments. The spectrum was monitored at 4916 \AA . The dashed curve indicates relative dye-laser power.

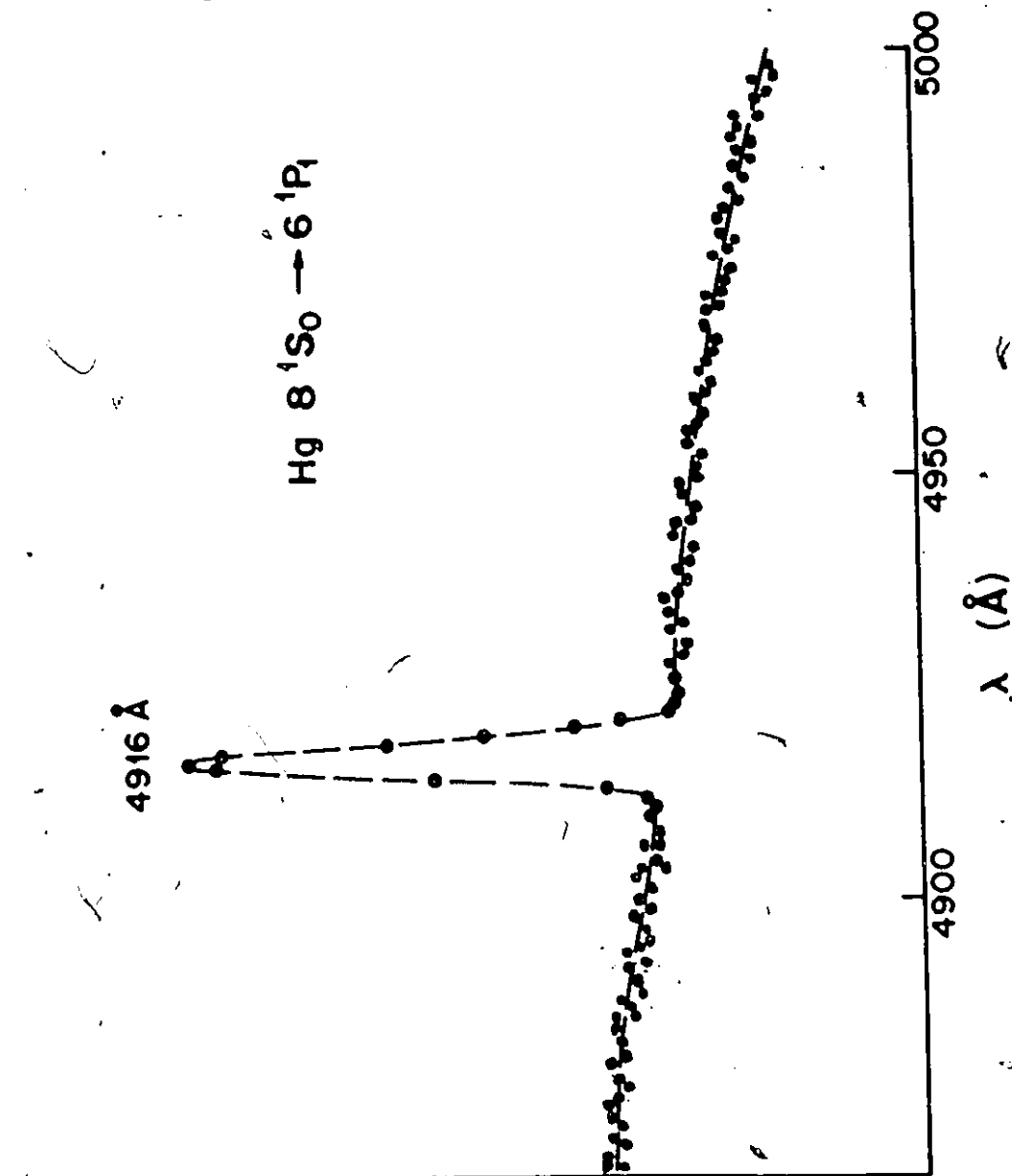
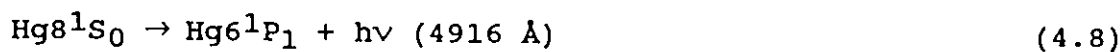
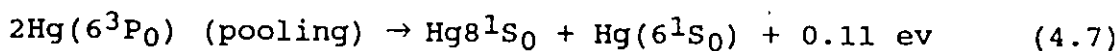
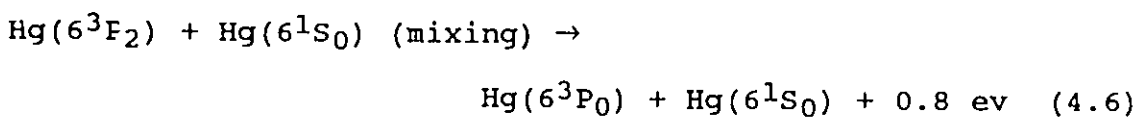
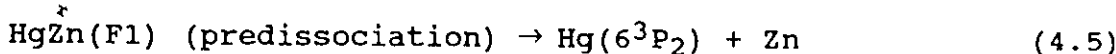
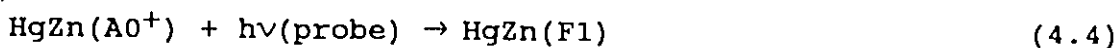
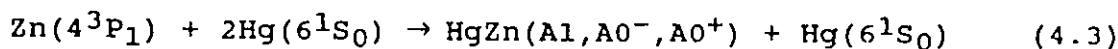
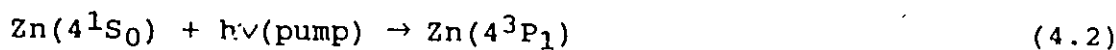


Figure 4.18 Hg 4916 Å fluorescence used to monitor the $F1 \leftarrow A0^+$ excitation spectrum. The background signal represents the tail of the 4750 Å band.

I suggest that the Hg 4916 Å radiation emitted in the Hg $8^1S_0 \rightarrow 6^1P_1$ decay was due to the predissociation of the F1 HgZn molecules, followed by collisional mixing and pooling among Hg $6^3P_{0,1,2}$ atoms. The predissociation occurred through the curve-crossing between the F1 state and the repulsive $D0^-$ state and produced Hg 6^3P_2 metastable atoms. Because of collisional mixing and the strong imprisonment of the Hg 2537 Å ($6^3P_1 \rightarrow 6^3S_0$) resonance radiation, the 6^3P_0 state was also highly populated and had a relatively long effective lifetime which was limited by the decay time of the imprisoned resonance radiation. This created favourable conditions for pooling collisions of 6^3P_0 atoms, which resulted in the population of the Hg 8^1S_0 state and the emission of the 4916 Å radiation accompanying the $8^1S_0 \rightarrow 6^1P_1$ decay³⁷. The mechanism may be represented as follows:



The partial PE diagram for the states participating in the predissociation, pooling and decay processes is shown in Fig. 4.19.

The signal-to-noise ratio in Figs. 4.17 and 4.18 is very high and comparable to the other HgZn excitation and fluorescence spectra, suggesting that the mechanism by which the Hg 8^1S_0 state was populated must have been quite efficient. Further evidence for the mechanism involving the predissociation and pooling processes was provided by comparing the time evolution of the 4750 Å fluorescence band, emitted in the decay of the A1 and A0⁺ reservoir states to the X0⁺ ground state, with the variation of the 4916 Å LIF intensity in relation to the pump-probe delay. The comparison, shown in Fig. 4.20, showed identical rise- and decay-times which confirmed that the lower state involved in the bound-bound absorption was a reservoir state correlated with the Hg($1S$)+Zn($3P$) atomic states. The possibility of pooling collisions between Zn 4^3P_0 and Hg 6^3P_0 atoms was also ruled out because of the large energy defect and also, because after a delay of 450 ns, the density of Zn 4^3P_0 atoms was quite low as may be seen in Fig. 4.2.

It has been reported that collisions between two Hg atoms in the $6^3P_{0,1,2}$ states have been investigated³⁸ and it is known that collisions between two 6^3P_1 atoms give rise to the Hg emission at 4108 Å and 6123 Å, $6^3P_0 - 6^3P_1$ collisions give rise to the Hg emission at 6907 Å and 6072 Å, $6^3P_0 -$

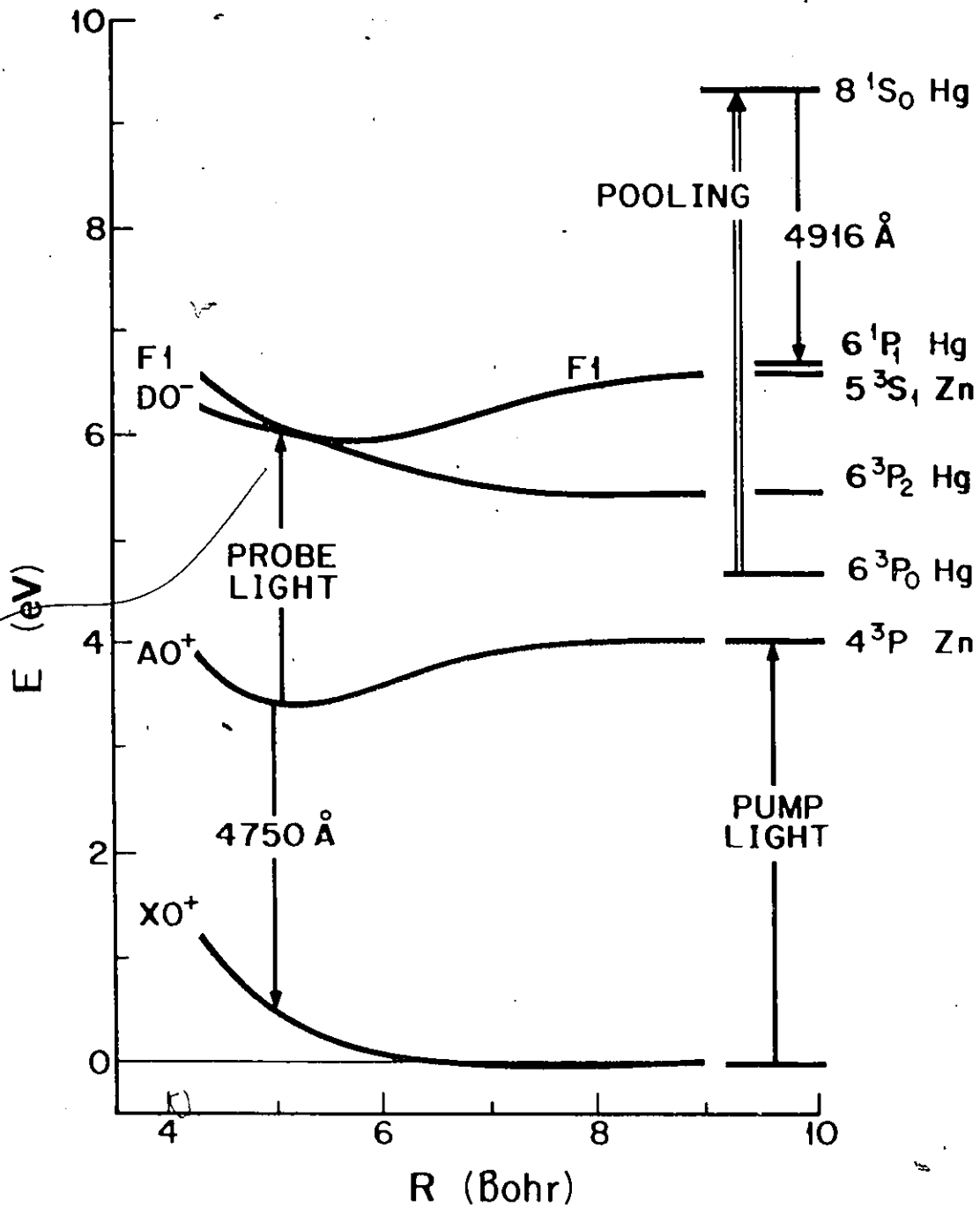


Figure 4.19 A partial PE diagram showing predissociation and pooling resulting in 4916 Å emission.

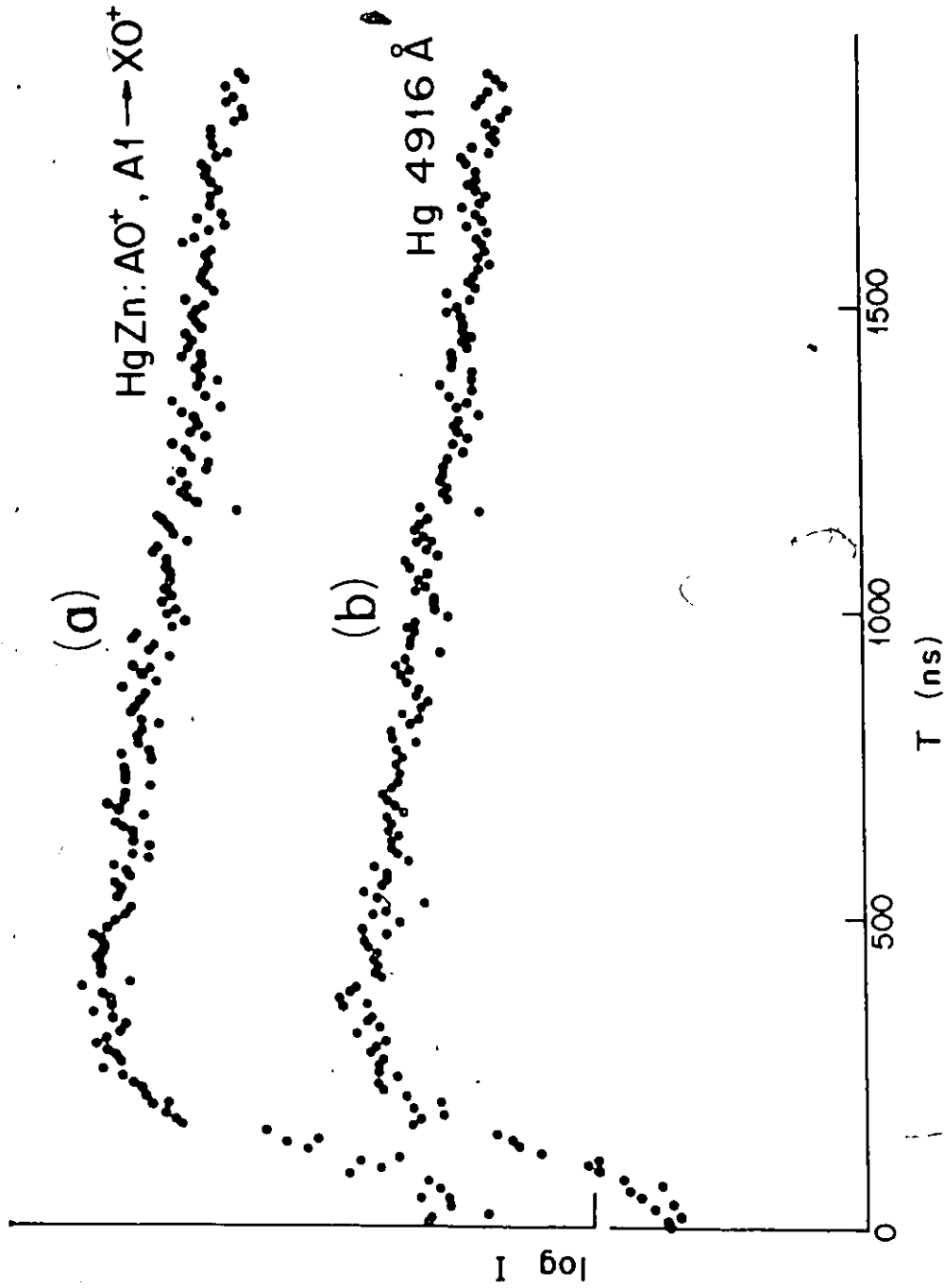


Figure 4.20 Time-evolution of the fluorescence. (a) The 4750 Å band excited with pump pulses only; (b) Hg 4916 Å atomic fluorescence intensity plotted against pump-probe (4318 Å) delay.

6^3P_2 collisions produce Hg emission at 5354 Å, and $6^3P_0 - 6^3P_0$ collisions give rise to the Hg 4916 Å emission. The fact that, in this experiment only the 4916 Å line was detected, is attributed to the Boltzmann distribution according to which the 4916 Å Hg line should be expected to be at least 20 times more intense than the lines produced by $6^3P_0 - 6^3P_1$ collisions and 400 times more intense than the lines produced by $6^3P_1 - 6^3P_1$ collisions. Three-body collisions among the Hg $6^3P_{0,1,2}$ atoms were not expected to give rise to any Hg emission lines³⁸ even though the Hg vapor pressure reached 2.2 atm during the experiment.

The excitation spectrum shown in Fig. 4.17 includes more vibrational components than are shown in Fig. 4.13. This is because all vibrational levels can participate in the curve crossing and predissociation giving rise to the 4916 Å emission, while the excitation spectrum recorded by monitoring the bound - continuum UV fluorescence from the molecule favoured particular vibrational levels of the F1 state. The relative intensities of the components in Fig. 4.17 are determined by the FC factors as well as the thermal distribution over the vibrational levels of the $A0^+$ state.

The vibrational constants of the $A0^+$ and F1 states were calculated by substituting the frequencies and frequency separations of the $F1 \leftarrow A0^+$ band system into the standard term equation (2.22). The results were found to be identical with the results obtained in sections 4.3.1.2 and 4.3.3.

This part of the experiment made a useful contribution to the analysis of the $F1 \leftarrow A0^+$ excitation spectrum which was very complex, as may be seen in Fig. 4.13. The results, together with the PE curves, also confirmed the assignment of the F1 state as that which underwent radiative decays to the $X0^+$ and $A0^+$ states and predissociation through a curve-crossing.

4.4 Excitation and Decay of the $E0^-$ State

As the probe-laser was scanned across the 4000 - 4450 Å wavelength region, two bound-bound resonance fluorescence spectra were detected in this region and another bound-bound spectrum was detected in the 4600 - 4780 Å region. The analysis indicated the presence of one upper state and three lower states participating in the transitions. I have identified the upper state as the $E0^-$ state, and the lower states as the $A1$, $A0^-$ and $B0^-$ states³⁹.

The three fluorescence spectra were excited when the probe-laser was tuned to any vibrational component of the $E0^- \leftarrow A1$ or $E0^- \leftarrow A0^-$ band systems, but not of the $E0^- \leftarrow B0^-$ band system and, accordingly, only two excitation spectra were recorded. This observation indicated that the $B0^-$ state was not populated by the pump pulses because of the Boltzmann factor. A PE diagram showing the the $X0^+$, $A1$, $A0^-$, $A0^+$, $B0^-$ and $E0^-$ states is sketched in Fig. 4.21.

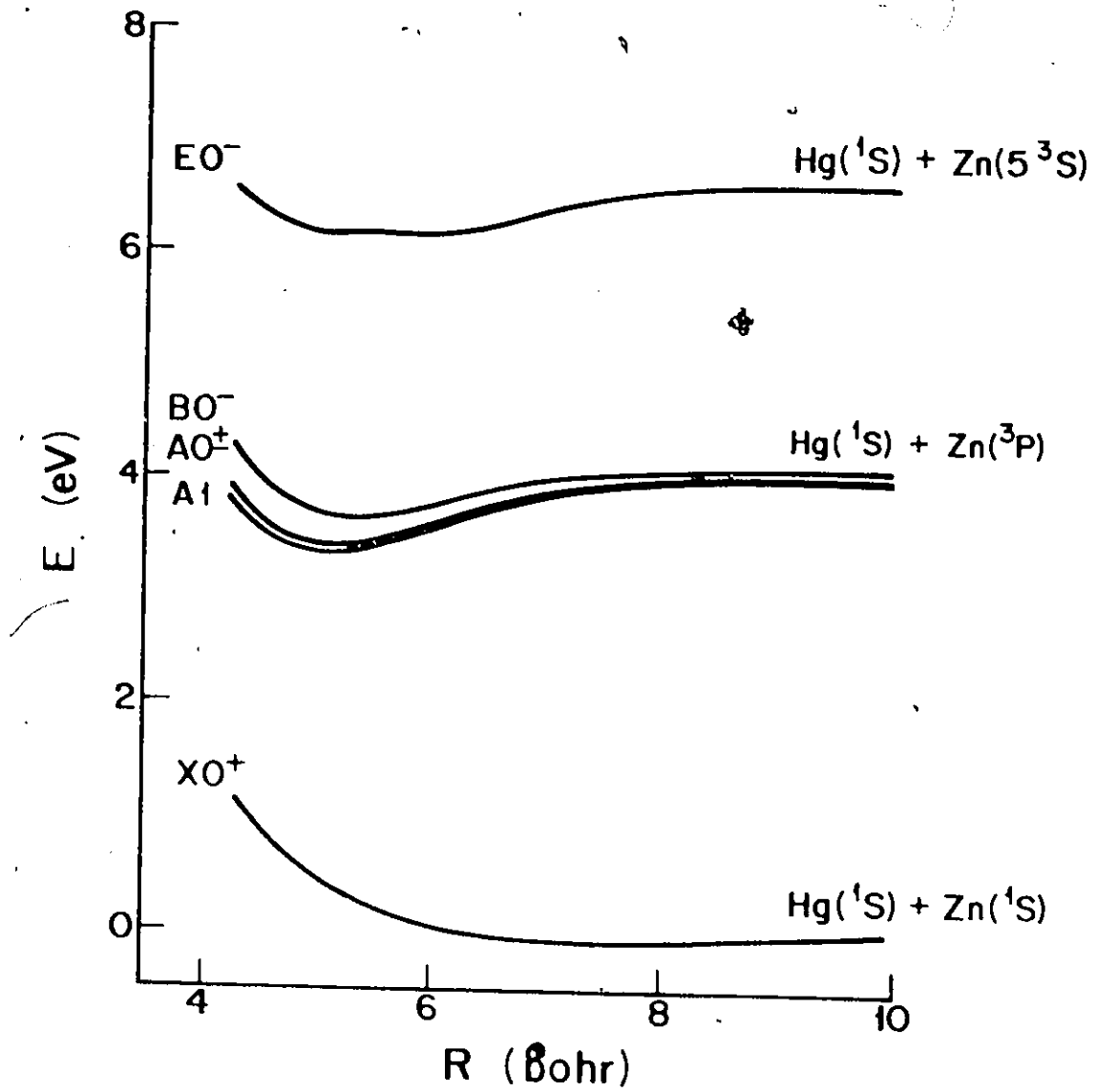


Figure 4.21 A partial PE diagram showing the $\text{X}0^+$, $\text{A}1$, $\text{A}0^-$, $\text{A}0^+$, $\text{B}0^-$ and $\text{E}0^-$ states.

4.4.1 The Fluorescence Spectrum in the 4000 - 4450 Å Region

Figure 4.22 shows a trace of two superimposed fluorescence spectra emitted in the bound-bound decay of the $E0^-$, $v' = 0$ level to the $A1$ and $A0^-$ states. The $v' = 0$ level was excited with the probe-laser wavelength 4189 Å corresponding to the $E0^-, v' = 0 \leftarrow A1, v'' = 2$ transition; the corresponding vibrational component, which is indicated with a dashed profile, was not recorded in fluorescence because of the background from scattered laser light.

The $v' = 0 \rightarrow v'' = 0$ components were located at 4122 Å in the $E0^- \rightarrow A1$ band system and at 4236 Å in the $E0^- \rightarrow A0^-$ band system. Accordingly, the energy separation between the $v = 0$ levels of the $A1$ and $A0^-$ states was found to be $653 \pm 10 \text{ cm}^{-1}$. The intensity profile of the spectrum has the shape of two intermingled distributions, typical of $v' = 0$ emission bands. The pattern of relative intensities among the vibrational components is similar in both bands, with transitions to $v'' > 5$ being too weak to be detected. This suggests that the r_e values associated with the states $A1$ and $A0^-$ are almost equal. The trace shows the vibrational assignments of the various components and the spectrum also includes the atomic Hg 4358 Å and 4047 Å lines which serve as convenient points of reference.

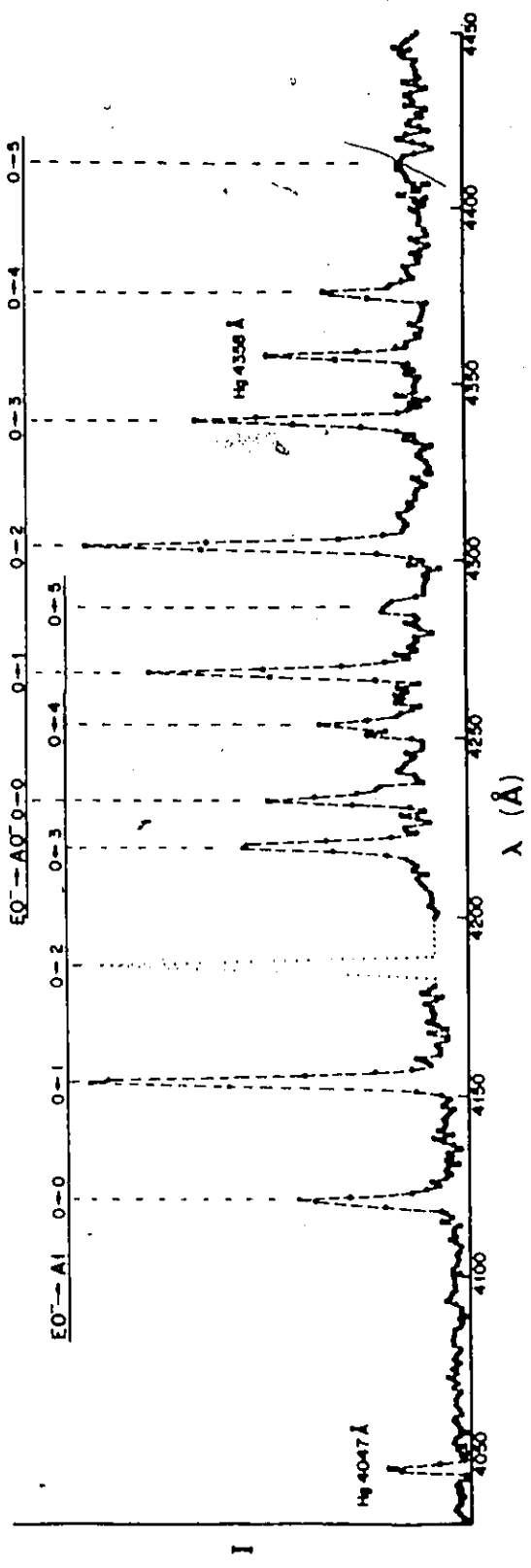


Figure 4.22 A trace of two fluorescence bands arising from $EO^- \rightarrow A1$ and $EO^- \rightarrow A0$ transitions, showing $v' = 0 \rightarrow v''$ assignments. The dashed profile indicates the peak corresponding to the probe wavelength.

Probe laser radiation at 4096 Å excited the $E0^-$, $v' = 1 \leftarrow A1$, $v'' = 0$ transition. The subsequent decay resulted in the emission of the fluorescence spectrum shown in Fig. 4.23 which includes both $E0^- \rightarrow A1$ and $E0^- \rightarrow A0^-$ bands, as well as the 4047 Å, 4358 Å and 5461 Å Hg lines. The mechanism leading to the emission of these lines has not yet been elucidated.

The wavelengths, frequencies and frequency separations of the vibrational components of the $E0^- \rightarrow A1$ and $E0^- \rightarrow A0^-$ band systems are listed in Tables 4.2 and 4.3, respectively. The frequencies were substituted in the standard term equation (2.22) and used in a least-squares analysis which yielded the following vibrational constants: $\omega_e = 195 \pm 3 \text{ cm}^{-1}$ and $\omega_e x_e = 0.88 \pm 0.2 \text{ cm}^{-1}$ for the A1 state, and $\omega_e = 194 \pm 3 \text{ cm}^{-1}$ and $\omega_e x_e = 0.7 \pm 0.2 \text{ cm}^{-1}$ for the $A0^-$ state.

4.4.2 The Fluorescence Spectrum in the 4600 - 4780 Å Region

A very intense bound-bound fluorescence spectrum, registered in the 4600 - 4780 Å region, is attributed to transitions between the vibrational levels of the $E0^-$ state and those of a lower state which is believed to be the $B0^-$ state. A trace of this band, shown in Fig. 4.24, exhibits a v'' progression which represents the vibrational spacing of

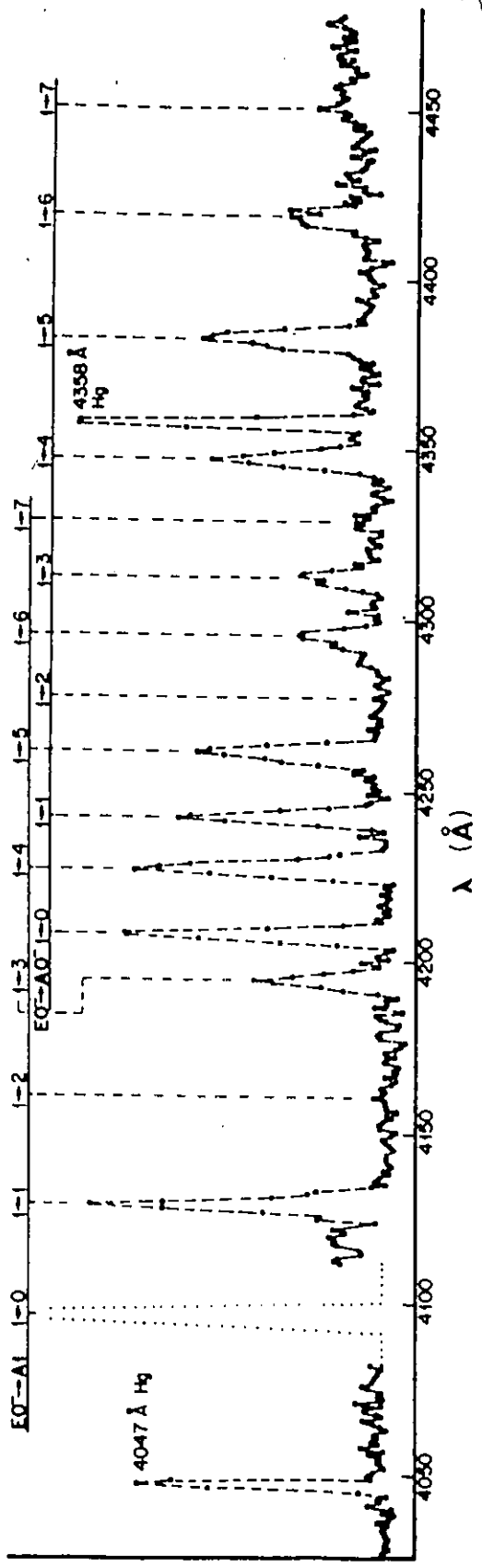


Figure 4.23 A trace of two fluorescence bands arising from $E0^- \rightarrow A1$ and $E0^- \rightarrow A0^-$ transitions, showing $v' = 1 \rightarrow v''$ assignments. The dashed profile indicates the peak corresponding to the probe wavelength.

Table 4.2 Vibrational components of the $E0^- \rightarrow A1$ fluorescence band; the measured $\lambda(\text{\AA})$ are given in air, $\nu(\text{cm}^{-1})$ are stated in vacuo.

$\nu' \rightarrow \nu''$	$\lambda(\text{\AA})$	$\nu(\text{cm}^{-1})$	$\Delta\nu(\text{cm}^{-1})$
0 - 0	4122±1	24253.3±5	
			198.4
0 - 1	4156±1	24054.9±5	
			189.5
0 - 2	4189±1	23865.4±5	
			192.2
0 - 3	4223±1	23673.2±5	
			183.5
0 - 4	4256±1.5	23489.7±8	
			186.2
0 - 5	4290±2	23303.5±10	
1 - 0	4096±1	24407.2±5	
			189.2
1 - 1	4128±1	24218.0±5	
			192.0
1 - 2	4161±2	24026.0±10	
			189.1
1 - 3	4194±1	23836.9±5	
			191.7
1 - 4	4228±1.5	23645.2±8	
			183.0
1 - 5	4261±1	23462.1±5	
			185.7
1 - 6	4295±2	23276.4±10	
			182.8
1 - 7	4329±3	23093.6±15	

Table 4.3 Vibrational components of the $E0^- \rightarrow A0^-$ fluorescence band; the measured $\lambda(\text{\AA})$ are given in air, $\nu(\text{cm}^{-1})$ are stated in vacuo.

$\nu' \rightarrow \nu''$	$\lambda(\text{\AA})$	$\nu(\text{cm}^{-1})$	$\Delta\nu(\text{cm}^{-1})$
0 - 0	4236±1	23600.6±5	
0 - 1	4271±1	23407.2±5	193.4
0 - 2	4306±1	23216.9±5	190.3
0 - 3	4342±1	23024.4±5	192.5
0 - 4	4377±2	22840.3±10	184.1
1 - 0	4208±1	23757.6±5	190.4
1 - 1	4242±1	23567.2±5	192.9
1 - 2	4277±2	23374.3±10	189.7
1 - 3	4312±2	23184.6±10	186.7
1 - 4	4347±1	22997.9±5	188.9
1 - 5	4383±2	22809.0±10	185.8
1 - 6	4419±3	22623.2±15	182.8
1 - 7	4455±4	22440.4±20	

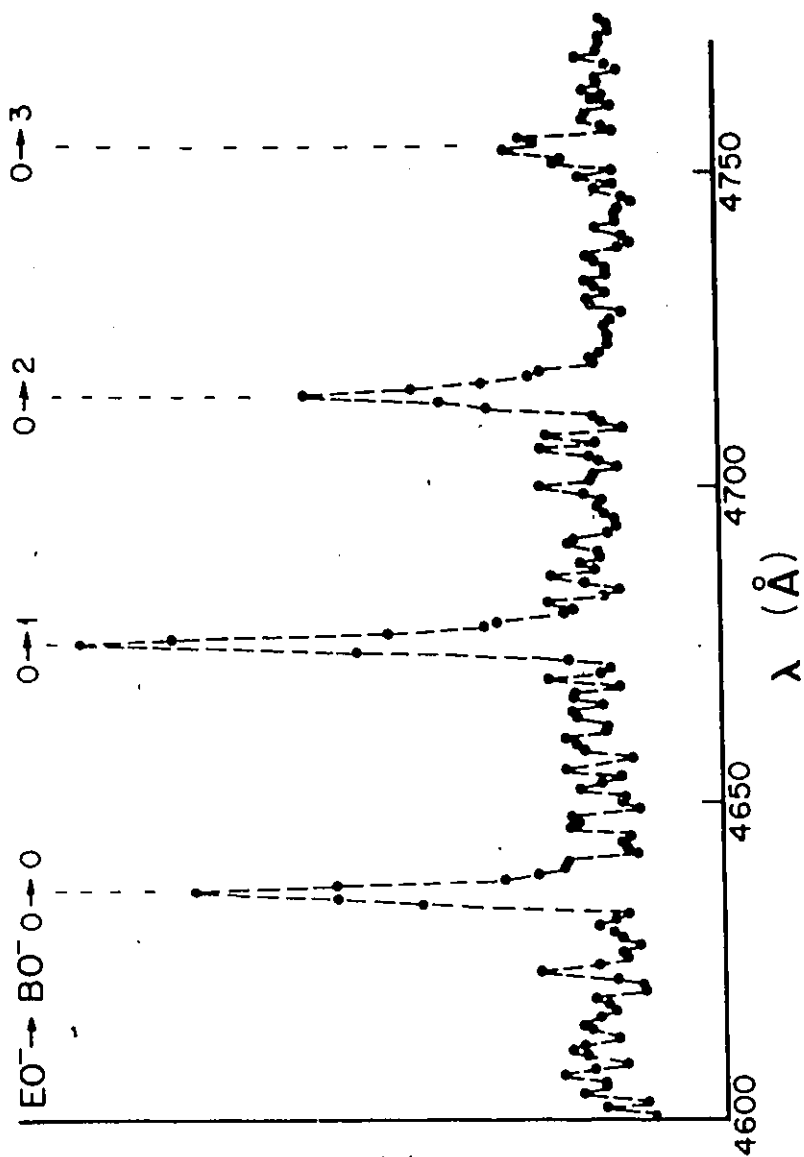


Figure 4.24 A trace of the fluorescence band excited with 4189 Å probe radiation and originating from the $E0^-, v' = 0 \rightarrow B0^-, v''$ transitions, showing $v' \rightarrow v''$ assignments.

the B_0^- state. The band was excited with 4189 Å probe radiation which excited the $E_0^-, v' = 0 \leftarrow A_1, v'' = 2$ transition. The most intense fluorescence component corresponds to the $E_0^-, v' = 0 \rightarrow B_0^-, v'' = 1$ emission at 4676 Å; components due to transitions from $v' = 0$ to $v'' > 4$ were too faint to be detected because of low FC factors and because of the intense fluorescence continuum emitted by the long-lived $A_1 A_0^+$ excimer which has a peak at 4750 Å. From the wavelength of the $E_0^-, v' = 0 \rightarrow B_0^-, v'' = 0$ component, which I found to be 4637 Å, I concluded that the $B_0^- - A_1$ energy separation was $2694 \pm 10 \text{ cm}^{-1}$. Figure 4.25 shows the trace of the fluorescence band resulting from the decay of the $E_0^-, v' = 1$ level to various B_0^-, v'' levels. The $v' = 1$ level was excited with 4096 Å probe radiation which induced the $E_0^-, v' = 1 \leftarrow A_1, v'' = 0$ transition. The relative intensities of the vibrational components are determined mainly by the FC factors; again, components arising from $v' = 1 \rightarrow v'' > 5$ transitions were too faint to be detected. The wavelengths, frequencies and frequency separations of the components in the $E_0^- \rightarrow B_0^-$ band are listed in Table 4.4. When substituted in the standard term equation (2.22) and subjected to least-squares analysis, they yielded the vibrational constants for the B_0^- state; $\omega_e = 181.5 \pm 2 \text{ cm}^{-1}$ and $\omega_e x_e = 1.0 \pm 0.2 \text{ cm}^{-1}$.

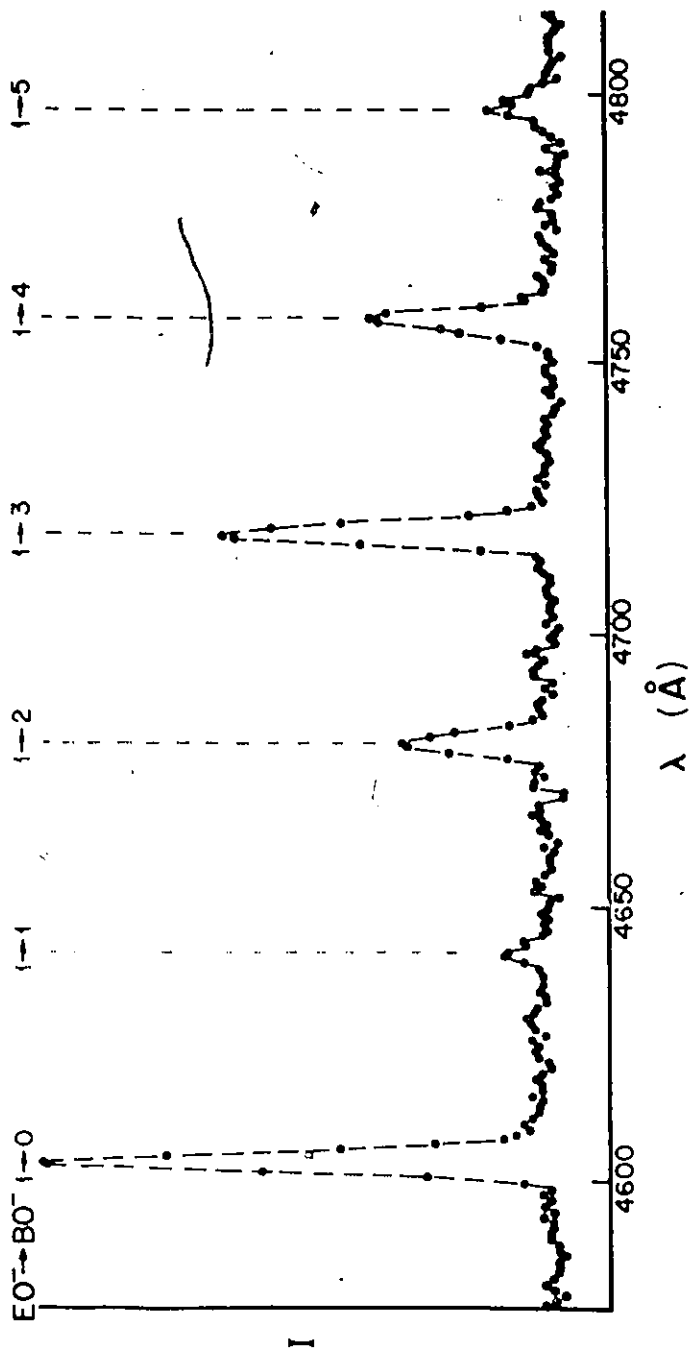


Figure 4.25 A trace of the fluorescence band excited with 4096 \AA probe radiation and originating from the $E0^-$, $v' = 1 \rightarrow B0^-, v''$ transitions, showing $v' \rightarrow v''$ assignments.

Table 4.4 Vibrational components of the $E0^- \rightarrow B0^-$ fluorescence band; the measured $\lambda(\text{\AA})$ are given in air, $\nu(\text{cm}^{-1})$ are stated in vacuo.

$v' \rightarrow v''$	$\lambda(\text{\AA})$	$\nu(\text{cm}^{-1})$	$\Delta\nu(\text{cm}^{-1})$
0 - 0	4637±1	21559.6±5	
0 - 1	4676±1	21379.8±5	179.8
0 - 2	4715±1	21203.0±5	176.8
0 - 3	4754±2	21029.0±10	174.0
1 - 0	4603±1	21718.9±5	182.5
1 - 1	4642±1	21536.4±5	174.9
1 - 2	4680±1	21361.5±5	176.5
1 - 3	4719±1	21185.0±5	173.7
1 - 4	4758±1	21011.3±5	170.8
1 - 5	4797±2	20840.5±10	

4.4.3 The Excitation Spectrum in the 4180 - 4310 Å Region

Since the $E0^-$ state was found to emit fluorescence bands in its decay to the $A1$, $A0^-$ and $B0^-$ states, the $E0^- \leftarrow A1$ and $E0^- \leftarrow A0^-$ excitation spectra might be expected to have the same profiles when monitored at any wavelength corresponding to a vibrational component in the $E0^- \rightarrow A1$, $E0^- \rightarrow A0^-$ (4000-4450 Å) or $E0^- \rightarrow B0^-$ (4600-4780 Å) fluorescence bands. This I found to be the case; at the same time I also found that I was not able to produce an $E0^- \leftarrow B0^-$ excitation spectrum and concluded that the $B0^-$ state was not populated by the 3076 Å pump light. Figure 4.26 shows an excitation spectrum in the 4180 - 4310 Å region, monitored at 4676 Å, a fluorescence component which corresponds to the $E0^-, v' = 0 \rightarrow B0^-, v'' = 1$ transition; virtually identical profiles were recorded when the excitation spectrum was monitored on a vibrational component of the $E0^- \rightarrow A1$ or $E0^- \rightarrow A0^-$ fluorescence band. This consistency confirms the assignments of the bands to the various bound-bound transitions and reinforces my conclusions concerning the relative positioning of the $A1$, $A0^-$, $B0^-$ and $E0^-$ states on the energy scale.

The trace shown in Fig. 4.26 also resembles the central segment of the fluorescence spectrum shown in Fig. 4.22. This is not surprising since I believe both spectra to represent v'' progressions of the $A1$ and $A0^-$ states. Another

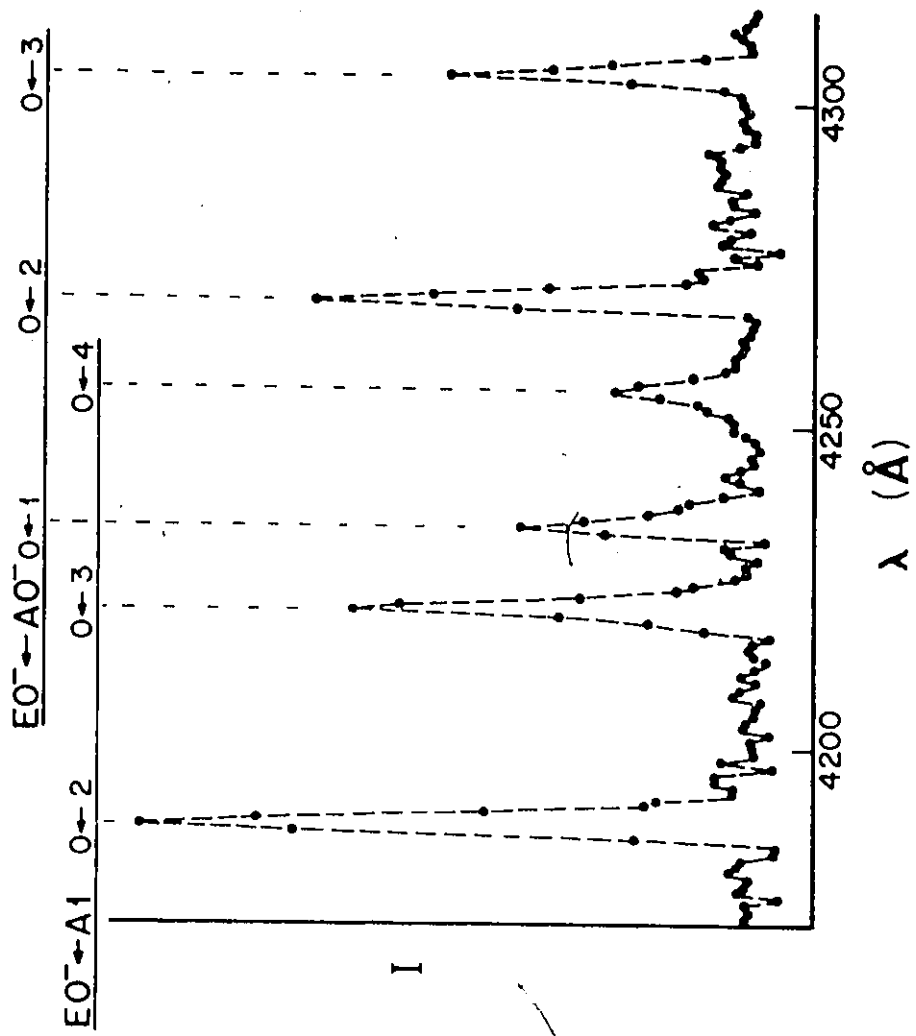


Figure 4.26 A trace of the $E0^-, v' = 0 \leftarrow A1, v''$ and $E0^-, v' = 0 \leftarrow A0^-, v''$ excitation bands, monitored at 4676 Å.

example of an excitation spectrum is shown in Fig. 4.27; there the $E0^-$, $v' = 1$ level was excited from various v'' levels of the $A1$ and $A0^-$ states and the spectrum was monitored at 4603 Å, a component corresponding to the $E0^-$, $v' = 1 \rightarrow B0^-$, $v'' = 0$ transition.

Δr_e between the $E0^-$ state and $A1$, $E0^-$ and $A0^-$, and $E0^-$ and $B0^-$ states were estimated to be 0.13 ± 0.01 Å, 0.13 ± 0.01 Å and 0.10 ± 0.01 Å, respectively, using the computer-simulated modelling in the Appendix.

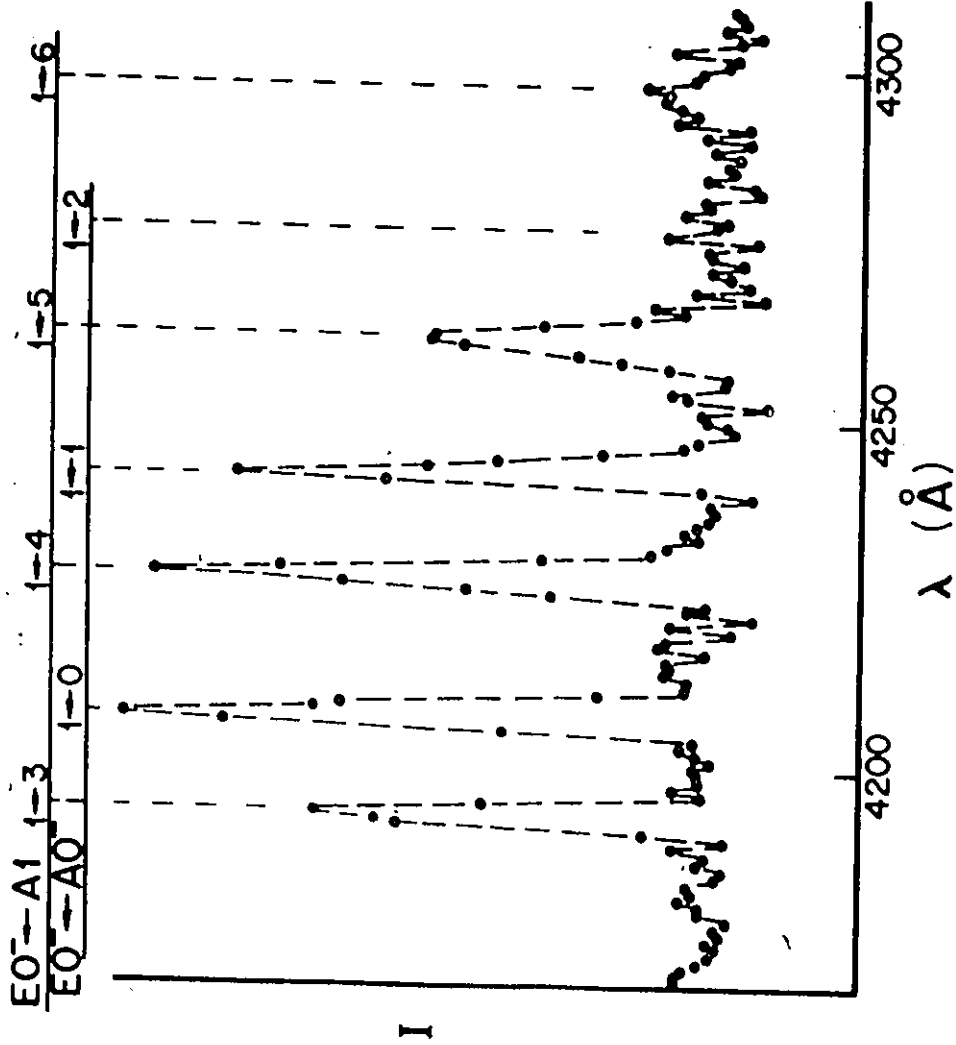


Figure 4.27 A trace of the E_0^- , $v' = 1 \leftarrow A_1^-$, v'' and E_0^- , $v' = 0 \leftarrow A_0^-$, v'' excitation bands, monitored at 4719 \AA .

5 SUMMARY AND CONCLUSIONS

Various excited HgZn states were excited by the pump-and-probe method which was used to record fluorescence and excitation spectra that have not been previously observed. The spectra were correlated with a PE diagram drawn and labelled according to Hund's case (c), which was produced simultaneously but independently of the experimental study^{15,16}. The various experimental results of this investigation may be summarized as follows:

1) The A1 and A0⁺ states were found to be the emitting states for the 6.1 μ s fluorescence band at 4750 Å, which was first reported by Eden¹ at 4600 Å.

2) The mechanism which gave rise to this fluorescence band, was confirmed to be a three-body-collision involving two Hg (6^1S_0) and one Zn (4^3P_1) atoms¹.

3) The reservoir states produced by the pump pulses, from which higher excimer states were excited by absorption of a probe pulse, were found to be the A1, A0⁻ and A0⁺ states.

4) The bound-continuum fluorescence band at 2500 Å, was identified as arising from C0⁺ \rightarrow X0⁺ decays; the C0⁺ state was populated by transitions from the A0⁺ reservoir state using probe laser wavelengths in the 5200 - 6650 Å region

and was not found to decay to any other state than $X0^+$.

5) The bound-continuum fluorescence bands near 2260 Å, were identified as arising from $E1 \rightarrow X0^+$ and $F1 \rightarrow X0^+$ decays. The $E1$ and $F1$ states were found to be excited by probe pulses in the 4200 - 4500 Å region, which induced $F1 \leftarrow A0^+$, $E1 \leftarrow A0^+$ and $E1 \leftarrow A0^-$ transitions.

6) The $E1$ state was not found to decay to any state other than $X0^+$, and the $F1$ state was found to give rise to a bound-bound resonance fluorescence spectrum in its decay to the $A0^+$ state.

7) The Hg 4916 Å emission detected when probe-laser radiation in the 4200 - 4500 Å region was used, was found to arise from predissociation of HgZn molecules in the $F1$ state by a $D0^-$ curve-crossing followed by collisional mixing and pooling collisions of the resulting Hg 6^3P_0 atoms.

8) The fluorescence spectrum in the 4000 - 4450 Å region was shown to consist of resonance fluorescence bands arising from $E0^- \rightarrow A1$ and $E0^- \rightarrow A0^-$ decays. The $E0^-$ state was excited by transitions from both the $A1$ and $A0^-$ states.

9) The $E0^-$ state was found to decay to the $B0^-$ state, giving rise to bound-bound fluorescence spectrum observed in the 4600 - 4780 Å region. The $B0^-$ state was apparently not populated by the pump pulses since no $E0^- \leftarrow B0^-$ excitation spectrum could be produced.

10) The analysis yielded vibrational constants of the $A1$, $A0^-$, $A0^+$, $B0^-$, $C0^+$, $E1$, $F1$ and $E0^-$ states as well as the

relative energies and internuclear separations for some of the states; the results are summarized in Table (5.1).

The results derived from my investigations suggest that the various excited states participate in the absorption of radiation at various wavelengths in the 4000 - 4500 Å, 4600 - 4800 Å and 5200 - 6650 Å regions. Optical probing between these regions appeared to produce no significant absorption. I suggest, as an extension to this work, careful investigation of the 5000 - 7000 Å region to detect any laser-induced fluorescence which might help identifying new states. It would also be useful to identify the origin of the fluorescence spectrum observed at 2750 Å²¹, which has not yet been analyzed. This may require higher probe-laser power to compensate for the weak fluorescence signal. Finally, the success of the pump-and-probe method in the HgZn investigation may be taken as encouragement to use it for the study of other heteronuclear (and homonuclear) excimers such as HgCd, Cd₂, Zn₂, etc.

**TABLE 5.1 Molecular constants obtained from the fluorescence
and excitation spectra**

HgZn State	ΔE (cm^{-1}) ^a	ω_e (cm^{-1})	$\omega_e x_e$ (cm^{-1})	Δr_e (\AA) ^b
A1	0	195±3	0.88±0.2	0
A0 ⁻	653±12 600 ^c	194±3	0.7±0.2	0.01±0.01
A0 ⁺	906±12 600 ^c	192±4	0.8±0.2	0.01±0.01
B0 ⁻	2694±12 2900 ^c	181.5±2	1.0±0.2	0.03±0.01
C0 ⁺	17531±20 15000 ^c	117±4	0.5±0.2	0.26±0.01
E1	23519±12 19800 ^c	135±10		0.14±0.01
F1	24220±12 21500 ^c	167±4		0.14±0.01
E0 ⁻	24253±12 23000 ^c	158±4		0.12±0.01

a. ΔE is the energy of the $v = 0$ level relative to the $v = 0$ level of the A1 state

b. Δr_e is determined relative to r_e (A1)

c. Estimated from the PE diagram.

6 APPENDIX

The intensity distributions in various fluorescence bands were computer-simulated by computing the integral in eq. (2.33) numerically, in which $\psi'(r)$ and $\psi''(r)$ were assumed to be simple harmonic wavefunctions, generated by Hermitian polynomials. The vibrational constants of the upper and lower states ω_e' , $\omega_e x_e'$, ω_e'' and $\omega_e x_e''$, obtained from the analysis of the bands, were used in the modelling process and Δr_e , the difference in the internuclear separations, was set as a variable. The model did not include the Boltzmann distribution factors because the computer-simulation was restricted to fluorescence bands or excitation bands associated with a single v'' level (usually $v'' = 0$).

Figures A.1-4 show the results of the modelling, carried out with the appropriate Δr_e values (which are given in the figure captions), for (a) $v' = 0 \rightarrow v''$ and (b) $v' = 1 \rightarrow v''$ transitions in the $F1 \rightarrow A0^+$, $E0^- \rightarrow A1$, $E0^- \rightarrow A0^-$ and $E0^- \rightarrow B0^-$ fluorescence spectra, respectively. It may be seen that the computer-simulated intensity distributions in the spectra shown in Figs. A.1-4 (a) resemble those of the actual spectra shown in Figs. 4.15, 4.22, 4.22 and 4.24 ,

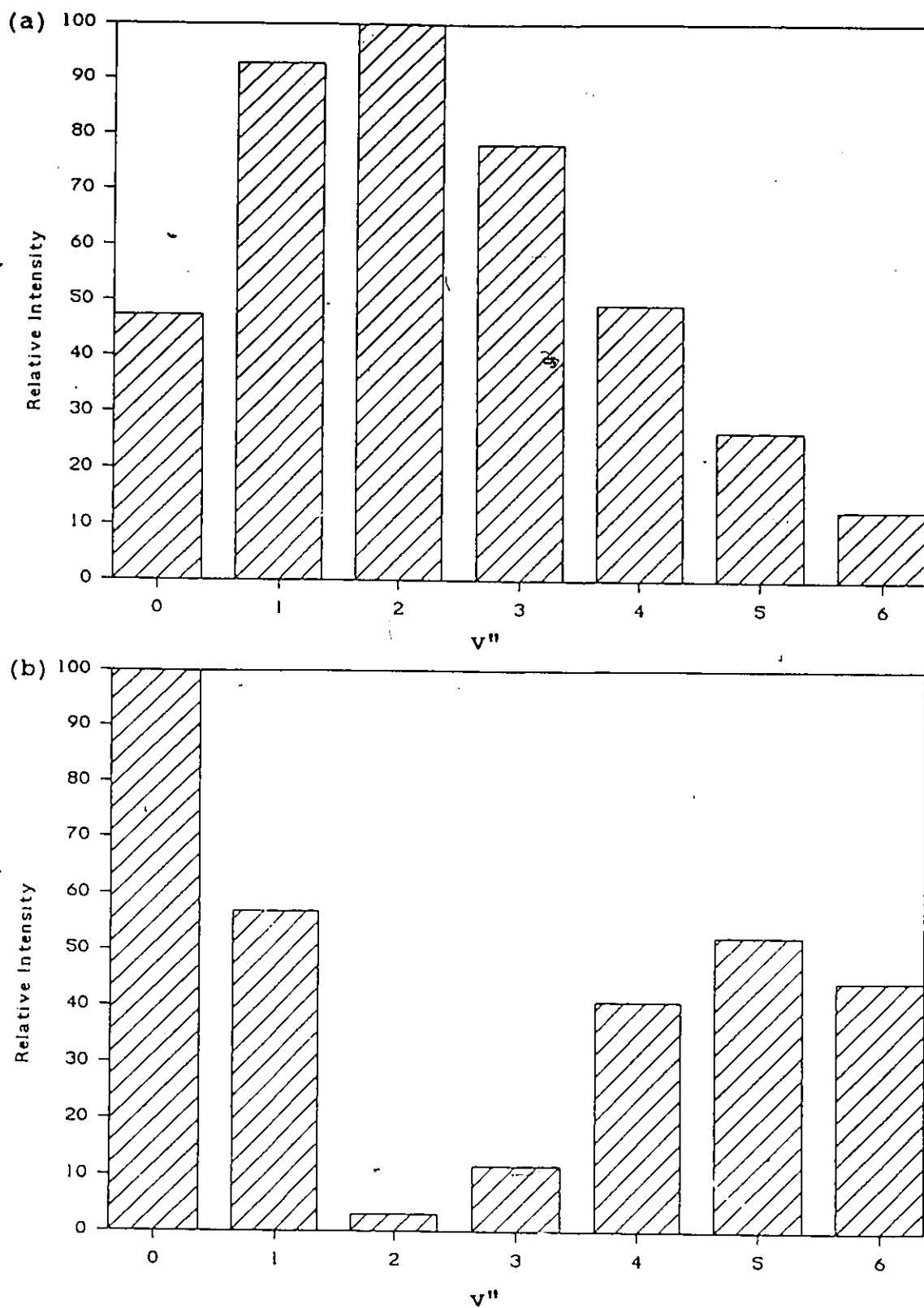


Figure A.1 Computer-simulated intensity distribution in the $F1 \rightarrow A0^+$ fluorescence spectrum ($\Delta r_e = .13 \text{ \AA}$).
(a) $v' = 0 \rightarrow v''$ and (b) $v' = 1 \rightarrow v''$.

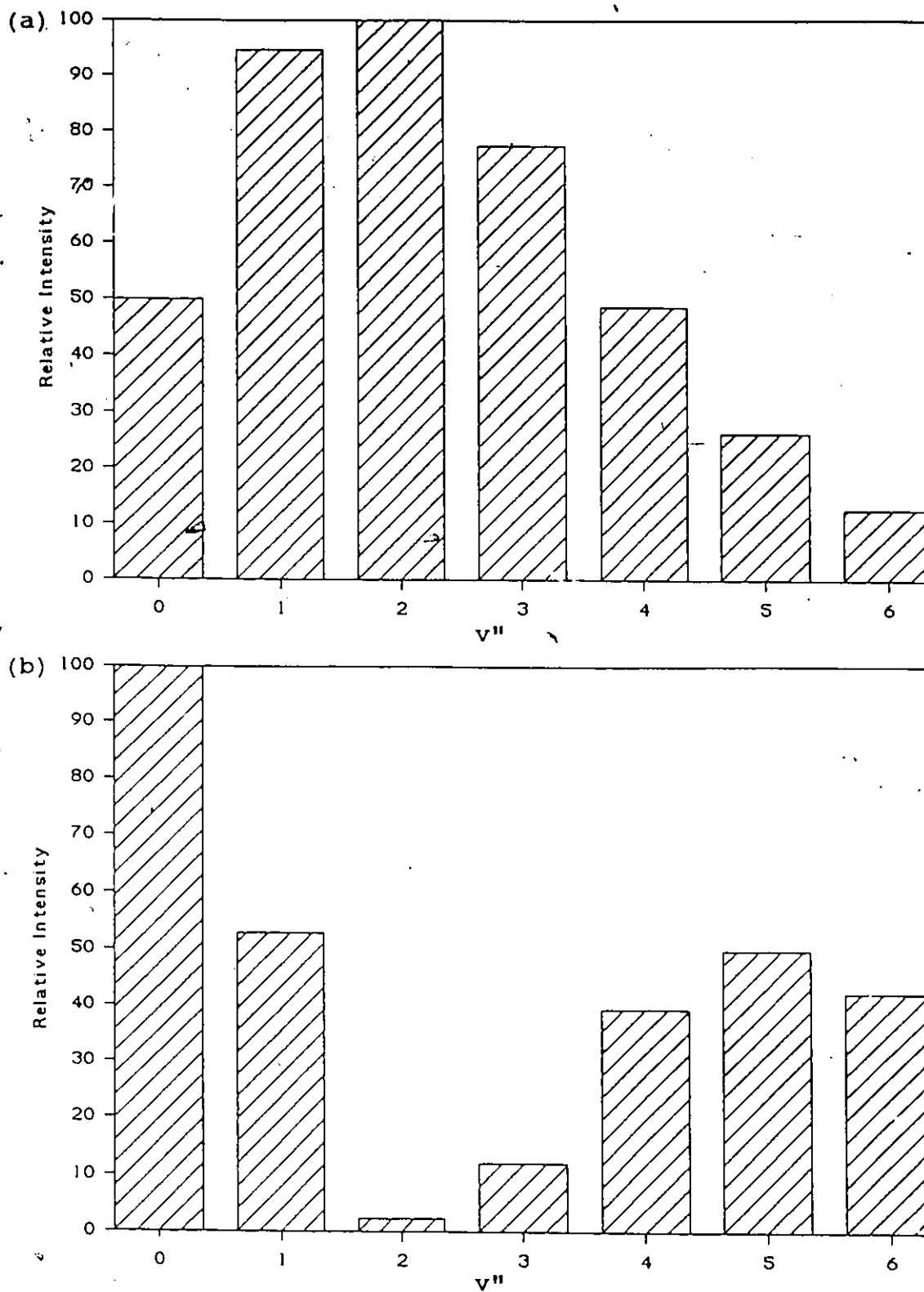


Figure A.2 Computer-simulated intensity distribution in the $E0^- \rightarrow A1$ fluorescence spectrum ($\Delta r_e = .13 \text{ \AA}$).
(a) $v' = 0 \rightarrow v''$ and (b) $v' = 1 \rightarrow v''$.

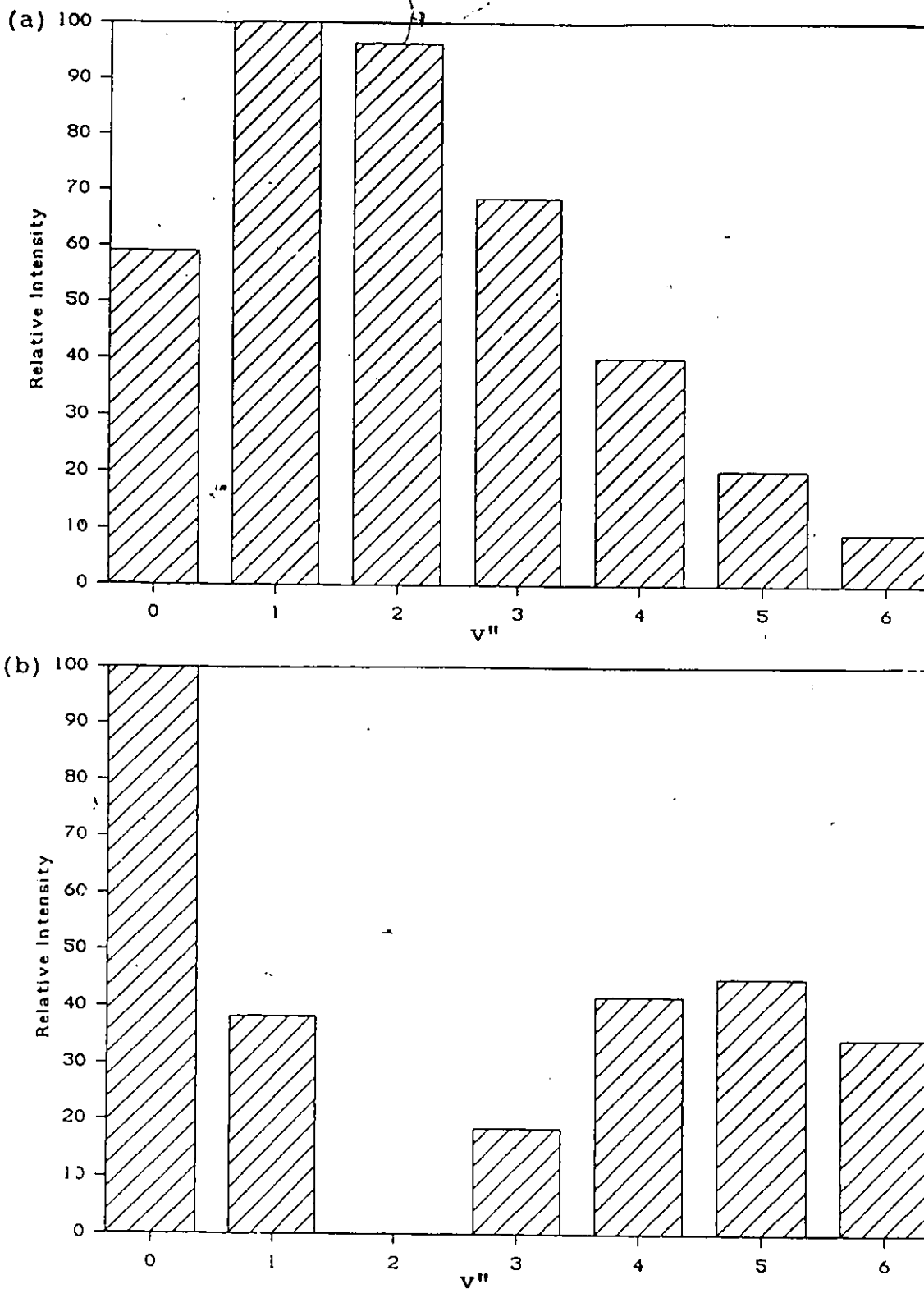


Figure A.3 Computer-simulated intensity distribution in the $E0^- \rightarrow A0^-$ fluorescence spectrum ($\Delta r_e = .12 \text{ \AA}$).
(a) $v' = 0 \rightarrow v''$ and (b) $v' = 1 \rightarrow v''$.

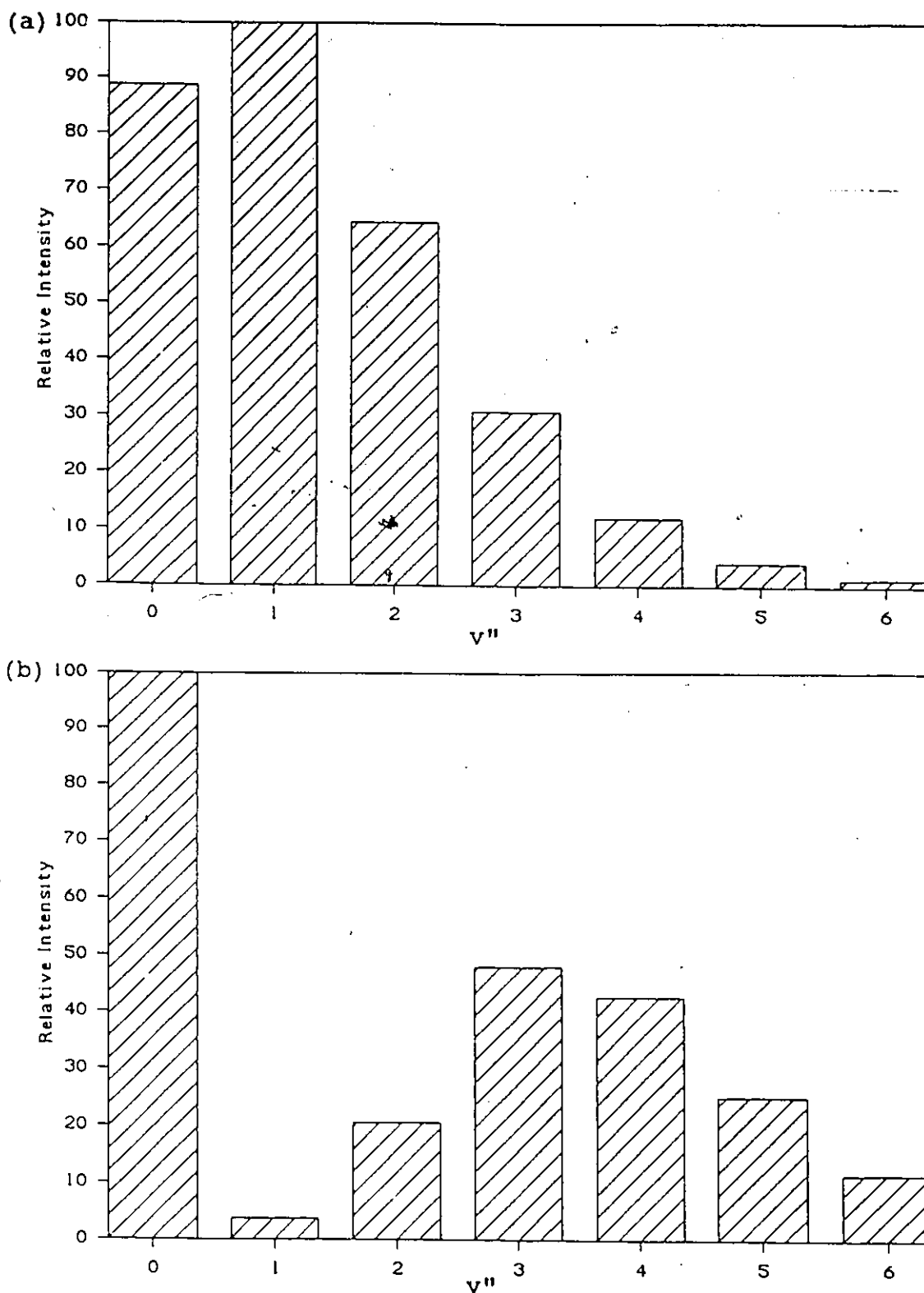


Figure A.4 Computer-simulated intensity distribution in the $E0^- \rightarrow B0^-$ fluorescence spectrum ($\Delta r_e = .1 \text{ \AA}$).
(a) $v' = 0 \rightarrow v''$ and (b) $v' = 1 \rightarrow v''$.

respectively, and that the computer-simulated intensity distributions in the spectra shown in Figs. A.1-4 (b) resemble those of the actual spectra shown in Figs. 4.16, 4.23, 4.23 and 4.25, respectively.

Figure A.5 shows the results of modelling of the $v' = 0 \leftarrow v''$ transitions in the $E1 \leftarrow A0^+$ excitation spectrum, which has a similar intensity distribution as in the actual excitation spectrum in Fig. 4.13. The modelled spectrum for the $v' \leftarrow v'' = 0$ transitions in the $C0^+ \leftarrow A0^+$ excitation spectrum, with the appropriate Δr_e , is shown in Fig. A.6. which has a similar intensity distribution as in the actual excitation spectrum in Fig 4.7. It should be noted that, for purposes of comparison, the excitation spectra in Figs. 4.13 and 4.7 should be normalized to the power curve of the dyes.

Figures A.7 and A.8, show how sensitive the modelled vibrational intensity distribution is to small changes in the Δr_e value. Fig. A.7 shows the intensity distribution for the $v' = 0 \rightarrow v''$ transitions of the $E0^- \rightarrow B0^-$ fluorescence spectrum resulting from putting (a) $\Delta r_e = .08 \text{ \AA}$, (b) $\Delta r_e = .12 \text{ \AA}$ and (c) $\Delta r_e = .2 \text{ \AA}$ instead of the optimum $\Delta r_e = .10 \text{ \AA}$. Fig A.8 shows a similar comparison for $v' = 1 \rightarrow v''$ transitions. This sensitivity, in fact, allowed the accurate determination of Δr_e values with a precision of ± 0.01

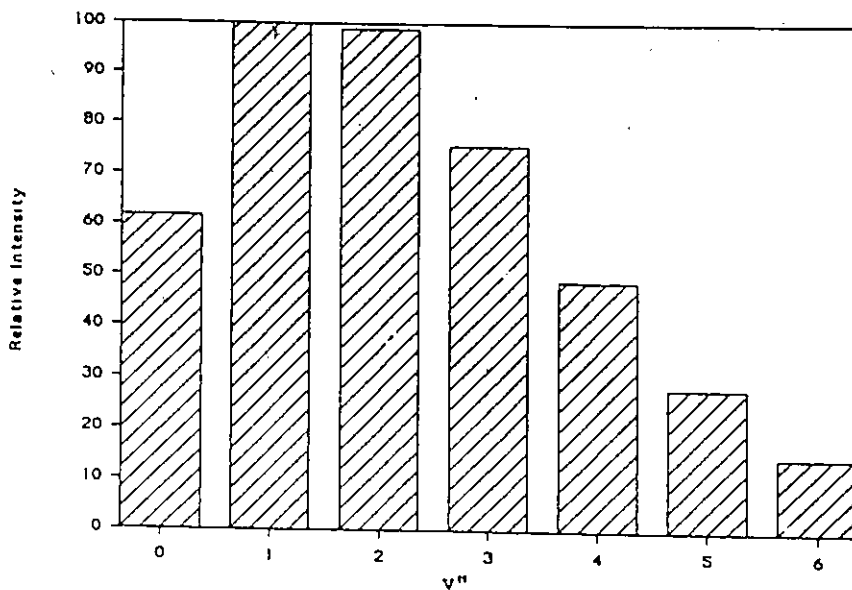


Figure A.5 Computer-simulated intensity distribution in the $E1, v' \leftarrow A0^+, v'' = 0$ excitation spectrum ($\Delta r_e = .13 \text{ \AA}$).

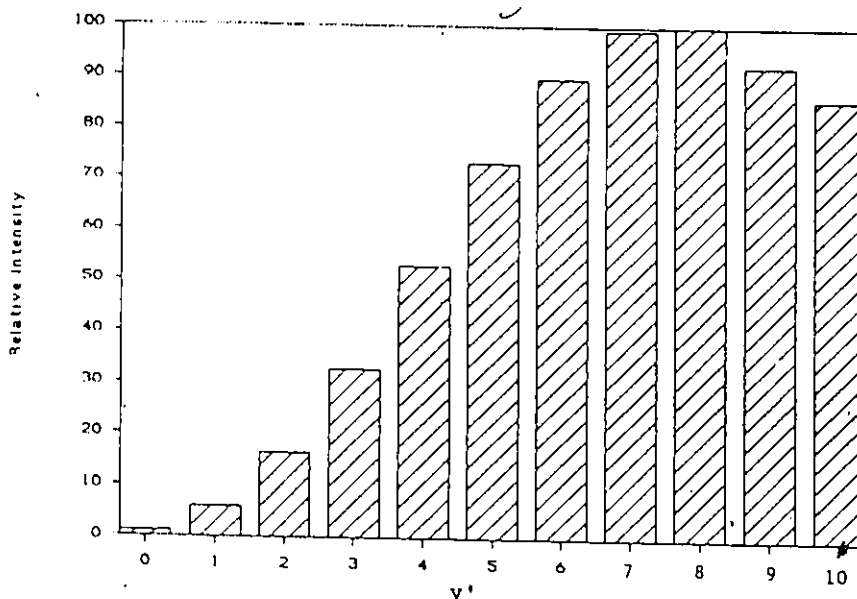


Figure A.6 Computer-simulated intensity distribution in the $C0^+, v' \leftarrow A0^+, v'' = 0$ excitation spectrum ($\Delta r_e = .25 \text{ \AA}$).

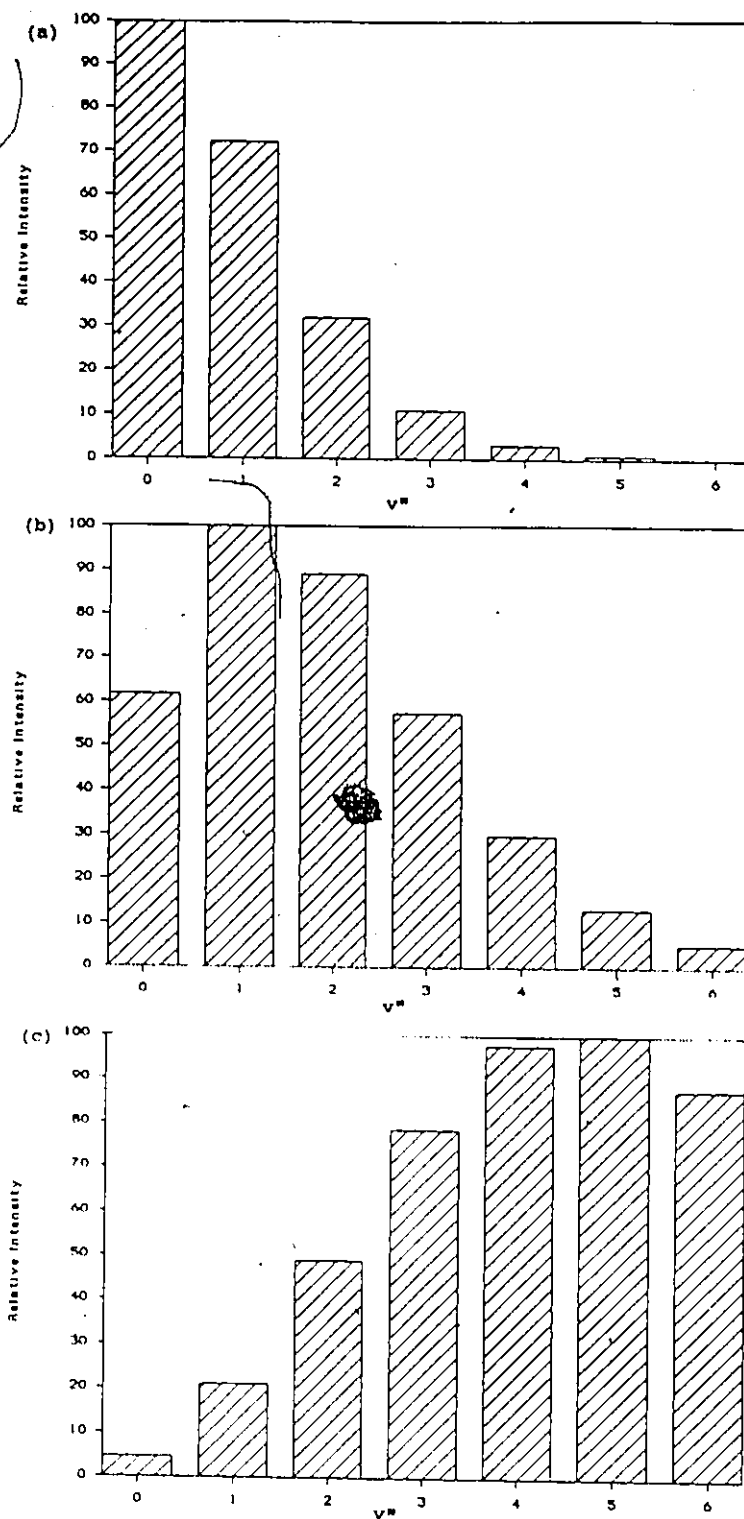


Figure A.7 Computer-simulated intensity distribution in the $E0^-$, $v' = 0 \rightarrow B0^-$, v'' fluorescence spectrum with Δr_e (a) = 0.08 Å, (b) = 0.12 Å and (c) = 0.2 Å.

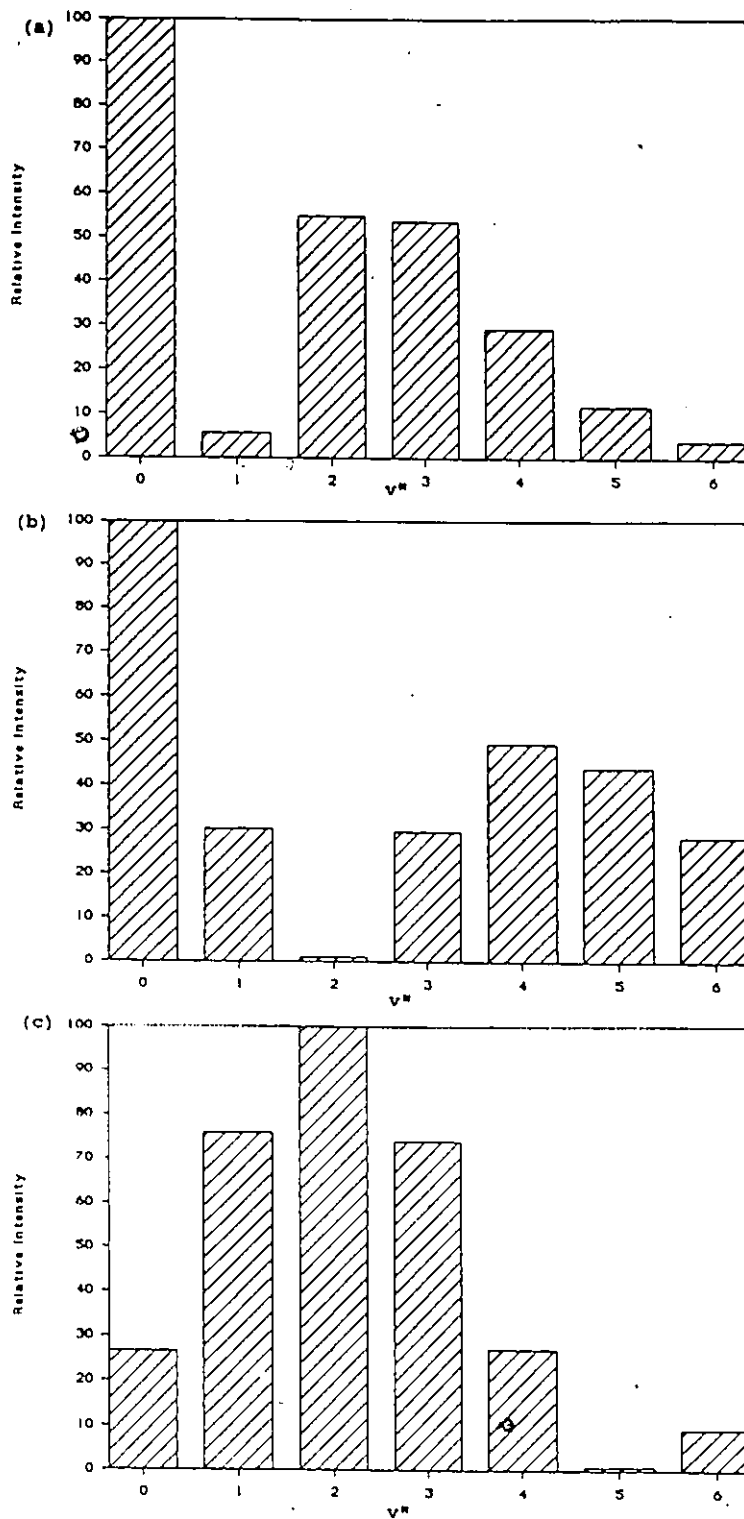


Figure A.8 Computer-simulated intensity distribution in the $E0^-, v' = 1 \rightarrow B0^-, v''$ fluorescence spectrum with Δr_e (a) = 0.08 Å, (b) = 0.12 Å and (c) = 0.2 Å.

A. Whenever possible, the Δr_e values were determined by modelling transitions originating from both the $v' = 0$ and the $v' = 1$ levels.

REFERENCES

1. J. G. Eden, *Optics Commun.* 25, 201 (1978).
2. R. J. Niefer, J. Supronowicz, J. B. Atkinson, and L. Krause, *Phys. Rev. A* 35, 4629 (1987), and references within.
3. A. B. Callear, *Chem. Rev.* 87, 335 (1987).
4. R. J. Niefer, J. Supronowicz, J. B. Atkinson, and L. Krause, *Phys. Rev. A* 34, 2483 (1986).
5. K. C. Celestino and W. C. Ermler, *J. Chem. Phys.* 81, 1872 (1984).
6. C. H. Su, Y. Huang, and R. F. Brebrick, *J. Phys. B* 18, 3187 (1985).
7. H. Tatewaki, M. Tomonari, and T. Nakamura, *J. Chem. Phys.* 82, 5608 (1985).
8. R. M. Hill, D. J. Eckstrom, D. C. Lorents, and H. H. Nakano, *Appl. Phys. Lett.* 23, 373 (1973).
9. R. J. Carbone and M. M. Litvak, *J. Appl. Phys.* 39, 2413 (1976).
10. L. A. Schlie, B. D. Guenther, and R. D. Rathge, *Appl. Phys. Lett.* 28, 393 (1976).
11. H. Komine and R. L. Byer, *J. Chem. Phys.* 67, 2536 (1977).
12. M. W. McGeoch *J. Chem. Phys.* 71, 140 (1980).
13. M. W. McGeoch *J. Chem. Phys.* 73, 2534 (1980).
14. D. Drummond and L. A. Schlie *J. Chem. Phys.* 65, 3454 (1976).
15. G. Chambaud and W.E. Baylis, 1989. Private communication.
16. E. Hegazi, J. Supronowicz, G. Chambaud, J. B. Atkinson, W.E. Baylis and L. Krause, (to be published).
17. R. J. Niefer, J. Supronowicz, J. B. Atkinson, and L. Krause, *Phys. Rev. A* 34, 1137 (1986).

18. J. Supronowicz, R. J. Niefer, J. B. Atkinson, and L. Krause, *J. Phys. B* 19 (1986) 1153-1164.
19. J. Supronowicz, R. J. Niefer, J. B. Atkinson, and L. Krause, *J. Phys. B: At. Mol. Phys.* 19 (1986) L717-L721.
20. J. Supronowicz, E. Hegazi, G. Chambaud, J.B. Atkinson, W.E. Baylis, and L. Krause, *Phys. Rev. A* 37, 295 (1988).
21. C. E. Moore, *Natl. Bur. Stand. U.S.A. Circ. No. 467*, Vol. III (1958).
22. W. E. Baylis, *J. Phys. B* 10, L583 (1977)
23. F. H. Mies, W. J. Stevens, and M. Krauss, *J. Mol. Spectrosc.* 72, 303 (1978).
24. P. J. Hay, T. H. Dunning, and R. C. Raffanetti, *J. Chem. Phys.* 65, 2679 (1976).
25. C. F. Bender, T. N. Rescigno, H. F. Schaefer III, and A. E. Orel, *Chem. Phys.* 71, 1122 (1979).
26. G. Herzberg, 1950. Spectra of Diatomic Molecules (New York, Van Nostrand Publ. Co.).
27. R.S. Mulliken, *J. Chem. Phys.* 55, 309 (1971).
28. E.U. Condon, *Phys. Rev.* 32, 858 (1928).
29. R.J. Niefer and J.B. Atkinson, *Optics commun.* 67, 139 (1988).
30. W. Kedzierski, R. Berends, J. B. Atkinson, and L. Krause, *J. Phys. E.* 21, 796 (1988)
31. R.J. Niefer and J.B. Atkinson, 1985. Private Communication.
32. A.N. Nesmeyanov, 1963. Vapour Pressure of the Elements (Academic Press, New York).
33. J. Nestor, *Appl. Opt.* 21, 4154 (1982).
34. J. Supronowicz, E. Hegazi, J.B. Atkinson, and L. Krause (to be published).
35. G.R. Fournier, 1988. Private Communication.
36. J. Supronowicz, E. Hegazi, J.B. Atkinson and L. Krause, *Phys. Rev. A* 37, 3818 (1988).

37. E. Hegazi, J. Supronowicz, J.B. Atkinson, and L. Krause (to be published).
38. O. P. Bochkova, E. Gamarts, and Yu. A. Tolmachev, Opt. Spectrosc. 36, 150 (1974).
39. E. Hegazi, J. Supronowicz, J.B. Atkinson, and L. Krause (to be published).

VITA AUCTORIS

I was born on March 28, 1959 in Cairo, Egypt. In 1962, my family moved to Kuwait where I completed my primary, intermediate and secondary education. Having moved back to Egypt I entered Ain Shams University in Cairo in 1975, and obtained my honours B.Sc. degree in Physics in 1979. During the years 1979-81 I was on the staff of the Faculty of Science at that University. In 1982 I enrolled in the Physics M.Sc. program at the Catholic University of America in Washington, D.C., USA, and graduated in 1985. I arrived in Canada in January 1986 and enrolled in the Ph.D. program in Physics at the University of Windsor, Ontario. During my graduate studies, the University of Windsor granted me various graduate scholarships.